UNIMORE
UNIVERSITÀ DEGLI STUDI DI
MODENA E REGGIO EMILIA

UNIVERSITÀ DEGLI STUDI
DI MODENA E REGGIO EMILIA

Dottorato di ricerca in
"Ingegneria industriale e del territorio"

Ciclo XXXVIII

Vibration Analysis of Electric Powertrain: Effect of Electro-mechanical Interactions

---

Candidate: Razie Ebrahimnejad

Relatore: Prof. Giovanni Franceschini

Eventuale Correlatore: Prof. Alberto Muscio

Coordinatore del Corso di Dottorato: Alberto Muscio

Dedicated to:

My homeland, **IRAN.**

To **Mohammadreza Ghasemzadeh** and his father,

To the brave Iranians, sacrificed their life for freedom in **8-9 January 2026**.

Acknowledgment

I express my heartfelt thanks to Giovanni Iarriccio, whose guidance, encouragement, and unwavering support illuminated the path through the challenges and uncertainties of this research. His advice has been both a compass and a source of inspiration throughout this journey.

I sincerely thank Professor Francesco Leali for his insightful support and encouragement, which has made this work possible. My profound appreciation goes to Professor Giovanni Franceschini, whose mentorship, wisdom, and expertise were instrumental in shaping both the content and quality of this thesis. I am deeply grateful to Professor Marco Barbieri, whose support, mentorship, and example of resistance have not only strengthened this research but also inspired my growth as a scholar.

I also extend my appreciation to professor Silvio Sorrentino, Professor Stefano Nuzzo and Dr. Alessandro De Felice, for their invaluable guidance during my Ph.D. journey.

Finally, a special thanks goes to my colleague, Alessandro Capitanio; achieving these outcomes would not have been possible without his dedicated collaboration.

Table of Contents

List of Figures

List of Tables

Abstract

The global transition toward the electrification of vehicle drivetrains has introduced novel engineering challenges, particularly concerning Noise, Vibration, and Harshness (NVH) performance. The inherent quiet operation of the electric drive system eliminates the acoustic masking provided by conventional Internal Combustion Engines (ICE), thereby intensifying NVH issues such as gear whine, motor whistle, and inverter noise due to pulse-width modulation (PWM). These acoustic attributes are critical determinants of perceived product quality and passenger comfort. To enhance the dynamic performance and long-term reliability of the system, an electromechanical dynamic analysis of the coupled motor-gear transmission system is crucial. This is necessary to accurately capture electromechanical interaction effects that cannot be fully characterized by purely mechanical models. This study addresses this requirement by presenting a comprehensive modeling methodology for the dynamic analysis of torsional vibrations within electric powertrains, including gear transmissions. Given the inherently nonlinear nature of the coupled system, a hybrid modeling strategy is employed, leveraging analytical formulations in conjunction with Finite Element (FE) simulation data. The mechanical transmission is a single-stage spur gear pair; gear mesh stiffness is defined by a periodically time-varying function, and the model incorporates the nonlinear effects of gear backlash. Torsional flexibility of the drive shafts is retained using equivalent stiffness coefficients, while the compliance of bearings and supports is excluded from the current model. The mechanical subsystem is dynamically coupled with an Interior Permanent Magnet Synchronous Motor (IPM). The IPM is represented by a non-linear model, accounting for magnetic anisotropy and magnetic saturation, parametrized using data derived from dedicated Finite Element Analysis. This high-fidelity approach facilitates the capture of critical nonlinear effects stemming from magnetic saturation and flux spatial harmonics, which are essential for accurate response prediction. Machine control is simulated via nested, speed (outer) and current (inner) control loops. To analyze the dynamic stability, a set of linearized equations is derived to determine the system's linear normal modes. Furthermore, the frozen time method is applied to derive the system normal modes under the presence of electromechanical interactions. Dynamic simulations are subsequently performed via direct numerical integration of the governing equations. The analysis focuses on exploring amplitude–frequency curves, bifurcation diagrams, and steady-state responses across various operating regimes to evaluate potentially critical oscillations. This comprehensive model enables a rigorous investigation of electromechanical coupling phenomena often neglected in simplified analyses (i.e., purely mechanical models or those relying on motor models based on concentrated parameters). The main contribution of this research lies in demonstrating the accurate

assessment of the electric powertrain's dynamic behavior under time-varying motor torque, highlighting how the torque is influenced not only by the target load but also by the overall dynamic conditions of the system—a critical coupling effect hitherto unreported in the context of gear whine noise analyses within electric drive NVH studies.

Keywords: Electric powertrain, Electro-mechanical interactions, Gear nonlinear dynamics, Torque Ripples, Frequency analysis.

Chapter 1: Literature Review

1.1. Introduction

Electromechanical powertrain systems, typically comprising an electric motor coupled with a reduction or transmission gear set, constitute a foundational technology across a wide spectrum of industrial, transport, and automated machinery. The widespread adoption of this architecture is attributable to its inherent operational merits, which include high reliability, an impressive power-to-weight ratio, and cost-effectiveness. Despite these clear advantages, the performance and longevity of these integrated systems are frequently constrained by various operational vulnerabilities, which manifest as both electrical abnormalities (e.g., stator winding faults, current harmonics) and mechanical failures (e.g., gear wear, bearing degradation). Furthermore, with the continuous advancement of modern electric drive systems toward larger power capacities and higher levels of system integration, a more complex challenge has emerged: the mechanical vibration resulting from the intricate electromechanical interaction effect. This coupling phenomenon involves the motor's harmonic electromagnetic torque exciting the structural dynamics of the gear set, leading to vibrations that can significantly increase acoustic emissions and accelerate component fatigue. Given the critical role these systems play in modern industries, it has become essential to conduct a rigorous electromechanical dynamic analysis of the motor-gear system. Such analysis is not merely a diagnostic tool, but a prerequisite for enhancing the system's dynamic control and performance, ensuring stability, and fundamentally enhancing long-term system reliability under demanding operational conditions.

1.2 Research Background

1.2.1 Electric motors modeling approaches

From an industrial perspective, the major types of electric motors adopted or under consideration for HEVs, as well as for EVs, include DC motor, induction motor (IM), permanent magnet (PM) synchronous motor, and switched reluctance motor (SRM). However, compared with other commonly employed motors for EVs, a permanent-magnet synchronous motor (PMSM) possesses better compromised performance, particularly the interior PMSM (IPMSM) [1-2]. The rigorous dynamic modeling and simulation of electric motors represents a basis of modern electrical machine design and control. A foundational moment in this field can be traced to 1987, when Laitwaite [3] introduced the Magnetic Equivalent Circuit (MEC) method and it was then developed by Ostovic at 80s [4-5]. This approach was developed later by combining it with the two-reaction theory of Blondel [6]. This theory was later generalized and extended to the method known as Park transformation by Park [7], i.e., the widely utilized direct-quadrature (d-q) models of electric machines.

The d-q model is particularly essential for analyzing and controlling Alternating Current (AC) machines, especially permanent magnet synchronous machines (PMSMs) and induction motors. This powerful model simplifies the complex, time-varying dynamics of the three-phase system by transforming it into an equivalent two-axis system (d-q) rotating synchronously with the rotor's magnetic field. This transformation effectively linearizes the machine equations, reducing the variables to be controlled and allowing for easier mathematical manipulation and the design of high-performance controllers, such as Field-Oriented Control. The d-q transformation is a crucial technique because it decouples the variables associated with the machine's operation, allowing for independent control of torque and flux. This decoupling is achieved by representing the machine's voltages and currents in a rotating reference frame that aligns with the rotor's magnetic field. The d-q model has limitations, particularly in accurately simulating harmonics and unbalanced operations, since it is based on the assumption that core saturation is ignored, the permanent magnetic field is assumed as a sinusoidal distribution, the power source is a sinusoidal wave, the air gap is uniform, and the effects of the change of electromagnetic parameters and harmonics are ignored as well. Some studies suggest that neglecting these factors can lead to inaccuracies in performance predictions [8]. Kallio et al. [9] pointed out that conventional d-q models often oversimplify the machine behavior by focusing solely on fundamental components, which can lead to inaccuracies in performance analysis. They proposed a FE-based phase-variable model for double-star PM synchronous machines, and they showed that the current harmonics mainly arise due to inductance harmonics.

The effect of magnetic saturation in the nonlinear modeling of synchronous machines has received attention since the early 80^{s} [10,11]. One of the key advantages of MEC is its ability to incorporate magnetic saturation effects. Saturation occurs when the magnetic material reaches its maximum magnetic flux density, leading to nonlinear behavior that can significantly affect machine performance. MEC models can be designed to account for these nonlinearities, providing more accurate predictions of machine behavior compared to linear models [12]. This is particularly useful during the design phase of electrical machines. It allows engineers to quickly evaluate multiple design configurations and optimize parameters such as winding turns, core materials, and geometrical dimensions. This analysis capability is crucial in modern design processes where multiple iterations are often required to achieve optimal performance [13]. Iglesias et al. [14] developed a model to include the variable magnetic saturation effects in a self-computed synchronous machine model. E. Levi in the 90^{s} developed the d-q axis model in induction machines by considering the effect of magnetic saturations [15-20]. Despite all the limitations of d/q axis methodology, subsequent research has built upon these fundamental modeling techniques, extending their application to coupled electromechanical systems through sophisticated methods like the finite element method (FEM) for detailed magnetic field analysis and comprehensive circuit-field models to accurately capture phenomena like saturation, spatial harmonics, and fault conditions.

Over decades, there have been many interests in theoretically simulating the dynamic forces by supposing simplification in the energy distribution in air gaps due to the interaction of the magnetic fields of rotor and stator. Early in 1987, Belmans and Vandenput [21] by assuming the infinite permeability of the rotor iron path and sinusoidally distributed MMF along the air gap, by applying Ampere's law, wrote the nonlinear air gap permeance in a Fourier series expansion. Frosini et. al. [22] improved the model by including the tangential flux density calculated from motor torque. To find a relationship between the torque and the tangential stress acting upon the rotor and stator surfaces of an electrical machine, they consider the two basic phenomena acting on almost all electric machines: the force exerted on an electric current in a magnetic field (Lorentz force) and the force produced between ferromagnetic structures carrying a magnetic flux (Maxwell force). Ampere’s circuital law is fundamental in understanding the magnetic fields generated by electric currents. This law is applied to analyze the magnetic circuit, which includes the air gap, stator core, and rotor core. By applying this law, the expressions for magnetic flux density and magnetic field strength can be derived, which are critical for accurately modeling motor performance. The integration of Ampere’s law into the magnetic circuit containing the air gap, stator core, and rotor core with energy considerations allows for a comprehensive analysis of the motor's electromagnetic behavior. Im et al. [23] derived the

governing equations of a brushless DC motor by combining the electrical and mechanical equations of the motor and applying Lagrange's equation. Huang et al. [24] discussed parameter identification methods for brushless DC motors, which often involve energy considerations to accurately estimate motor parameters such as stator inductance and rotor flux linkage. Sudhoff et al. [25], presented a comprehensive approach to model induction motors using MEC method. The study highlights the advantages of MEC in capturing the complex magnetic interactions within induction motors, particularly under varying operational conditions. In conclusion, this approach facilitates the calculation of magnetic flux distribution and helps in understanding the machine's behavior under different conditions; however, due to the inherent nonlinearity of the system applying FEM is necessary [26].

While FEM provides detailed spatial resolution and can handle complex geometries, MEC offers a more computationally efficient approach for preliminary analysis. Amrhein [27] compared the results from FEM, experiment, and the magnetic equivalent circuit method (MEC) and indicated that MEC, corrected for local saturation, is a promising option for a design tool. On the other hand, this hybrid modeling strategy allows for a comprehensive understanding of machine dynamics, particularly in scenarios where both local and global effects are significant [28]. Recent advancements have enabled the use of MEC in real-time simulations, particularly in hardware-in-the-loop (HIL) setups. This capability is essential for applications requiring immediate feedback and control, such as in electric vehicles and renewable energy systems. In addition, MEC models can be implemented on platforms like field-programmable gate arrays (FPGAs) to achieve the necessary computational speed and accuracy [29].

1.2.2 Gear transmission

Gears were first described by the Greek mathematician Archimedes (287–212 B.C) [30]. While the Chinese legends refer to the South Pointing Chariot originally designed by Emperor Huang Di, in the 27th century B.C.E, probably as the earliest known mechanism to include gears inside. The discovery of the Antikythera Mechanism, the oldest known astronomical machine, shows that the ancient Greeks used metal gears with cylindrical teeth in early computing equipment and astronomical calendars around 87 B.C.E [31]. Aristotle (4th century B.C.E) wrote about friction wheels, and Philo of Byzantium (3rd century B.C.E) described geared water mills, Hero of Alexandria (c. 10–70 CE) provided the most detailed early theoretical accounts of gear ratios and reduction [32]. His theoretical illustration of gear ratios in Arabic translation is kept in British Library. More than 1,500 years later, gears figured prominently in Leonardo da Vinci's sketches. In 1835, English inventor Joseph

Whitworth patented the first gear hobbing, a machining process to cut gears, splines, and sprockets. Robert Willis made important contributions to machine element design, particularly in the shape of gear teeth [33]. Rotary contact between bodies was solved theoretically by Leonhard Euler in the eighteenth century. Euler proved that either epicycloid-shaped or involute-shaped teeth could pass motion from one body to another without angular acceleration [34]. The first to formulate the tooth root stress of the gears was Lewis who in 1892 applied the cantilever beam approach to model the gear pairs [35]. The experimental measurement of dynamic loads was initiated in 1925 by a special research committee of the ASME, and the findings were published in 1931. Earle Buckingham [36] considered the dynamic load to comprise the transmitted tangential load plus an incremental dynamic component, and he developed a series of equations to calculate this dynamic load. In 1937, Almen and Straub [37] introduced a method for evaluating bending strength of gear teeth. Their formulation remained a fundamental basis for calculating root fillet stress in accordance with established standards such as ISO 6336-1 (1996) [38], ISO 6336-2 (1996) [39], ISO 6336-3 (1996) [40], and ISO 6336-5 (1996) [41]. Harris devoted many years in this field to develop analytical models and experimental analysis of the dynamic loads of spur gears, and the fundamental definition of transmission error first was introduced by him [42]. Extensive research was devoted to dynamic load of gear pairs since 1950 to increase the performance of machineries, including the first spring-mass model, which was introduced by Tuplin [43-47]. The analytical framework for calculating contact pressure originated from Hertz's theory and was subsequently modified to suit gear tooth contact conditions by Johnson [48]. For a long time, these simplified equations were the only practical means of estimating gear failure. The outstanding works of Litvin [49,50] covered the lack of understanding of the geometry of all kinds of gears. Litvin revised, expanded and unified in a unique compact analytical theory, called the theory of meshing, all the useful equations to design and generate gears starting from all types of manufacturing process. His work covered: spur involute gears, internal involute gears, noncircular gears, cycloidal gearing, involute helical gears with parallel axes, modified involute gears, involute helical gears with crossed axes, face-gear drives, worm-gear drives with cylindrical worms, double-enveloping worm-gear drives, spiral bevel gears, hypoid gear drives, planetary gear trains, generation of helicoids, design of fly blades and generation of surfaces by CNC machines.

Over years, extensive research has been dedicated to understanding and predicting gears' dynamic behavior. While the foundational work in this field began with simple spring-mass models to determine the dynamic load factor, it quickly evolved into sophisticated, multi-degree-of-freedom systems capable of representing the complex, coupled torsional, lateral, and axial motions of gear trains [51,52]. This rigorous dynamic modeling of gear systems is essential, because the primary

internal excitation is the time-varying mesh stiffness, which is compounded by geometric imperfections and non-linear factors like backlash [53,54]. Over the decades, a vast body of literature has been developed, establishing both classical lumped-parameter and more advanced finite element (FE) approaches to simulate these intricate interactions [55,56]. The primary aims of these modeling efforts are diverse, focusing directly on engineering performance and reliability, as highlighted in numerous comprehensive reviews [51,53]. A major objective is the control of noise and vibration, where the metric of Transmission Error (TE) is established as the fundamental excitation source that must be minimized through design [54,55,60]. Concurrently, researchers have sought to enhance the long-term integrity of transmissions through detailed system stability analysis. The inclusion of significant non-linearities, such as gear backlash and bearing clearance, has revealed complex behaviors like bifurcation and chaos, which directly threaten the operational stability and system life [52,58]. Therefore, modern dynamic modeling continues to be a crucial tool for both predicting performance under ideal conditions and analyzing the robustness of the system against failure-inducing phenomena [57].

1.2.3 Coupled electromechanical studies

In recent years, electric drive systems (EDS) for electric vehicles (EVs) have undergone significant development, driven by the need to achieve high speed, high integration, and high-power density, which inherently increases the performance requirements and complexity of the entire system. A key design change involves the elimination of components like clutches and the adoption of the structure, where the drive motor is directly coupled with the gear system. While simplifying the structure, this direct coupling allows for greater transmission of disturbances, often leading to a deterioration of the system's vibration state. This intimate interaction increases the complexity of the overall dynamic characteristics of the system. Therefore, revealing the electromechanical coupling vibration mechanism of the electric drive system under various operating conditions and studying the influence of multi-source composite excitations including electromagnetic vibration from the motor, inherent mechanical vibration from the gears, and external load excitations on the system's dynamic characteristics are essential research imperatives for improving the electric drive system's crucial Noise, Vibration, and Harshness (NVH) performance.

The development of dynamically coupled electromechanical models has attracted increasing attention in recent years, particularly as electric automotive industry continues to evolve toward higher efficiency and performance. Several studies have focused on capturing the mutual interactions

between electromagnetic excitations and mechanical vibrations, revealing that electromechanical coupling may significantly alter the dynamic behavior of power transmission systems.

The development of dynamically coupled electromechanical models has been addressed in several recent studies [61–64], highlighting the growing importance of capturing electrical–mechanical interactions in modern electric drive systems. As the industry moves toward higher levels of electrification, understanding how electromagnetic excitations propagate through transmission components has become critical for predicting vibration, noise, and durability. Jiang et al. [65] focused on the electromagnetic influence on the normal modes of a multistage transmission driven by a Permanent Magnet Synchronous Motor (PMSM). In their formulation, the electromagnetic characteristics of the motor were not modeled explicitly but were instead represented by an equivalent set of torsional stiffness and damping coefficients. These coefficients were incorporated into a lumped-mass bending–torsional model of the gearbox, and the coupling between the electrical and mechanical subsystems was analyzed using the frequency response function (FRF) method. The results demonstrated that electromagnetic effects have a measurable impact on the modal behavior of the gearbox, particularly under operating conditions where the interaction between motor torque and gear flexibility is strong. Fan et al. [66] advanced the modeling strategies by proposing a multi-excitation mechatronic model of an electric powertrain. Their work showed that when electrical and mechanical subsystems are modeled together, electromechanical coupling introduces additional vibration modes that are absent in purely mechanical models. This finding emphasizes that vibration prediction for electric powertrains cannot rely solely on structural mechanics, since electromagnetic excitation can significantly alter the global dynamic response. Feki et al. [67] developed an integrated nonlinear electromechanical dynamic model to investigate how tooth faults affect the stator current signals of the motor. They formulated a nonlinear first-order differential system in which the state vector includes both mechanical and electrical variables, providing a unified representation of the coupled dynamics. This approach enabled a direct link between mechanical fault characteristics and their electrical signatures, demonstrating the potential of electromechanical models for fault diagnosis and condition monitoring. Bai et al. [68,69] extended these efforts by coupling a nonlinear permeance network model of the electric motor with a lateral–torsional dynamic model of a planetary gear system. Their study compared the dynamic loads acting on the gears with and without considering spatial and nonlinear effects in the motor model, showing that these nonlinearities substantially influence the transmitted forces. As electromagnetic torque fluctuations are a dominant source of vibration and noise in electric powertrains, Chen et al. [70] proposed a combined theoretical and finite element analysis (FEA) framework based on the fixed-permeability method [71]. Their model

accounted for magnetic saturation and multiple harmonic components of the magnetic field to accurately predict electromagnetic torque in a PMSM. The results showed excellent agreement with FEA simulations and confirmed the ability of the method to capture torque ripple harmonics.

A more detailed investigation of electromechanical coupling phenomena in electric vehicle (EV) powertrains was performed by Ge et al. [72]. They analyzed the dynamics of a two-stage helical gear transmission driven by a PMSM, where the time-varying gear mesh stiffness was modeled analytically using the slice method. The PMSM torque was determined through finite element analysis (FEA) combined with the frozen-permeability method, enabling a state-dependent torque formulation capable of capturing electromagnetic nonlinearities. Their results highlighted that even modest torque fluctuations can significantly modify the torsional vibration response of the transmission, particularly in the presence of multiple sources of excitation. The nonlinear dynamics of a two-stage automotive transmission were studied by Donmez and Kahraman [73]. In their lumped-parameter model, the electromagnetic torque was represented as a fluctuating input, and the formulation was validated using a deformable-body benchmark. The steady-state analysis revealed operating regions where electromechanical coupling strongly influenced the system dynamics, while transient simulations under regenerative braking exhibited dominant low-frequency vibrations of the output drivetrain. These results suggested that inclusion of regenerative effects is essential when predicting transient response, although the absence of closed-loop control in the model led to amplified torque oscillations. Most recently, Mughal et al. [74] developed a tribodynamic model to investigate gear whine noise in electric drive units. Although their analytical model excluded the electric motor dynamics, experimental measurements showed that the interaction between electrical harmonics and gear mesh resonances plays a significant role in the observed vibration and noise behavior. Their findings indicate that, to accurately capture these phenomena, future models must incorporate the electromechanical coupling introduced by electric motor operation, as simplified models may underestimate or misrepresent the superimposed harmonic content.

1.3 Research gap

Recent developments in electric drive systems have established that electromechanical coupling plays a decisive role in shaping the vibration behavior of modern electric powertrains. Existing studies have made meaningful contributions by incorporating electromagnetic effects into drivetrain vibration models, demonstrating that electromagnetic excitations can modify modal characteristics, introduce additional vibration modes, and influence fault signatures. However, the current state of the literature reveals several limitations that prevent a complete understanding of the dynamic behavior of electric powertrains under realistic operating conditions.

First, many available electromechanical models use simplified representations of the motor dynamics. In several studies, the electromagnetic contribution is treated through equivalent stiffness and damping coefficients or by prescribing fluctuating torque inputs without detailed consideration of nonlinear magnetic effects. Although these approaches provide qualitative insights, they neglect spatial flux harmonics, magnetic saturation, and control-induced interactions, which are inherent to interior permanent magnet (IPM) machines used in high-performance automotive applications. As a result, the models may underestimate the magnitude and frequency content of torque ripple that strongly contributes to torsional vibrations.

Second, while some recent investigations have combined finite element (FE) electromagnetic analysis with analytic transmission models, the drivetrain is often simplified to linear or weakly nonlinear forms. Gear mesh coupling, backlash, and time-varying stiffness—critical features of spur or helical gear interactions—are either idealized or considered separately from the electromechanical effects. Consequently, the mutual influence between nonlinear gear dynamics and electromagnetic excitations has not yet been fully captured, especially under time-dependent operating conditions.

Third, closed-loop motor control effects are mostly absent or only partially included in existing models. Studies focusing solely on torque excitations do not reflect the fact that the electric machine operates under nested speed–current control loops that actively modify torque delivery. Without modeling the control architecture, simulated responses may exaggerate or overlook oscillatory behavior observed in real applications, particularly during rapid load changes, regenerative braking, or high-speed torque tracking.

Fourth, investigations to date tend to focus on either steady-state or modal characteristics, whereas few studies address the full dynamic spectrum of the electromechanical system. Critical transient phenomena, bifurcations, and multi-source excitation interactions involving electromagnetic torque ripple, gear mesh vibration, and external load disturbances have not been examined within a unified

nonlinear framework. These interactions are known to play a dominant role in noise, vibration, and harshness (NVH) issues in electric drive units but remain insufficiently understood.

Finally, although experimental observations have confirmed the coexistence of electrical harmonics with gear mesh resonances, no comprehensive model has been developed that integrates nonlinear FE-based motor modeling with nonlinear gear transmission dynamics under realistic control strategies. This lack of integrated, high-fidelity modeling makes it difficult to predict dynamic behavior across the full operating envelope and limits the ability to design mitigation strategies at the system level.

In summary, the literature shows that while electromechanical coupling in electric powertrains has been acknowledged, existing studies have not yet provided a fully integrated nonlinear model that simultaneously accounts for:

- Detailed electromagnetic effects: Capturing spatial flux harmonics, magnetic saturation, and control-induced interactions inherent in interior permanent magnet (IPM) machines, which are critical for accurate prediction of torque ripple and its influence on drivetrain vibrations.
- Nonlinear drivetrain dynamics: Including gear mesh stiffness variations, backlash, and time-dependent coupling between gears, shafts, and bearings, so that the interplay between mechanical nonlinearities and electromagnetic excitations can be fully represented.
- Closed-loop control interactions: Reflecting the influence of nested current and speed control loops on torque delivery, transient response, and stability, especially under dynamic operating conditions.
- Comprehensive multi-source excitations: Accounting for the simultaneous effects of electromagnetic torque ripple, gear mesh vibrations, and external disturbances in steady-state operating regimes, enabling a holistic understanding of NVH phenomena.

Addressing these gaps requires the development of a high-fidelity, nonlinear electromechanical model that integrates FE-based motor analysis with detailed transmission dynamics under realistic control schemes. Such a model would not only bridge the current divide between electromagnetic and mechanical studies but also enable the systematic exploration of dynamic interactions that govern NVH behavior, reliability, and performance in modern electric powertrains.

1.4 Thesis objective and outline

This study undertakes a comprehensive investigation of torsional vibration phenomena within an electric powertrain system. Due to the intrinsic nonlinear characteristics of the system components, a hybrid modeling strategy is employed that combines analytical formulations with finite element (FE) simulations. Within this framework, the mechanical transmission is represented by a lumped-parameter model of a spur gear pair, where the effects of time-varying mesh stiffness and backlash are explicitly incorporated to capture the dynamic interaction between mating gear teeth. The drive shafts are formulated through equivalent torsional stiffness parameters that reproduce their elastic behavior, while bearing and support compliances are intentionally omitted in order to reduce model complexity without compromising the accuracy of the primary dynamic effects of interest.

The mechanical subsystem is coupled with an interior permanent magnet (IPM) motor, which is described through a nonlinear dynamic model constructed on the basis of FE-derived electromagnetic field data. This modeling approach allows the representation of magnetic saturation and spatial flux harmonics, both of which are essential for accurately capturing the electromechanical response of modern high-performance electric machines. The motor operates under a nested speed–current control strategy, designed to emulate realistic operating conditions and ensure that the interaction between electrical and mechanical domains is adequately represented. In this manner, the proposed modeling framework facilitates the examination of electromechanical coupling effects that are frequently excluded from conventional models, whether due to oversimplified mechanical assumptions or insufficient representation of IPM motor dynamics.

The developed methodology enables a detailed analysis of the powertrain's dynamic behavior under time-dependent torque excitations, which arise from both external loading and internal system interactions. Particular emphasis is placed on identifying the influence of these excitations on torsional oscillations and the associated transmission dynamics.

The remainder of this thesis is organized as follows. Section 2 presents the derivation of the theoretical models describing the mechanical transmission and IPM motor, followed by the integration of these subsystems into a unified electromechanical representation. Section 3 then reports and interprets the simulation results, including linear modal analysis, amplitude–frequency response characteristics, bifurcation patterns, and steady-state vibrational responses under different operating conditions. Special attention is given to the identification and interpretation of critical oscillatory phenomena. Finally, Section 4 synthesizes the key findings, discusses their implications for powertrain design and control, and outlines the principal findings.

Chapter 2: Analytical Model and Methodology

2.1 Introduction

The present chapter is dedicated to the analytical modeling methodology of the integrated motor-gear driveline. The first part is devoted to modeling of the nonlinear torsional vibration of the gear pair; a 3- degree of freedom oscillator with clearance-type non-linearity is considered to model the torsional dynamic behavior of the gear pair, neglecting the bearings. The main gear pair characteristics (mesh stiffness and inertia) are evaluated after an accurate geometrical modeling and a finite element analysis, including contact mechanics. Values for mesh stiffness are evaluated for different positions along one mesh cycle, and a Fourier expansion of the time-varying stiffness is carried out. The effect of the presence of manufacturing errors is neglected. The dynamical model presents a nonlinear time varying system of equations.

The second part focuses on developing a high-fidelity nonlinear model of the IPM motor and its integration with the gear system, addressing key gaps in existing electromechanical studies. A finite element (FE) motor model is first constructed, and electromagnetic field data are extracted over a full rotation cycle. These data are interpolated to build a nonlinear motor model that captures spatial flux harmonics and magnetic saturation effects, introducing the essential nonlinearities typically neglected in simplified models. A nested PI control strategy is implemented to reproduce realistic torque delivery and facilitate dynamic coupling between the motor and gear transmission. The resulting integrated motor–gear–control model establishes a unified framework for deriving the full set of nonlinear dynamic equations, enabling accurate simulation of multi-source interactions, transient phenomena, and coupled nonlinear electromechanical behavior.

2.2 Torsional Model of the system

The issue of gear-induced noise, known as gear whine, has been the subject of extensive investigation for a long time, yet interest in this phenomenon has intensified in recent years due to increasingly stringent regulatory limits on permissible noise emissions and heightened global competition, particularly within the automotive sector, where vibration and acoustic comfort is a key performance indicator. Among the various mechanisms contributing to vibratory and acoustic responses in geared systems, transmission error is widely recognized as a dominant source. This deviation between the actual and ideal kinematic motion of meshing gears generates dynamic forces that propagate through the gearbox structure, exciting the housing, shafts, and associated components. The resulting structural vibrations lead to the radiation of whine noise from the gearbox casing, making the accurate characterization and mitigation of transmission error a central focus in studies to improve the NVH performance of modern mechanical transmissions.

In this study to address the dynamic modeling of the objective system, lumped mass modeling is utilized. The lumped mass modeling method, also known as the lumped parameter model, is a foundational and widely used analytical technique for studying the dynamic behavior of spur gears. It simplifies a complex gear system into a collection of discrete rigid bodies (lumps) representing the gears, shafts, and inertia, which are interconnected by springs and dampers that model the flexibility and dissipation of the gear teeth, shafts, and bearings. The literature presents a range of analytical approaches employing lumped-parameter formulations for the dynamic analysis of spur gear pairs [51,75-76]. These dynamic models are generally classified into three categories: purely torsional, torsional–transverse, and fully three-dimensional representations [77]. The purely torsional model, originally introduced to examine torsional vibrations in spur gear pairs, is characterized by a single degree of freedom (DOF) [51]. At elevated operating speeds, however, rotating mass imbalances and gyroscopic effects induce gear vibrations in the radial (transverse) directions, commonly referred to as whirling vibrations [78-79]. Consequently, the torsional model has been extended to a torsional–transverse configuration that incorporates transverse vibratory motion; this model possesses three DOFs [80]. Nevertheless, the torsional–transverse model may be inadequate for analyzing the dynamic behavior of helical gear pairs, as these systems also generate axial forces. To address this limitation, a three-dimensional model with six DOFs has been developed by integrating axial and tilting motions into the torsional–transverse framework [76,78,81]. However, Özgüven et. al. [82] concluded that adding extra compliances and inertias to increase a model's degrees of freedom does not significantly improve the estimation of the dynamic stress or transmission-error predictions when the vibration modes are mostly uncoupled. However, if the mesh-stiffness-controlled torsional mode

interacts with other modes, the corresponding compliances must be included. In such cases, adding these compliances is more important than elaborating a single-DOF model with secondary effects like tooth friction.

Mechanical systems that incorporate clearances, gaps, or intentional tolerances within joints, bearings, or other contact interfaces often rely on intermittent contact to transmit motion or force between components. When such systems are subjected to periodically time-varying external forces or parametric excitations, their dynamic response becomes significantly more complex. This situation commonly arises in rotating machinery, where cyclic loading, geometric imperfections, and variations in operating conditions introduce time-dependent excitations that interact with the intrinsic nonlinearity of clearance interfaces. Numerous numerical [83-95] and experimental studies [96-98] have demonstrated the nonlinear vibration behavior of spur gears. Across these studies, the primary source of nonlinearity is attributed to intermittent loss of tooth contact associated with backlash nonlinearity.

Utilizing the lumped mass modelling approach and taking into account the coupling interaction between the electric motor and mechanical transmission system driven through the input shaft, we can demonstrate the representation of the objective system as a 3-DOF model. Figure 1 shows the 3-DOF lumped mass torsional model of the transmission, which represents a simple schematic of the system's dynamics. The effects which are included in the mathematical model and thus considered in the dynamic analysis are as follows: (1) time varying mesh stiffness and mesh damping; (2) torsional compliances of pinion and gear shafts; (3) material damping in shafts; (4) inertia of rotor, input and output shafts; (5) drive and load torques; (6) separation of teeth in mesh and backlash; (7) back side contact that may follow tooth separation.

Therefore, specifically, as can be observed in Figure 1, θ_m, θ_p, and θ_g are the angular displacements of the motor, the pinion, and the gear, respectively. The IPM motor is modeled using a disk of moment of inertia I_m, on which is applied an external torque T_m representing the electromagnetic torque, resulting from the interaction of the electromagnetic fields of the stator and rotor in the e-motor. The shaft, which connects the motor to the pinion, is assumed to be flexible, with torsional stiffness k_t^p and viscous damping c_t^p. The pinion and the gear are modeled by means of rotating disks with a base radius r_p and r_g and the moment of inertia I_p and I_g, respectively. Meshing gears are coupled along the line of action represented by a viscoelastic element with time-varying stiffness $k_m(t)$, and equivalent damping coefficient c_m. $2b$ represents the constant clearance, and lastly, a shaft, having

torsional stiffness k_t^g and viscous damping c_t^g, connects the gear to a fixed constraint, which represents a load characterized by a large inertia.

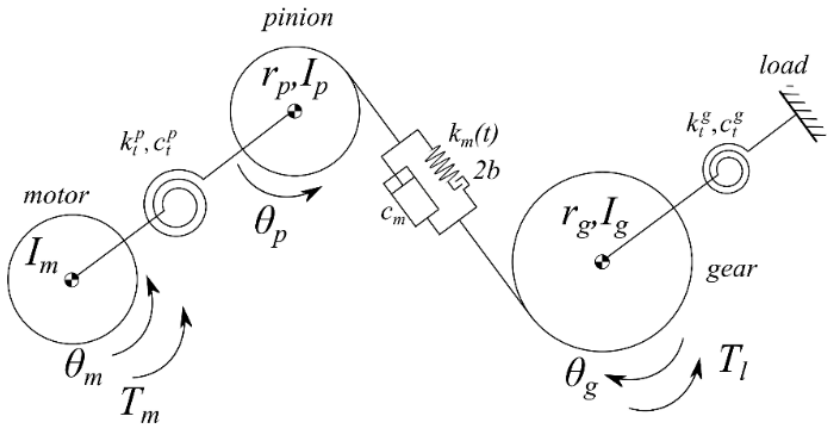

Figure 1 Schematic of the 3-DOF lumped mass torsional model

External torque T_l is applied to the gear, which represents the reference or the requested torque of the system. The torsional angle of the *j*-th disk is $\Theta_j = \Omega_j t + \theta_j(t)$, for *i=m, p,* and *g*, where the first term is related to the constant velocity of an ideal rigid driveline, and the second term accounts for deflection caused by elastic compliance.

Assuming a large load inertia I_l, the deflection can be approximated as $\theta_l(t) \approx 0$ for any *t*. Using the velocity relationship $\Omega_p = \Omega_m$, $\Omega_g = \Omega_m r_p / r_g$, and $\Omega_l = \Omega_g$, the system reduces to a 3-DOF torsional model of the driveline. By introducing the expression for the transmission error (DTE) along the line of action as:

$$x = r_p\theta_p - r_g\theta_g \tag{1}$$

The governing set of equations of the dynamics of the system can be expressed as in Eq. (2).

$$\begin{aligned} I_m\ddot{\theta}_m + c_t^p\left(\dot{\theta}_m - \dot{\theta}_p\right) + k_t^p\left(\theta_m - \theta_p\right) &= T_m \\ I_p\ddot{\theta}_p + r_p c_m\dot{x} + r_p k_m(t) f(x) + k_t^p\left(\theta_p - \theta_m\right) + c_t^p\left(\dot{\theta}_p - \dot{\theta}_m\right) &= 0 \\ I_g\ddot{\theta}_g - r_g c_m\dot{x} + r_g k_m(t) f(-x) + c_t^g\dot{\theta}_g + k_t^g\theta_g &= -T_l \end{aligned} \tag{2}$$

Where $f(x)$ is the piecewise linear backlash function, which accounts for clearance and potential backside contact, which is discussed in the following section (3.1.1). The TVMS, $k_m(t)$ is approximated using a Fourier series, where $\omega = z_p\Omega_p$ is the mesh frequency, with z_p denoting the number of pinion teeth, and Ω_p is the angular velocity of the pinion. The over-dot operator indicates differentiation with respect to time, *t*.

Dynamic analysis is made in the plane of gears, and any out-of-plane motion is neglected. As the excitation is basically along the line of action, the transverse vibration of gears in the direction perpendicular to the line of action is neglected. Another simplifying assumption made is to neglect the friction between the teeth in contact. Bearing compliances, transverse compliances of shafts, and gear errors, such as pitch, profile, and runout errors, and profile modifications are not considered in the model.

2.2.1 Nonlinear Backlash

Backlash is defined as the clearance between mating gear teeth. More precisely, it is the difference between the width of a tooth space on one gear and the thickness of the corresponding engaging tooth on the mating gear, both measured at their respective pitch circles. This intentional gap prevents interference, allows for lubrication, and accommodates manufacturing tolerances and thermal expansion.

Backlash may also be defined as the minimum distance between the surfaces of two mating teeth, measured along a line normal to the tooth surface, at the tightest point of mesh when the gears are installed in their proper, specified mounting positions. This definition emphasizes the physical clearance that exists even when the gears are positioned as closely as possible without binding.

In practical gear analysis, the value of backlash along the operating line of action (the path along which tooth forces are transmitted during engagement) can be calculated by projecting the tangential backlash at the pitch circle onto the line of action. This involves resolving the clearance into components aligned with the direction of tooth contact, typically using geometric relationships based on pressure angle and gear tooth geometry.

The value of backlash along the operating line of contact can be calculated as follows:

$$b = [s'_1 - ((2\pi r'_2 / Z_2) - s'_2)] * (r_{b1}/r'_1) \quad (3)$$

where s'_1 and s'_2 are the tooth thickness at the pitch circle of the gear pair, r'_1 and r'_2 are operating pitch radii of gear 1 and gear 2, respectively, r_{b1} is the base radius, and Z is the number of teeth.

The presence of clearances alters the effective stiffness and damping characteristics of the system, producing piecewise-linear or impact-driven behavior. As a result, generally, even small periodic excitations can induce highly nonlinear responses, including subharmonic and superharmonic resonances, bifurcations, intermittent contact or rattling, and transitions to chaotic motion. These phenomena contribute to a rich and intricate spectrum of dynamic behaviors that are not captured by traditional linear models. Understanding these nonlinear effects is therefore essential for accurate

prediction of system performance, early detection of faults, and the design of robust control and mitigation strategies in practical engineering applications.

Considering the contact of the gear pair as a 1-degree oscillator, representing the torsional motion, the equivalent model of the contact can be shown as in Figure 2. The system under consideration, as can be seen in Figure 1, comprises a nonlinear representation of a geared drivetrain in which the time-varying mesh stiffness and backlash clearance serve as the primary sources of mechanical nonlinearity. As can be seen, the presence of backlash introduces a clearance zone in which the teeth periodically lose and regain contact, producing impacts and discontinuities in the transmitted torque.

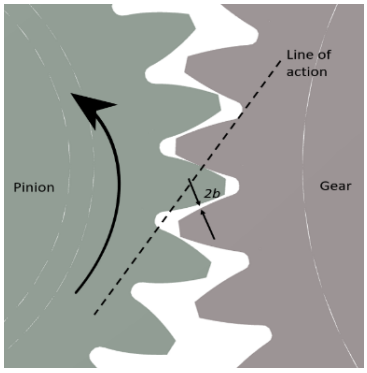

Figure 2 Backlash representation

As a result, the gear mesh is characterized by a constant clearance of $2b$, representing the fixed backlash along the line of action between mating teeth. Accordingly, the displacement-dependent restoring force is formulated through a specific functional relationship that captures the transition between no-contact regions and contact-engagement phases. This expression defines how the system responds mechanically as the relative displacement traverses the clearance threshold, thereby enabling the accurate representation of the nonlinear stiffness behavior inherent in gear meshing dynamics. Therefore, the displacement function, for which the restoring force is assumed, can be represented as the following expression:

$$f(x) = \begin{cases} x - b & x \geq b \\ 0 & |x| \leq b \\ x + b & x \leq -b \end{cases} \tag{4}$$

Where the backlash function is defined as a function of the relative displacement of the gear pair along the line of action or the dynamic transmission error (x). In the context of the present study, these general principles of clearance-induced nonlinearity and time-dependent excitation directly inform the modeling of the gear transmission–motor system. Gear mesh stiffness varies periodically with the rotation of the gears due to the changes in tooth contact conditions along the tooth profile. These features create a dynamic environment highly sensitive to parametric excitation and

intermittent contact phenomena. The following section is devoted to a description of the method for constructing the time-varying mesh stiffness.

2.2.2 Mesh Stiffness Evaluation

As it is explained in the previous section, the equivalent gear mesh model represented the discontinuity of the contact in the dynamical model. Since the number of tooth pairs in contact varies throughout the mesh cycle as the gears mesh each other, the mesh stiffness is inherently time-dependent and fluctuates in accordance with the instantaneous contact conditions. Consequently, the dynamic mesh force cannot be represented by a single constant value; rather, it must be treated as a continuous, periodically varying quantity that evolves over each rotation of the gears. The periodic modulation of mesh stiffness as an internal periodic excitation source leads to a corresponding continuous change in tooth deflection, which directly affects the instantaneous angular transmission error. The dynamic nature of this error introduces periodic excitation into the gearbox system, promoting structural vibrations that propagate through the housing and associated components, ultimately resulting in the generation and radiation of noise during gear operation.

In this study, the main gear pair characteristic, i.e., mesh stiffness, has been evaluated after an accurate geometrical modeling and a finite element analysis, including contact mechanics through FE simulations conducted with Transmission 3D software [99].

FEA has become an important tool in engineering design thanks to advances in computational power, which enable the simulation of complex systems. However, some mechanical applications, such as gear systems, remain challenging due to their intricate kinematics and the significant influence of components like gearboxes, shafts, and bearings. Accurately modeling gear-tooth contact with a general nonlinear finite element program requires extremely fine meshing in the contact zone, which must smoothly transit to a coarser mesh elsewhere on the gear. Because the contact zone shifts as gears rotate, the model would either need to be continuously remeshed or remain highly refined over the entire surface. Both approaches result in computational costs that are impractically high. Transmission 3D addresses these difficulties by using a specialized semi-analytical finite element approach combined with detailed tooth-contact modeling. This method captures the behavior of precisely machined, elastic gear bodies while avoiding the need for extremely fine meshing at the contact surfaces, resulting in accurate simulations with significantly reduced computational time.

The contact solver used in Transmission 3D is based on the Revised Simplex solver [100]. This solver is commonly used to solve quadratic programming problems. It also provides a guarantee of convergence within a predetermined number of iterations. It is specifically designed for the linear

inequality type constraints found in contact problems. The nominal position of each individual gear in the system changes with time, determined by the kinematics of the system. Generally, it is very difficult to include this kinematic information into a finite element program. Transmission 3D has a special-purpose programming language built into the software in order to specify the details of the kinematics of each component in the system. Important details such as the kinematics effect of assembly errors, runout, and misalignments are easy to apply using this approach.

Figure 3 geometrical and material characteristics of the gear pair

The reconstruction of the gear mesh stiffness is performed based on the evaluation of the static transmission error (STE) over a full mesh cycle using 15 discrete mating positions. To this end, the geometrical and material properties of the gear pair are first defined and modeled in Transmission 3D, as illustrated in Figure 3. Figure 4 represents the gear pair modeled in the FE software to be analyzed statically. Post-processing of the FE results provides the static transmission error in the form of a body deflection quantity, which is then used for the subsequent mesh stiffness reconstruction.

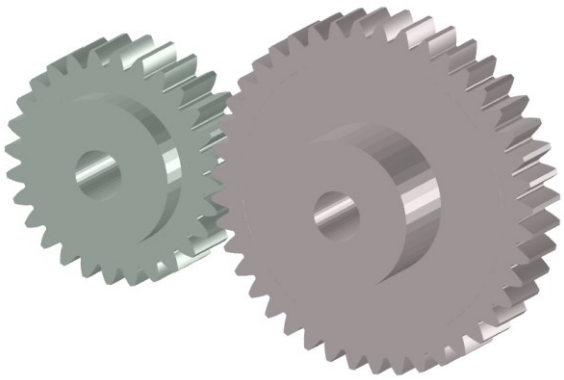

Figure 4 The gear pair constructed in Transmission 3D

After constructing the gear pair model in the software and defining its geometrical and material properties, the validity of the model must be verified. This is achieved by evaluating the contact pressure distribution along the tooth contact surface.

A physically consistent result is indicated by a contact pressure profile that exhibits higher values near the center of the tooth face and lower values toward the edges. Such a distribution confirms appropriate contact conditions and the reliability of the post-processed results. If this pattern is not observed, the simulation parameters must be revised. Figure 5 illustrates a computational grid arranged in the contact area of a gear tooth face.

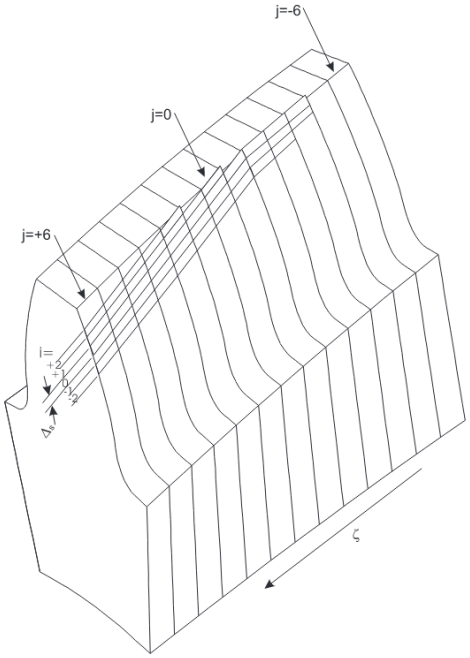

Figure 5 Computational grid of the contact region

The full tooth face width is divided into $2N+1$ sections, where N is a user-defined parameter (NFACEDIVS in Figure 6). A parameter ζ varies from -1 at one edge of the face width to $+1$ at the opposite edge, so the width of each section in ζ space is $\Delta\zeta = 2/(2N+1)$. For every slice $j = -N \ldots +N$, the tooth cross-section is taken at the slice midpoint, and a point on this cross-section is located that lies closest to the surface of the mating tooth. This step is based on the undeformed geometry. If the gap between the two gears at this closest point is greater than a user-defined separation limit (SEPTOL in Figure 6), that slice is excluded from further analysis. Otherwise, a grid of cells with indices i, where $i = -M \ldots +M$, is created around the closest point of the slice. The value M (NPROFDIVS in Figure 6) is also user-specified. The cell size in the profile direction, Δs (DSPROF in Figure 6), is another user-defined quantity, where s represents the arc-length along the profile. The parameter Δs is the grid cell width along the profile (DSPROF). The total grid width is therefore $(2M+1).\Delta s$.

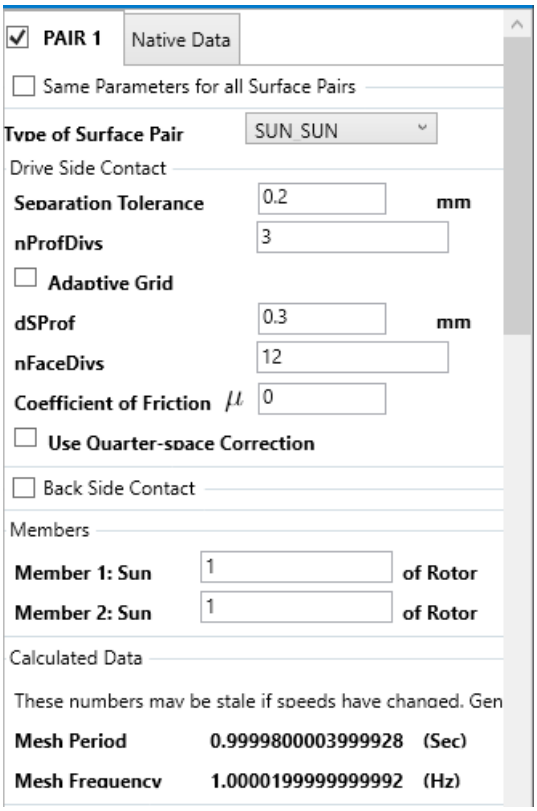

Figure 6 Cotact grid setting

Selecting an appropriate grid width is essential for accurate contact pressure results. If the grid is too wide while M is fixed, the resolution decreases because only the central cell ends up carrying the load. On the other hand, if the grid is too narrow, the contact region is cut off, leading to unrealistically high edge pressures. When the grid width is chosen correctly, the resulting pressure distribution will resemble the pattern shown in Figure 7.

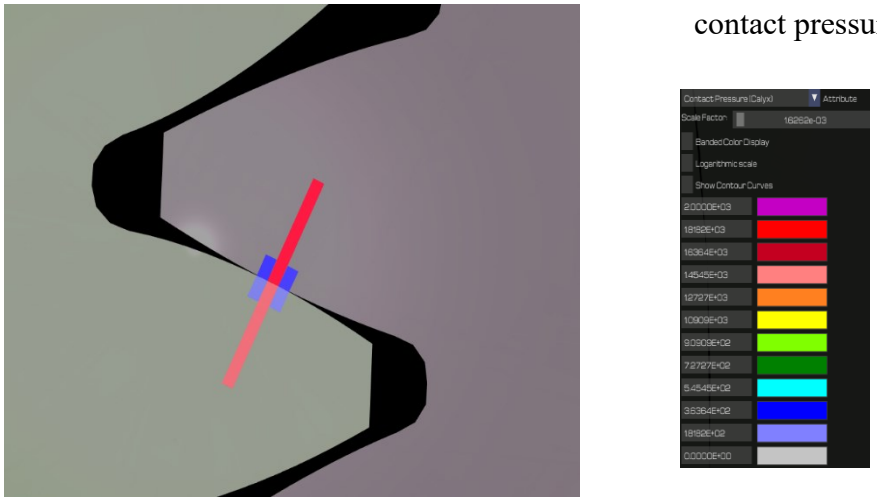

Figure 7 Pressure distribution in the contact zone

Fifteen equally spaced positions on the gear flank are analyzed to obtain the driver shaft rotation δ. The contact point between the gears at the first analyzed position is the pitch point. The parameter δ_i (normally expressed in radians) is obtained by taking the mean tangential displacement of the nodes

situated on the pinion's inner circumference at position i. The static transmission error along the line of action (typically given in micrometers) is then determined at each increment using the following formula:

$$STE = \delta_i * r_b \qquad i=1, \ldots, 15 \qquad (5)$$

Figure 8 shows an example of the post-processed values of δ in one mesh cycle, retrieved from the static simulation in Transmission 3D. As can be observed, from positions 5 to 12, two pairs of teeth are in contact, while for the remaining positions, one pair of teeth is in contact.

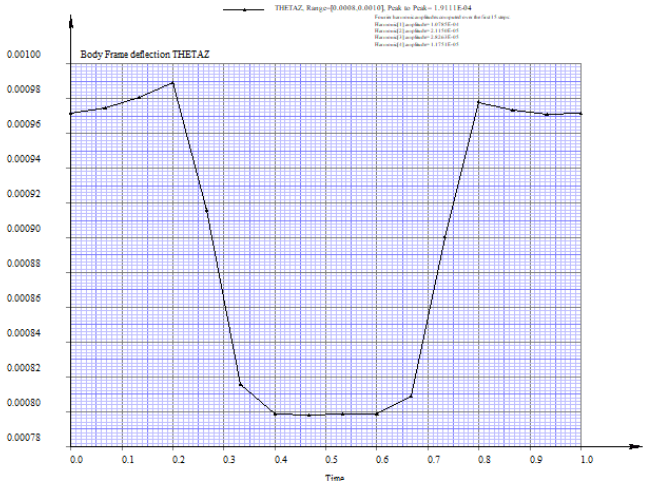

Figure 8 Static transmission error along the mesh cycle

The stiffness k is evaluated for each position by using the following relationship, which also transforms the torsional stiffness into the linear stiffness along the line of action:

$$K_i = \frac{T}{\delta_i * {r_b}^2} \qquad i=1, \ldots, 15 \qquad (6)$$

Therefore, by applying this formulation, the time-varying mesh stiffness can be seen in Figure 9

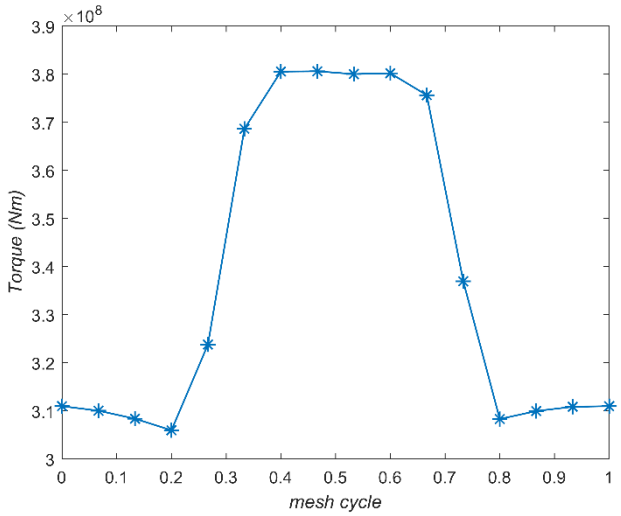

Figure 9 time-varying mesh stiffness along the mesh cycle

In order to obtain a continuous representation of the gear mesh stiffness over time, considering that the time-varying mesh stiffness (TVMS) exhibits a periodic behavior that is directly related to the mesh period of the gears, the discrete data set of stiffness values K_i, previously extracted from the finite element simulations at successive angular positions of the rotating gears, is transformed into the frequency domain by means of a discrete Fourier transform (DFT). This transformation enables the identification of the dominant harmonic components that characterize the periodic fluctuation of the stiffness. Subsequently, a Fourier series expansion of the TVMS is constructed by retaining the relevant frequency components obtained from the DFT. In this way, the originally discrete FE-based stiffness data are expressed as a continuous analytical function of angular position, thereby providing a suitable formulation for incorporation into the dynamic model of the gear transmission.

Consequently, the IPM motor is coupled to the mechanical subsystem which supplies torque through a compliant shaft that further influences the system's dynamic characteristics. The shaft compliance introduces additional elastic and damping effects, enabling torsional vibrations to interact with the nonlinear gear meshing process. When the periodically varying mesh stiffness, backlash nonlinearity, and motor–shaft dynamics are combined, the resulting model captures a wide array of nonlinear behaviors including amplitude-dependent resonances, modulation effects, and possible bifurcations that arise in practical drivetrain operation. This integrated nonlinear model therefore provides a realistic and comprehensive framework for analyzing the complex dynamic response of geared electromechanical systems, and it serves as a foundation for understanding how structural clearances, parametric excitations, and drivetrain elasticity jointly shape system performance and stability. In the next section the methodology to model the IPM motor and the nested PI control strategy are presented

2.3. Internal Permanent Magnet Synchronous Motor (IPM)

2.3.1 Introduction

Permanent-Magnet Synchronous Machines (PMSMs) have gained significant attention in both academic research and industrial applications owing to their outstanding electromagnetic performance characteristics. One of the most notable features of PMSMs is their high torque density, which enables the generation of greater torque output for a given machine volume compared to conventional motor types. This advantage primarily stems from the fact that the air-gap magnetic field, responsible for electromechanical energy conversion, is predominantly produced by permanent magnets embedded in or mounted on the rotor surface. Consequently, PMSMs do not require external excitation current to establish the main magnetic field, unlike traditional electrically excited synchronous machines.

The absence of rotor excitation windings leads to several performance and efficiency benefits. Firstly, it eliminates copper losses in the rotor circuit, significantly improving energy efficiency and reducing heat generation. Secondly, the simplified rotor structure enhances mechanical reliability and minimizes maintenance requirements. Furthermore, PMSMs exhibit superior dynamic response and high-power factor, which contribute to their effectiveness in systems requiring fast and precise torque control. These attributes make PMSMs particularly attractive for applications where compactness, lightweight design, and high efficiency are critical design objectives.

Owing to these characteristics, PMSMs have been increasingly adopted across a wide spectrum of modern electromechanical systems. In the industrial sector, they are extensively used in precision motion control systems, robotic actuators, and high-performance servo drives, where accurate speed and position control are essential. In the automotive industry, PMSMs serve as the core propulsion technology for hybrid and fully electric vehicles (HEVs/EVs) due to their high power-to-weight ratio and ability to operate efficiently over a broad speed range. Similarly, in the renewable energy domain, PMSMs are widely integrated into wind turbine generators, particularly in direct-drive configurations, which eliminate gearboxes and enhance overall reliability and energy conversion efficiency.

Beyond these sectors, PMSMs also play an essential role in aerospace and marine propulsion systems, where the demand for lightweight, efficient, and maintenance-free power units is growing rapidly. Recent advancements in magnetic materials, such as the development of high-performance rare-earth magnets (NdFeB and SmCo), as well as improvements in power electronic converters and

control algorithms, have further broadened the practical application range of PMSMs and enhanced their operational efficiency.

Overall, the combination of high torque density, superior efficiency, and robust control performance positions PMSMs as one of the most promising technologies for current and future electrical drive systems. Ongoing research continues to focus on optimizing machine topology, mitigating torque ripple, improving thermal management, and developing cost-effective alternatives to rare-earth magnets, all of which are aimed at expanding the feasibility and sustainability of PMSM technology in emerging applications.

The surface-mounted permanent-magnet (SPM) configuration represents one of the simplest and most widely adopted rotor structures. In this design, the permanent magnets are affixed directly onto the rotor surface, such that the magnetic field generated by the magnets interacts directly with the stator-produced armature field. The developed electromagnetic torque in SPM machines arises purely from the alignment torque component, which results from the interaction between the stator's rotating magnetic field and the rotor's constant magnetic field produced by the surface-mounted magnets. SPM configuration does not exploit magnetic saliency, and thus no reluctance torque is produced. Since, the magnets are located on the rotor surface, the effective air gap experienced by the stator winding is relatively large. This effective gap is equivalent to the sum of the physical air gap and the thickness of the magnet layer. The increased magnetic separation between the stator and rotor reduces the degree of magnetic coupling, which in turn makes the armature reaction comparatively weak. As a result, the stator flux linkage is less sensitive to variations in the armature current, and the winding inductances remain nearly constant regardless of the rotor position. This property greatly simplifies the mathematical modeling and vector control of SPM machines, making them well-suited for applications where precise torque and speed control are required, and where modeling simplicity is advantageous.

However, the structural simplicity of SPM machines comes with certain performance trade-offs. Due to the absence of a reluctance torque component, all the torque is produced solely through the permanent-magnet field, which means that a relatively larger volume of magnetic material is required to achieve a given torque output. This not only increases the cost and weight of the machine but also introduces potential issues related to magnet demagnetization at high operating temperatures. Additionally, since the torque production relies entirely on the magnetic flux, SPM machines exhibit limited capability for flux weakening at high speeds. This restricts their ability to maintain constant power output over a wide speed range, making them less suitable for applications demanding an extended constant power operating region, such as electric traction or high-speed spindle drives.

To overcome the limitations associated with surface-mounted permanent magnet (SPM) machines particularly their poor field-weakening capability and high dependence on permanent-magnet material, interior permanent magnet (IPM) machines have been developed and widely adopted. In IPM machines, the permanent magnets are embedded within the rotor iron rather than mounted on its surface. This configuration not only provides mechanical protection for the magnets but also enables the exploitation of magnetic saliency, thereby allowing both magnetic torque and reluctance torque components to contribute to the total electromagnetic torque. Consequently, IPM machines exhibit enhanced field-weakening performance, reduced reliance on rare-earth magnet materials, and improved overall operational efficiency, especially in applications requiring a wide constant power speed range.

However, the presence of reluctance torque introduces certain modeling and control challenges. In other word, the electromagnetic torque in IPM machines depends nonlinearly on both the d-axis and q-axis current components. This nonlinearity arises from the interaction between the magnetic saliency and the embedded magnets, as well as from the saturation of the stator and rotor cores. As the rotor position changes, the magnetic reluctance path varies significantly, leading to periodic variations in stored magnetic energy. These variations give rise to spatial harmonics in the air-gap flux density, which are then reflected in the induced phase voltages and can degrade waveform quality.

Due to these effects, the simplified mathematical models that assume constant d- and q-axis inductances (L_d and L_q) are insufficient to accurately capture the true behavior of IPM machines under practical operating conditions. In reality, the inductances vary with both current magnitude and rotor position, particularly under high load and deep saturation. This becomes especially critical in the field-weakening region, where the terminal voltage of the machine approaches the limit imposed by the inverter DC-link voltage. In this region, the presence of voltage harmonics and nonlinear inductance variation can lead to distorted current waveforms, reduced control precision, and increased torque ripple. Therefore, to model and control IPM machines effectively, it is essential to employ advanced modeling approaches that account for magnetic saturation, cross-coupling effects, and spatial harmonic components. Finite element analysis (FEA) and look-up table (LUT)-based models are frequently utilized for this purpose. In parallel, advanced control strategies such as nonlinear current control, adaptive field-weakening algorithms, and harmonic compensation techniques have been proposed to mitigate the adverse effects of nonlinearities and maintain smooth torque production across the entire operating range.

2.3.2 Dynamics of IPM

To address the problems associated with the conventional modeling methods, a flux-linkage-based machine model is employed. The conventional *d* and *q*-axis equivalent circuit model (ECM) is the most widely adopted method for modeling synchronous machines, as it simplifies the model implementation [109]. Applying this method, the PMSM stator voltage equations in the synchronous rotating reference frame (d–q) can be expressed as:

$$\begin{aligned} V_d &= RI_d + \dot{\lambda}_d - p\dot{\Theta}_m\lambda_q \\ V_q &= RI_q + \dot{\lambda}_q + p\dot{\Theta}_m\lambda_d \end{aligned} \tag{7}$$

Where V_d and V_q are the stator voltages, R is the phase resistance, I_d and I_q are the stator current components, $\dot{\Theta}_e = p\dot{\Theta}_m$ is the rotor speed in the electrical reference frame, p is the number of pole pairs, and λ_d and λ_q are the flux components. Based on this modeling approach, the dynamic characteristics of the IPM are described by a system of nonlinear differential equations that couple the electrical variables of the stator and rotor (currents and voltages) with the corresponding mechanical variables (torque, speed, and angular position) [110].

Knowing that the flux components are functions of currents and rotor position, i.e., $\lambda_d(I_d, I_q, \Theta_m)$ and $\lambda_q(I_d, I_q, \Theta_m)$, Eqs. (7) can be rearranged as:

$$\begin{aligned} V_d &= R\mathrm{I}_d + \frac{\partial\lambda_d}{\partial I_d}\dot{I}_d + \frac{\partial\lambda_d}{\partial I_q}\dot{I}_q + p\dot{\Theta}_m\left(\frac{1}{p}\frac{\partial\lambda_d}{\partial\Theta_m} - \lambda_q\right) \\ V_q &= R\mathrm{I}_q + \frac{\partial\lambda_q}{\partial I_d}\dot{I}_d + \frac{\partial\lambda_q}{\partial I_q}\dot{I}_q + p\dot{\Theta}_m\left(\frac{1}{p}\frac{\partial\lambda_q}{\partial\Theta_m} + \lambda_d\right) \end{aligned} \tag{8}$$

Where the partial derivatives of the flux components with respect to d-q currents represent the motor differential inductances. To solve this system of equations expressed in (8), the current time derivatives must be defined explicitly to be integrated over time. This is achieved by inverting Eqs. (8) to define current derivatives as a function of d-q currents, voltages, and rotor position.

To accurately capture and model the electromagnetic behavior of the PMSM, it is essential to account for the nonlinear and state-dependent characteristics of the machine's magnetic field distribution. In practical PMSMs, especially interior types, the magnetic flux paths and inductances are not constant, but vary with the stator current components and the rotor position due to magnetic saturation, cross-coupling effects, and rotor saliency. As defined in Eqs. 8, the electromagnetic quantities needed for the model are the flux linkages and the differential inductances. However, if iron losses in the machine stator and rotor cores are neglected, an important property relates these quantities: the flux linkage components, λ_d, λ_q represent a conservative field which admits a scalar

potential function, represented by the magnetic co-energy, W_c stored in the motor. Consequently, both flux linkages and differential inductances can be obtained from the differentiation of co-energy as Eq. (9) and Eqs. (10) respectively.

$$\lambda_d = \frac{2}{3}\frac{\partial W_c}{\partial I_d} \;\; ; \;\; \lambda_d = \frac{2}{3}\frac{\partial W_c}{\partial I_q} \tag{9}$$

$$L_{dd} = \frac{\partial \lambda_d}{\partial I_d} = \frac{2}{3}\frac{\partial^2 W_c}{\partial I_d^2}, \qquad L_{dq} = \frac{\partial \lambda_d}{\partial I_q} = \frac{2}{3}\frac{\partial^2 W_c}{\partial I_q \partial I_d} \tag{10}$$

$$L_{qd} = \frac{\partial \lambda_q}{\partial I_d} = \frac{2}{3}\frac{\partial^2 W_c}{\partial I_d \partial I_q}, \qquad L_{qq} = \frac{\partial \lambda_q}{\partial I_q} = \frac{2}{3}\frac{\partial^2 W_c}{\partial I_q^2}$$

Moreover, the PMSM electromagnetic torque is obtained from co-energy as:

$$T_m = \frac{3}{2}p(\lambda_d I_q - \lambda_q I_d) + \frac{\partial W_c}{\partial \Theta_m} \tag{11}$$

Where, $\frac{\partial W_c}{\partial \Theta_m}$ is the cogging torque component given by the partial derivative of co-energy with respect to the mechanical angle.

Accurately determining these relationships is fundamental for precise modeling, performance prediction, and control design. Simplified analytical models often assume constant d and q-axis inductances and neglect spatial harmonics and saturation effects; however, such assumptions lead to significant errors in estimating torque and flux, particularly in high-performance or high-load operating conditions. In practice, obtaining these quantities typically requires finite element analysis (FEA) or experimental characterization. These methods provide detailed insight into how the flux linkages, magnetic co-energy, and torque vary throughout the machine's operating range. The resulting data can then be stored in look-up tables or expressed through analytical fitting manifolds for use in control algorithms and dynamic simulations.

In this study, FEA, "Altair" software package, is utilized to model the IPM and retrieving the fluxes, electromagnetic torque, and magnetic co-energy data. The magnetic co-energy data are first obtained through Altair, accurately capturing the nonlinear behavior of the ferromagnetic materials and rotor position-dependent ripples in torque and fluxes. Secondly, the co-energy data are interpolated across a grid (i_d, i_q, Θ_m) of operating points using a three-dimensional cubic-spline. Periodic end-point conditions are imposed for the rotor angle coordinate, with periodicity every $2\pi/p$, while, for currents, 'not-a-knot' boundary conditions are assumed to impose the continuity of the third derivative at the endpoints [111]. Once W_c is built, flux components and differential inductances are obtained via closed-form differentiation of the co-energy. This approach avoids the introduction of

numerical error that would be introduced if numerical differentiation were applied instead, and complies also with the energy conservation hypothesis, which leads to Eqs (9, 10).

The IPM case in this study is considered as a 12-pole, 72-slots heavy-duty IPM traction motor and has been modeled based on the parameters in Table 1. The geometry of the motor is shown in Figure 10

Table 1 Electric motor and PI controllers' characteristics

Motor's parameters		Unit
Number of poles	12	-
Number of slots	72	-
Stator phase resistance R_s	0.02	Ω
DC-Link voltage V	650	V
D-axis inductance, unsaturated L_d	0.156	mH
Q-axis inductance, unsaturated L_q	0.308	mH
Magnet flux linkage, unsaturated λ_m	0.129	Wb

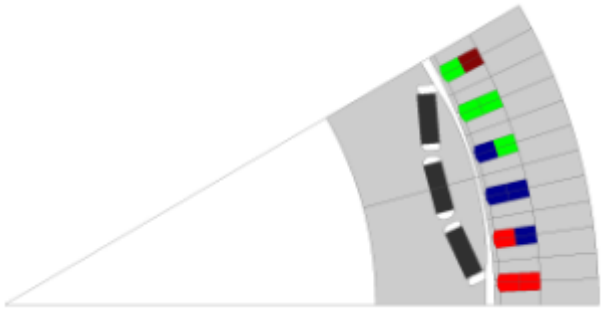

Figure 10 IPM motor geometry representation

By modeling the IPM motor, we are able to retrieve the data which are then necessary for the dynamic simulation.

An important point to notice is that the electrical model equations (Eqs. (7-11)) are formulated as continuous functions of the state variables, reflecting the actual behavior of the underlying physical quantities. In contrast, FE analyses and experimental measurements cannot supply such continuous information; they only yield numerical values at a discrete set of operating points. Therefore, to determine flux and inductance at an arbitrary operating condition, an appropriate interpolation strategy is required.

Specifically, in this case, the interpolation approach must satisfy two main criteria:

- It must ensure smooth transitions between the nodes of the data grid.
- It must preserve the principle of energy conservation.

The first requirement stems from the need for transitions between sampled data to appear realistic and physically consistent, meaning that the interpolating functions should exhibit at least C^1 continuity. The second requirement acknowledges that the model's quantities are physically interconnected and must retain their inherent relationships. For instance, when hysteresis and eddy-current effects are neglected, the flux linkage components form a conservative vector field. As such, they share a common potential function, which in this case is the magnetic co-energy. It is important to note that using a method like bilinear interpolation directly on the flux components would violate this property, because two independent bilinear functions cannot originate from a single potential.

The most straightforward way to satisfy the energy-conservation constraint is therefore to interpolate the co-energy itself and then obtain all dependent quantities by differentiating it with respect to the relevant coordinates. In this study, three-dimensional cubic-spline interpolation is employed for this purpose, as it satisfies the property of being twice continuously differentiable. Moreover, the derived quantities are obtained via closed-form differentiation of the polynomials defining the interpolating function, avoiding the numerical error that would be introduced if numerical differentiation were applied instead.

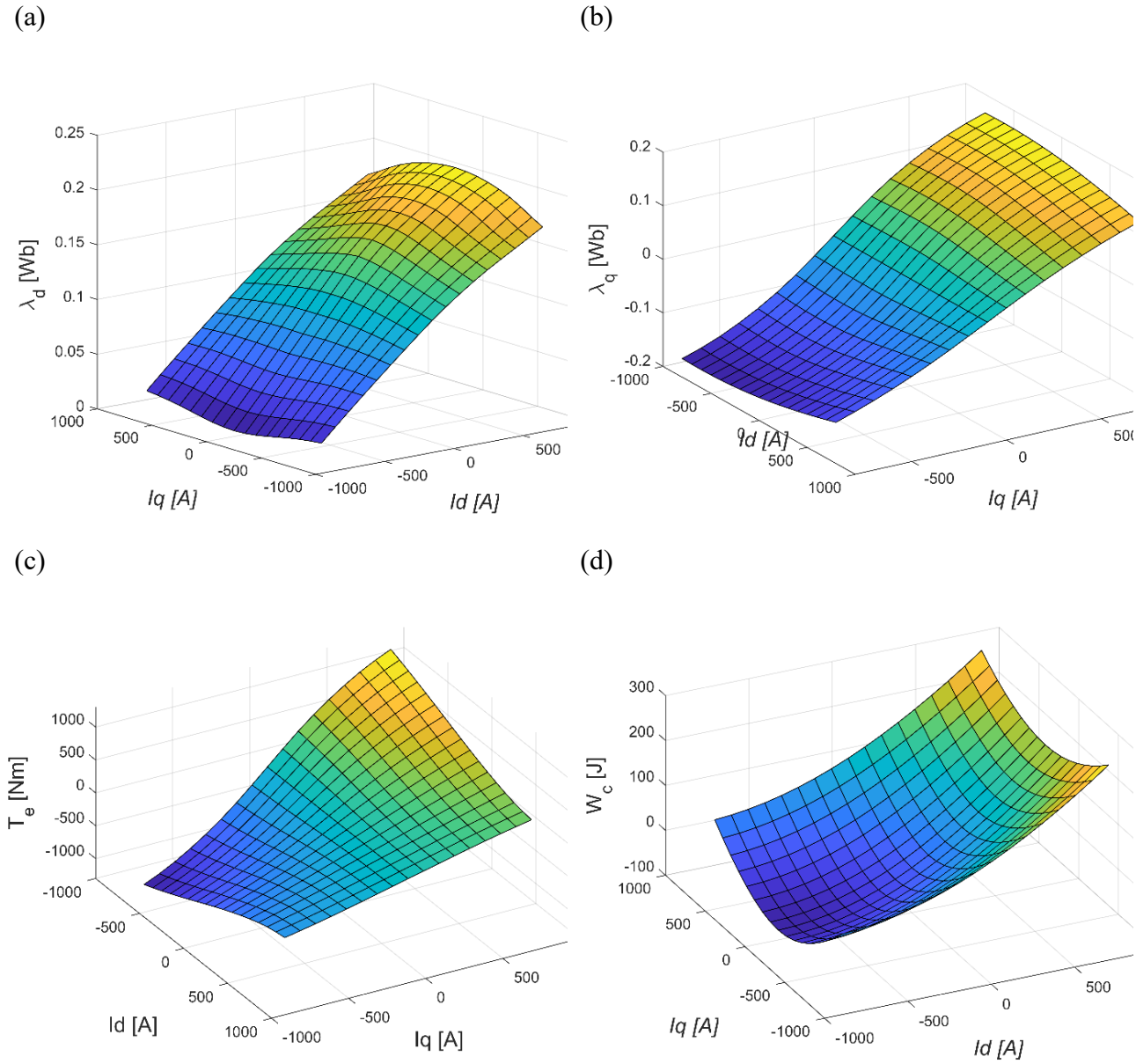

Figure 11 Manifolds based on the data retrieved from FEA modelling of the IPM

2.3.3 Nested PI controller system

Applying a dedicated and well-designed control strategy in an electric drive system is essential to ensure stable, efficient, and predictable operation under varying electrical and mechanical conditions. Since electric motors are inherently nonlinear systems whose performance is influenced by factors such as load variations, back-EMF dynamics, parameter changes, and electrical limitations, without a proper control structure, the motor would not be able to regulate its torque or speed effectively, leading to undesirable behavior like slow response or instability. In practical applications, motors must maintain a specified speed or torque despite disturbances, sudden load changes, or fluctuations in supply voltage. Control ensures that these performance requirements are met by continuously adjusting the electrical inputs to the motor.

Furthermore, control is necessary to protect the motor and power electronics from excessive currents or voltages that may arise during transients or unexpected disturbances. Limiting and shaping the current is crucial for preventing overheating and avoiding damage to the inverter or motor windings. A well-designed control system improves the overall energy efficiency of the drive by ensuring that the motor operates at conditions that minimize losses. Additionally, control allows the motor to produce the required torque with high accuracy, enabling smooth operation of the mechanical system it drives.

Finally, modern electric drive applications, such as electric vehicles, impose stringent requirements on dynamic performance, responsiveness, and operating safety. Meeting these demands is only possible through a structured control strategy that manages the multi-time-scale dynamics of the motor. Therefore, the application of control is fundamentally necessary to achieve reliable performance and meet operational objectives in real-world systems. Without a control strategy, particularly closed-loop control, the motor's behavior would be unpredictable under varying operational conditions.

The design of current and speed controllers relies on key machine parameters, including flux linkage, stator resistance, and the d- and q-axis currents. However, these parameters can vary from their nominal values under different operating conditions. Factors such as magnetic saturation, temperature changes, and long-term aging influence their accuracy. Elevated temperatures, for example, alter both the stator resistance and the machine’s flux linkage, while magnetic saturation primarily affects the inductances.

In this study, the operational objectives of the system are the load torque requested by the output shaft and the operational speed of the input or the rotor shaft. Two feedbacks (closed-loop) PI controllers are employed in a nested configuration:

- The inner current-control loop, characterized by a large bandwidth, regulates voltages through the stator currents. The proposed scheme modifies the current reference using the interpolation of the outputs of two look-up tables for the different PM currents
- The slower outer loop regulates the electromagnetic torque based on the rotor angular velocity. The outer PI control is applied to control the speed requested by the shaft. Indeed, the reference speed is set as the target speed for the input shaft or the rotor, and the error is obtained by the difference between the actual rotor speed given as the feedback from solving the mechanical equations and the target shaft speed.

The following step-by-step procedure is proposed to facilitate the design process and to present the entire procedure of designing the nested-feature control strategy in a comprehensive manner. The step-by-step procedure for designing the PIs of the nested strategy is divided into two parts: one for the current controller and another for the speed controller, as follows.

A): Current PI controllers:

The inner feedback controller is described by the following relationships:

$$V_d = K_{pI_d}(I_d^*(T_m^*) - I_d) + \int K_{iI_d}(I_d^*(T_m^*) - I_d)\, dt$$
$$V_q = K_{pI_q}\left(I_q^*(T_m^*) - I_q\right) + \int K_{iI_q}\left(I_q^*(T_m^*) - I_q\right)dt \quad (12)$$

where $(\cdot)^*$denotes the setpoint, and reference currents $I_d^*(T_m^*), I_q^*(T_m^*)$ are nonlinear functions of the reference torque and they are evaluated by interpolation of the look-up tables' data obtained from FE simulations. Figure 12presents a simplified control strategy block diagram for designing the current controllers. Note that such a simplified diagram is valid due to the decoupling scheme. Moreover, the simplified diagram is intended to enable the use of the proposed methodology for designing the PIs of the nested-feature strategy.

1st step: knowing the system parameters: The first step in designing the PI Control for IPM is to know the system parameters. Table 2 shows the parameters and their unit that must be identified in the 1st step of designing the control strategy.

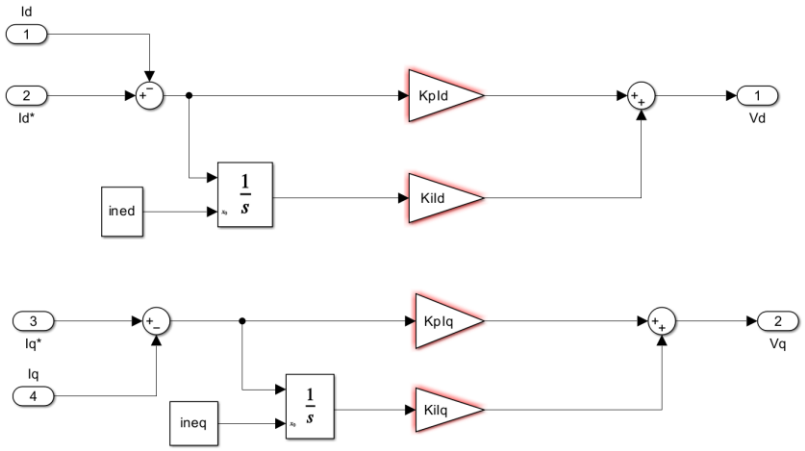

Figure 12 Simplified control strategy block diagram for designing the current controllers

Table 2 Neccessary parameters and their units.

Parameters	Unit
Stator Resistance (R_s)	Ω
d-axis inductance (L_d)	H
q-axis inductance (L_q)	H
Inverter switching frequency	Hz
Equivalent moment of inertia (I)	$Kg\ m^2$

2nd step: defining the desired time constant for the current controllers: The second step is to define the desired closed-loop time constant for the current controllers. Such a time constant is defined as τ, and its unit is seconds. τ should be small for a fast response, but large enough because 1/τ is the bandwidth of the closed-loop system. However, 1/τ must be at least 10 times lower than the switching frequency (in rad/s) of the inverter (The objective study does not include the inverter, thus here, the choice of bandwidth (ω_b)is not based on the switching frequency of the inverter). The time constant is usually chosen in the range of 0.5 *ms* to 2 *ms*.

3rd step: computing the proportional and integral gain of the d-q axis PI controller: The tuning parameters of the controller are given as:

$$K_{pId} = \omega_b * L_d \tag{13}$$

$$K_{pIq} = \omega_b * L_q$$

$$K_{iId} = K_{pId} * R_s/L_d$$

$$K_{iIq} = K_{pIq} * R_s/L_q$$

By using these values for proportional and integral gain of the PI controllers, a pole-zero cancellation happens, and the open-loop transfer function will be a simple integrator that has a gain of zero dB at the cutoff frequency that corresponds to the chosen time constant.

B): Speed PI controller:

The speed feedback controller is described by the following relationships:

$$T_m^* = K_{p\Omega}(\dot{\Theta}_m^* - \dot{\Theta}_m) - \int K_{i\Omega}(\dot{\Theta}_m^* - \dot{\Theta}_m)\, dt \tag{14}$$

The angular velocity of the rotor shaft is $\dot{\Theta}_m = \Omega_m + \dot{\theta}_m$, and $\dot{\Theta}_m^* = \Omega_m$ which indeed corresponds to the set or target speed of the rotor shaft. Therefore, this relation can be expressed as follows:

$$T_m^* = -K_{p\Omega}\dot{\theta}_m - K_{i\Omega}(\theta_m + C) \tag{15}$$

where C is an integration constant. This equation is obtained under the assumption that $\dot{\Theta}_m^* = \Omega_m$, a condition arising from the procedure adopted for the bifurcation analysis, which will be clarified in the following section. Figure 13 presents the control strategy block diagram for designing the speed controller.

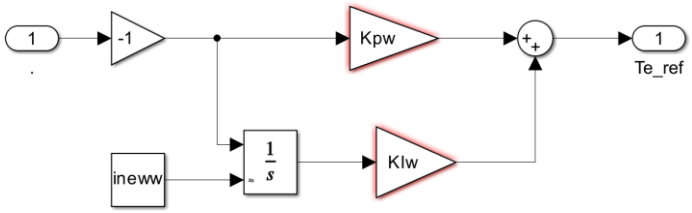

Figure 13: Control strategy block diagram for designing the speed controller

1st step: defining the desired time constant for the speed controller: The first step in designing the speed controller is to define the desired time constant. In order to make the inner and outer loop decoupled and the inner loop unitary, the time constant for the speed controller must be at least ten times higher than the time constant of the current control. Indeed, a rule of thumb from the control system theory says that the cut-off frequency (ω_c) of an outer loop must be ten times lower than the cut-off frequency bw for an inner loop. By doing that, the inner and outer loop has no coupling effects, and they can be designed individually.

$$\omega_c = 0.1 * bw \tag{16}$$

2nd step: computing the proportional and integral gain of the speed controller: The proportional and integral gain of the speed controller are as following:

$$K_{p\Omega} = \omega_c I_{eq} \tag{17}$$

$$K_{i\Omega}=\omega_c^2 \frac{I_{eq}}{10}$$

where, ω_c stands for the speed controller cut-off frequency and I_{eq} is the equivalent moment of inertia which is retained from the role of motor, pinion, and gear, i.e., $I_{eq} = I_m + I_p + I_g$ [112, 113].

The block diagram of the proposed nested PI controller strategy is represented in Figure 14. As can be observed, the outer control input is $\dot{\theta}_m$ which is given as feedback from the dynamic equation solver of the model, and the inner control inputs are I_d and I_q which are the feedback given from the electric equation solver of the model.

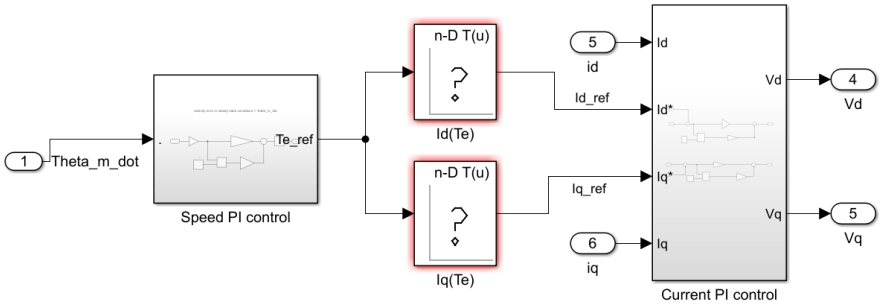

Figure 14 Block diagram of the proposed nested PI controller strategy

The output of the nested PI controller provides the voltage to the electric block of the solver. Therefore, as can be observed, two PI controllers enable increasing the efficiency of the system by regulating the operational feedback of the real-time system condition.

2.4 Coupled Electro-mechanical Dynamic Model

To study the electromechanical coupling vibration response of the electric drive system, the nonlinear model of the motor, the motor control system model, and the gearing system model established in the previous sections are integrated to obtain the electromechanical coupling dynamics. The central purpose of this study is to capture the bidirectional interaction between the electrical and mechanical systems and as shown, the performance of one domain fundamentally influences the other in real-time, which is lost in simplified, uncoupled analyses.

- Closed-Loop Interaction**:** The electromagnetic torque applied to the gears is not a constant value, but a dynamic output constantly adjusted by the control system. This control system relies on instantaneous feedback of the motor's actual speed ($\dot{\Theta}_m = \Omega_m + \dot{\theta}_m$) from the mechanical system.
- Mechanical Feedback: Non-linear gear dynamics (such as time-varying mesh stiffness and backlash) generate torsional vibrations and speed ripple. This speed ripple and torsional vibration act as disturbances that are fed back to the electrical control loops.
- Electrical Reaction: The control system reacts to this mechanical speed ripple by adjusting the voltage commands (V_d, V_q) to the motor, resulting in a corresponding ripple in the electromagnetic torque (T_m). This torque ripple then excites the mechanical system further, closing the loop.

The final model is a unified representation of the following high-fidelity sub-systems:

A. Nonlinear Motor Model

This component models the physical characteristics of the electric machine. It is crucial that it includes non-linear magnetic effects like saturation and accounts for spatial flux harmonics. This model takes the stator current commands from the control system and the actual rotor position and speed from the gearing system, and accurately calculates the electromagnetic torque (T_m) that excites the mechanical system.

B. Motor Control System Model

This sub-model simulates the nested control structure, comprising an outer speed loop and an inner current loop. Its primary function is to interpret the reference speed and react to the actual motor speed feedback ($\dot{\Theta}_m$), and then to generate the precise voltage commands necessary to regulate the motor's output.

C. Gear Transmission System Model

The mechanical transmission, which is established as a non-linear dynamic model incorporating the major sources of vibration: time-varying meshing stiffness and the highly non-linear effect of backlash. This model accepts the electromagnetic torque (T_m) as its primary input excitation and outputs the resultant dynamic variables, including the essential motor speed and rotor angular position, which completes the feedback loop.

The integration results in a comprehensive set of coupled, non-linear ordinary differential equations (ODEs). Solving these equations simultaneously, typically through time-domain numerical integration, allows for the accurate simulation of the full drive cycle.

The significance of this integrated dynamic model is its ability to predict critical NVH phenomena that simpler models overlook:

- Accurate gear whine prediction: It provides high-fidelity data for the dynamic mesh force and dynamic transmission error (DTE).
- Harmonic analysis**:** It accurately links mechanical excitations to electrical ripple, allowing for the study of current and torque harmonics that contribute to motor and inverter noise.
- Stability assessment: It enables the rigorous evaluation of the system's dynamic stability and critical resonance speeds under real-world operating conditions influenced by control system dynamics, electric motor and mechanical nonlinearities.

The modeled electric drive system is a typical complex electromechanical coupling system. In the operation of the electric drive system, the control system and the motor voltage are coupled terms; the motor current and speed are feedback variable inputs to the electrical control system, and the control system is based on the detection of the feedback speed and current signals in real-time control of the motor output torque. The rotational speed and torque are transferred as coupling variables between the permanent magnet synchronous drive motor and the gear train in real time, as shown in Figure 15.

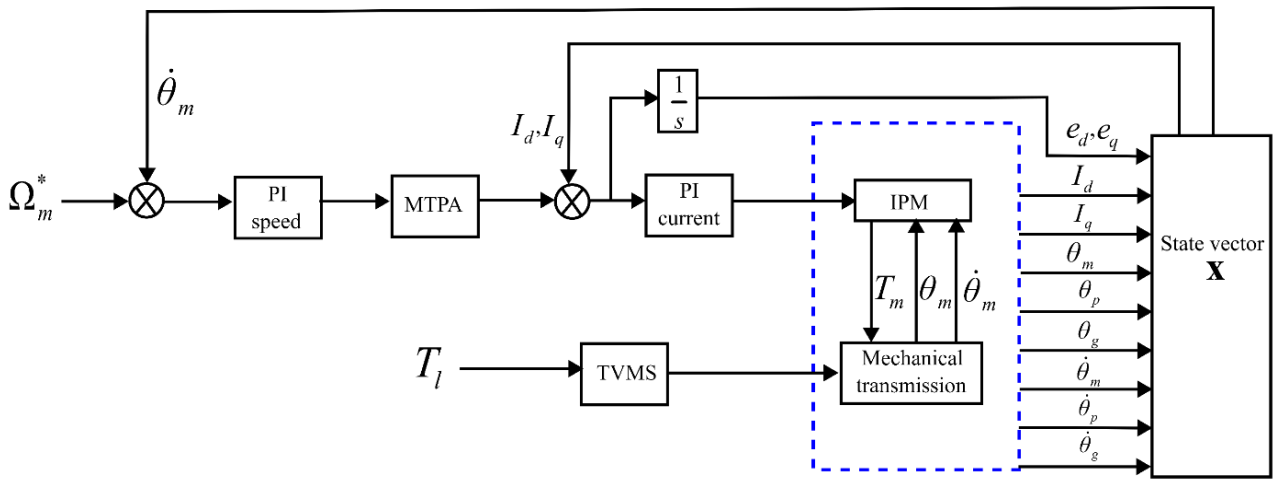

Figure 15: electromechanical coupling dynamic model of the system

By combining Eqs. (1), (2), (4), (7), (12), (15), and expanding the mechanical variables using the state-space formulation, the governing equations of the electric powertrain can be expressed as a comprehensive set of coupled, non-linear ordinary differential equations (ODEs) with time-varying coefficients; It is worth noting that Eq. (12) introduces the terms of integral in the governing set of the equations. To avoid working with integro-differential equations, two additional state variables are introduced as:

$$\begin{aligned} \dot{e_d} &= I_d^*(T_m^*) - I_d \\ \dot{e_q} &= I_q^*(T_m^*) - I_q \end{aligned} \tag{18}$$

The integrated system is defined based on the state variables as follows:

$$\boldsymbol{X} = \left[I_d, I_q, e_d, e_q, \omega_m, \omega_p, \omega_g, \theta_m, \theta_p, \theta_g\right]^T \tag{19}$$

Therefore, the governing set of state-space representation of the system is as follows:

$$\begin{aligned} RI_d + L_{dd}\dot{I}_d + L_{dq}\dot{I}_q + p\dot{\Theta}_m\left(\frac{1}{p}\frac{\partial\lambda_d}{\partial\Theta_m} - \lambda_q\right) &= K_{pI_d}\,\dot{e}_d + K_{iI_d}\,e_d \\ RI_q + L_{qd}\dot{I}_d + L_{qq}\dot{I}_q + p\dot{\Theta}_m\left(\frac{1}{p}\frac{\partial\lambda_q}{\partial\Theta_m} + \lambda_d\right) &= K_{pI_q}\,\dot{e}_q + K_{iI_q}\,e_q \\ \dot{e_d} &= I_d^*(T_m^*) - I_d \\ \dot{e_q} &= I_q^*(T_m^*) - I_q \\ \dot{\theta}_m &= \omega_m \\ \dot{\theta}_p &= \omega_p \\ \dot{\theta}_g &= \omega_g \end{aligned} \tag{20}$$

$$I_m\dot{\omega}_m + c_t^p(\omega_m - \omega_p) + k_t^p(\theta_m - \theta_p) = \frac{3}{2}p(\lambda_d I_q - \lambda_q I_d) + \frac{\partial W_c}{\partial \Theta_m}$$

$$I_p\dot{\omega}_p + r_p c_m\dot{x} + r_p k_m(t)f(x) + k_t^p(\theta_p - \theta_m) + c_t^p(\omega_p - \omega_m) = 0$$

$$I_g\dot{\omega}_g - r_g c_m\dot{x} + r_g k_m(t)f(-x) + c_t^g\dot{\theta}_g + k_t^g\theta_g = -T_l$$

In which, according to the analytical formulation, the reference speed Ω_m and load torque, T_l are assumed as the target variables.

The governing set of equations presenting the coupled dynamics of the electromechanical system is implemented in the MATLAB/Simulink environment. The dynamic system derived from integrating the three non-linear models (motor dynamics, control system, and gear transmission) is classified as a system of Stiff Ordinary Differential Equations (ODEs). Stiffness in this context means that the system contains widely separated time scales. The fast dynamics (small time constants) are governed by the electrical components i.e., current control loops, and high-frequency gear mesh excitation, while the slow are governed by the mechanical components.

Standard explicit numerical solvers like the simple Runge-Kutta methods, would require an extremely small step size to maintain stability and accurately capture the fastest dynamics, making the simulation computationally prohibitive for long-duration analyses.

The choice of the ode23t solver, commonly found in environments like MATLAB/Simulink, is a strategic decision tailored for these types of problems. *ode23t* is an implicit numerical solver that uses a modified version of the Trapezoidal Rule. Implicit methods are stable even with large step sizes, making them highly efficient for stiff systems. It is a medium-order method that strikes a balance between computational speed and accuracy, efficiently handling the mixture of slow mechanical dynamics and fast electrical transients without compromising stability.

The specified relative and absolute tolerances define the acceptable error limits for the numerical solution and are critical for ensuring the fidelity of the simulation results.

- Relative Tolerance: This tolerance governs the error relative to the magnitude of the solution component itself. A value of 10^-6 is a high-precision setting, ensuring that the larger state variables (like angular position or speed) are calculated with high accuracy.

- Absolute Tolerance: This tolerance governs the maximum absolute error allowed in the solution, particularly for components whose values are close to zero (e.g., small vibrations or deviations). A value of 10^-8 is particularly strict. This high degree of precision ensures that small,

critical effects such as the current ripple or the dynamic transmission error (DTE) at low excitation are not lost in numerical noise.

A block diagram of the electromechanical model, presenting all the coupling process and the feedback interactive workflow of the integrated model is represented in Figure 16.

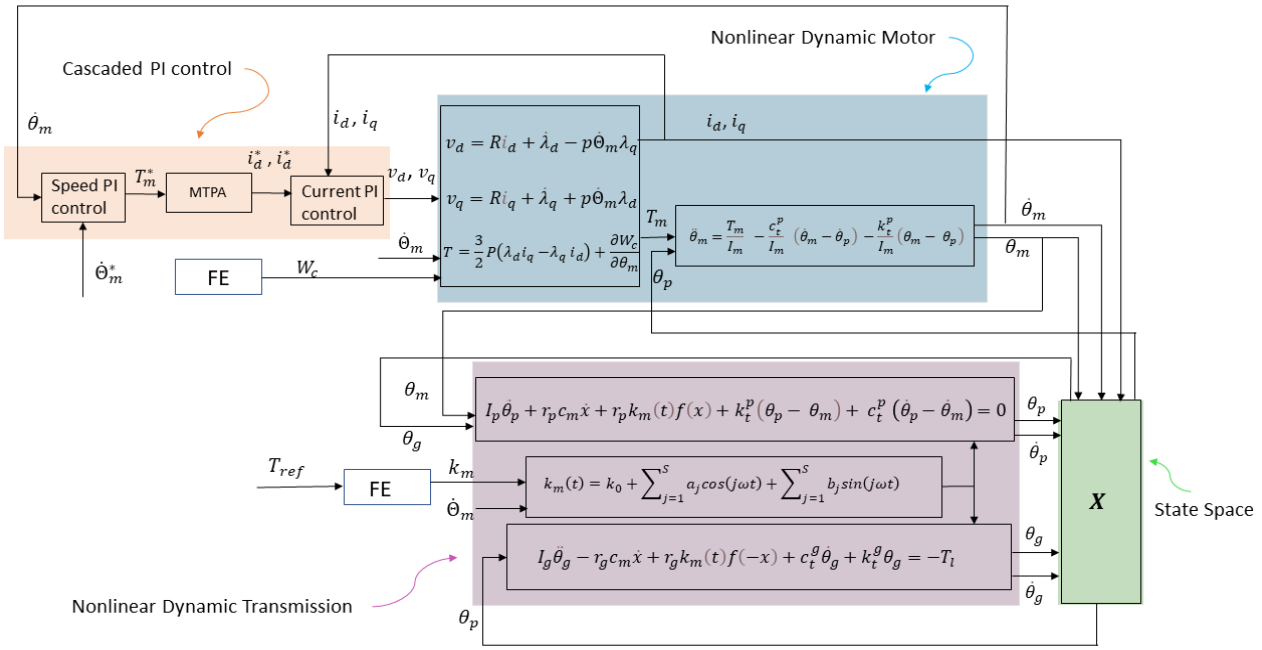

Figure 16 Block scheme of the electromechanical model.

By selecting the appropriate implicit solver and imposing proper tolerances, the study ensures that the computationally demanding simulation of the coupled system yields results that are both stable and enough accurate, thereby providing confidence in the subsequent dynamic analysis. After establishing a complex, high-fidelity numerical model and obtaining a solution through ode23t solver, it is mandatory to perform validation and verification of the solution. This step ensures that the model not only solves the equations correctly and the numerical implementation is correct but also accurately predicts the physical behavior of the electric drive system.

2.5 Frozen time modal analysis

The investigation of linear normal modes plays a fundamental role in supporting the interpretation of the dynamic behavior of nonlinear electromechanical systems. Modal characteristics such as natural frequencies and mode shapes provide valuable insight into the intrinsic vibration mechanisms and serve as a reference for identifying resonance conditions, internal interactions, and potential coupling phenomena within the system. In the context of nonlinear systems, modal analysis is particularly useful for understanding how linearized dynamics influence or interact with nonlinear responses observed under operational excitations.

The governing equations of motion, expressed in Eqs. (20), form a system of coupled differential equations with time-varying coefficients. This time dependency arises primarily from two sources. First, the mechanical subsystem includes parameters such as time-varying mesh stiffness, which introduce periodic variations linked to the gear mesh cycle. Second, the electromagnetic subsystem exhibits strong nonlinear behavior, as the magnetic co-energy and consequently the flux linkages and inductance matrices depend on the instantaneous electrical currents and rotor position. These electromagnetic quantities are evaluated at each time step using multidimensional look-up tables derived from finite element simulations, allowing the effects of magnetic saturation and spatial harmonics to be accurately captured.

As a result, the overall electromechanical system is both strongly nonlinear and time-varying, which makes the direct application of classical linear modal analysis nontrivial. In particular, the continuous variation of system matrices over time prevents the direct formulation of a single, time-invariant eigenvalue problem. This introduces significant challenges in identifying the underlying linear dynamics that govern the system's local vibration behavior.

To address these difficulties, the frozen-time modal analysis method is adopted. In this approach, the system is linearized at selected time instants by "freezing" all time-varying and state-dependent parameters at their instantaneous values. By treating these parameters as constants over an infinitesimally small time-interval, the nonlinear time-varying system is approximated by an equivalent linear time-invariant system at that specific operating point. This allows the formulation and solution of a standard eigenvalue problem, from which the instantaneous natural frequencies and corresponding mode shapes can be extracted.

The frozen-time modal analysis provides valuable information about the modes that may participate in electromechanical coupling phenomena, particularly those associated with interactions between the motor electromagnetic dynamics and the torsional vibrations of the drivetrain. By performing this

analysis at different time instants or operating conditions, the evolution of modal characteristics can be examined, offering insight into how variations in electromagnetic torque, gear mesh stiffness, and operating speed influence the system's dynamic behavior.

Accordingly, Eqs. (20) can be rearranged and expressed in the matrix form given in Eq. (21) [102,103], which represents the linearized electromechanical system with frozen parameters. This formulation establishes the basis for computing the eigenvalues and eigenvectors required for modal analysis and serves as a key step in interpreting the dynamic responses observed in subsequent nonlinear simulations.

$$\mathrm{A}\dot{\mathrm{x}} + \mathrm{Bx} = \mathrm{u} \tag{21}$$

Where;

$$\mathbf{A} = \begin{pmatrix} \tilde{L}_{dd} & \tilde{L}_{dq} & -K_{pI_d} & 0 & 0 & 0 & 0 & 0 & 0 & 0 \\ \tilde{L}_{qd} & \tilde{L}_{qq} & 0 & -K_{pI_q} & 0 & 0 & 0 & 0 & 0 & 0 \\ 0 & 0 & 1 & 0 & 0 & 0 & 0 & 0 & 0 & 0 \\ 0 & 0 & 0 & 1 & 0 & 0 & 0 & 0 & 0 & 0 \\ 0 & 0 & 0 & 0 & 1 & 0 & 0 & 0 & 0 & 0 \\ 0 & 0 & 0 & 0 & 0 & 1 & 0 & 0 & 0 & 0 \\ 0 & 0 & 0 & 0 & 0 & 0 & 1 & 0 & 0 & 0 \\ 0 & 0 & 0 & 0 & 0 & 0 & 0 & I_m & 0 & 0 \\ 0 & 0 & 0 & 0 & 0 & 0 & 0 & 0 & I_p & 0 \\ 0 & 0 & 0 & 0 & 0 & 0 & 0 & 0 & 0 & I_G \end{pmatrix} \tag{22}$$

B=

$$\begin{pmatrix} R & 0 & -K_{il_d} & 0 & 0 & 0 & 0 & p\left(\frac{1}{p}\frac{\partial\tilde{\lambda}_d}{\partial\Theta_m} - \tilde{\lambda}_q\right) & 0 & 0 \\ 0 & R & 0 & -K_{il_q} & 0 & 0 & 0 & p\left(\frac{1}{p}\frac{\partial\tilde{\lambda}_q}{\partial\Theta_m} + \tilde{\lambda}_d\right) & 0 & 0 \\ 1 & 0 & 0 & 0 & 0 & 0 & 0 & 0 & 0 & 0 \\ 0 & 1 & 0 & 0 & 0 & 0 & 0 & 0 & 0 & 0 \\ 0 & 0 & 0 & 0 & 0 & 0 & 0 & -1 & 0 & 0 \\ 0 & 0 & 0 & 0 & 0 & 0 & 0 & 0 & -1 & 0 \\ 0 & 0 & 0 & 0 & 0 & 0 & 0 & 0 & 0 & -1 \\ \frac{3p\tilde{\lambda}_q}{2} & -\frac{3p\tilde{\lambda}_d}{2} & 0 & 0 & k_t^p & -k_t^p & 0 & c_t & -c_t & 0 \\ 0 & 0 & 0 & 0 & -k_t^p & k_t^p + k_m r_p^2 & -k_m r_g r_p & -c_t & c_t + c_m r_p^2 & -c_m r_g r_p \\ 0 & 0 & 0 & 0 & 0 & -k_m r_g r_p & k_t^g + k_m r_g^2 & 0 & -c_m r_g r_p & c_t + c_m r_g^2 \end{pmatrix} \tag{23}$$

$$\mathbf{u} = \begin{pmatrix} -p\Omega_m\left(\frac{1}{p}\frac{\partial\tilde{\lambda}_d}{\partial\Theta_m} - \tilde{\lambda}_q\right) \\ -p\Omega_m\left(\frac{1}{p}\frac{\partial\tilde{\lambda}_q}{\partial\Theta_m} + \tilde{\lambda}_d\right) \\ I_d^* \\ I_q^* \\ 0 \\ 0 \\ 0 \\ \dfrac{\partial\widetilde{W}_c}{\partial\Theta_m} \\ bk_m r_p \\ -bk_m r_g - T_l \end{pmatrix} \qquad \mathbf{x} = \begin{pmatrix} I_d \\ I_q \\ e_d \\ e_q \\ \theta_m \\ \theta_p \\ \theta_g \\ \omega_m \\ \omega_p \\ \omega_g \end{pmatrix} \tag{24}$$

with the operator $\widetilde{(\cdot)}$ highlighting the coefficients evaluated at the operating point fixed in a specific time instant.

The coefficient matrix $-\mathbf{A^{-1}B}$ contains the essential information required for the formulation and solution of the eigenvalue problem associated with the linearized electromechanical system. The eigenvalues of this matrix correspond to the system's natural frequencies and modal damping characteristics, while the associated eigenvectors describe the spatial distribution of the corresponding vibration modes. As such, this matrix plays a central role in identifying the dynamic characteristics that govern the system's response.

Unlike classical undamped or proportionally damped mechanical systems, the matrix $-\mathbf{A^{-1}B}$ is generally non-symmetric due to the presence of electromechanical coupling terms and control-induced asymmetries. Consequently, the eigenvalue problem does not admit a single set of orthogonal eigenvectors. Instead, two distinct sets of eigenvectors must be considered: the right eigenvectors, which describe the modal response of the system, and the left eigenvectors, which are associated with the adjoint system.

These left and right eigenvectors are related through the biorthogonality property, meaning that each left eigenvector is orthogonal to all right eigenvectors except for the one associated with the same eigenvalue. This biorthogonal relationship provides a consistent mathematical framework for modal decomposition and enables the projection of the system's dynamic response onto a modal subspace, even in the presence of non-symmetric system matrices. The use of biorthogonal eigenvectors is therefore essential for accurately analyzing and interpreting the electromechanically coupled vibration modes of the system [104].

2.6 Bifurcation analysis: initial conditions and PI controllers' settings

Bifurcation analysis is capable of revealing the full dynamic scenario of the system, showing how different periodic, quasi-periodic, or chaotic solutions emerge and evolve as a function of shaft speed, providing a more comprehensive understanding of the nonlinear phenomena inherent in gear dynamics. The main objective of this study is the dynamic simulation of the fully integrated electromechanical system including the electric motor, PI controllers, gear transmission, and the compliance shafts. Therefore, the analysis aims to identify changes in the qualitative behavior of the system response, such as the onset of multiple steady-state solutions, jump phenomena, or transitions to non-periodic motion, as commonly described in nonlinear dynamic [105].

In this study, bifurcation analysis has been carried out using the rotor speed Ω_m as the bifurcation parameter. The speed was varied in the speed range $\Omega_m \in [\Omega_{m,min}, \Omega_{m,max}]$, with an incremental step $\Delta\Omega_m$, in both speed-up and speed-down directions. At each speed step, N_Ω mesh periods were simulated, and N_s samples were recorded per meshing period. To eliminate transients, the steady-state response was evaluated considering only the last $N_{\Omega,s}$ meshing period.

In this context, the definition of the initial state vector $\mathbf{x_0}$ plays a pivotal role in solving the differential problem and initializes the numerical solution in the bifurcation analysis. Indeed, the numerous and complex nonlinearities of the system may converge to different co-existing attractors. To this end, for the first speed step, the initial state vector was defined as in (25),

$$\mathbf{x_0} = \left[I_{d,0}^*, I_{q,0}^*, \frac{RI_{d,0}^*}{K_{iI_d}}, \frac{RI_{q,0}^*}{K_{iI_q}}, 0,0,0,0,0,0 \right]^T \tag{25}$$

where;

$$T_{m,0}^* = T_l \frac{r_p}{r_g}, \qquad I_{d,0}^* = I_d^*(T_{m,0}^*) \qquad I_{q,0}^* = I_q^*(T_{m,0}^*) \tag{26}$$

Particular attention must be devoted to the third and fourth components of $\mathbf{x_0}$, which were derived from the third and fourth of Eqs. (20) by assuming null time derivatives and by introducing a fictious speed ramp used to increase Ω_m smoothly from 0 to $\Omega_{m,min}$for speed up simulation and from $\Omega_{m,max} + \Delta\Omega_m$ to $\Omega_{m,max}$ for speed-down simulation. More generally, at every speed step (not only the first), the fictitious ramp is required to ensure the continuity of the trajectory during the bifurcation analysis. In fact, at the end of the *i*-th step and the beginning of the (*i*+1)-th step, the following relations hold:

$$\dot{\Theta}_m^i(t_{end}) = \Omega_m^i + \dot{\theta}_m^i(t_{end}) \tag{27}$$

$$\dot{\Theta}_m^{i+1}(0) = \Omega_m^{i+1} + \dot{\theta}_m^{i+1}(0)$$

To preserve the continuity condition, one should hold $\dot{\Theta}_m^{i+1}(0) = \dot{\Theta}_m^i(t_{end})$. Without introducing this condition, there would be an inconsistency, since the instantaneous change in reference speed generates a constant error term $\Omega_m^{i+1} - \Omega_m^i$, which represents an unphysical jump in the nominal speed between consecutive steps. The only way to eliminate this discontinuity and thus avoid a spurious constant error in the formulation, is to introduce a fictitious speed ramp that smoothly connects Ω_m^i and Ω_m^{i+1}, preserves the continuity of the electromagnetic torque T_m, and prevents divergence of the numerical integrator. To maintain the continuity condition during the frequency response analysis, between frequency steps, the following initial conditions on torque control must be applied:

If;

$$\begin{aligned} \dot{\Theta}_m^* &= \Omega_m \\ \dot{\Theta}_m &= \Omega_m + \dot{\theta}_m \end{aligned} \tag{28}$$

Then;

$$\begin{aligned} \dot{e}_\Omega &= \dot{\Theta}_m^* - \dot{\Theta}_m = -\dot{\theta}_m \\ e_\Omega(t) &= \int \dot{e}_\Omega(t)dt = -\theta_m + C \end{aligned} \tag{29}$$

Therefore, from:

$$T_m^*(0) = K_{p\Omega}\, \dot{e}_\Omega(0) + K_{i\Omega}\, e_\Omega(0) \tag{30}$$

eventually, we have;

$$e_\Omega(0) = \frac{T_m^*(0) - K_{p\Omega}\, \dot{e}_\Omega(0)}{K_{i\Omega}} = \frac{T_m^*(0) + K_{p\Omega}\, \dot{\theta}_m(0)}{K_{i\Omega}} \tag{31}$$

where, $T_m^*(0)$ and $\dot{e}_\omega(0)$ are determined from the previous frequency step's state.

On the other hand, currents $I_d^*(T_m^*), I_q^*(T_m^*)$ are nonlinear functions of the reference torque as follows:

$$\begin{aligned} I_d^*(T_m^*) &= I_d^*(T_{m0}^*) + \frac{dI_d^*}{dx}|_{T_{m0}^*}(T_m^* - T_{m0}^*) + \cdots \\ I_q^*(T_m^*) &= I_q^*(T_{m0}^*) + \frac{dI_q^*}{dx}|_{T_{m0}^*}(T_m^* - T_{m0}^*) + \cdots \end{aligned} \tag{32}$$

By considering just the first order expansion of the currents one can observe:

$$\dot{e_d} = I_d^*(T_{m0}^*) + \frac{dI_d^*}{dx}|_{T_{m0}^*}(T_m^* - T_{m0}^*) - I_d \tag{33}$$

$$\dot{e_q} = I_q^*(T_{m0}^*) + \frac{dI_q^*}{dx}|_{T_{m0}^*}(T_m^* - T_{m0}^*) - I_q \tag{34}$$

Applying (33) and (34) allows to define the initial condition in speed-up simulation for the current error, in the first excitation frequency step, while initial currents are derived from (25). For the mechanical state variables, the first step is initialized from static situation, and the sequential steps start from the last condition of the previous step, keeping the continuity of the dynamic simulation.

Chapter 3: Results and Discussion

3.1 Inputs and Pre-requisites

To evaluate the proposed electromechanical coupling model and to illustrate its capability in capturing the dynamic behavior of the electric drive system, a representative test case is defined using the geometrical, material, and operational parameters summarized in Table 3. These parameters describe the configuration of the electric machine, the transmission components, and the associated mechanical properties, and are selected to reflect realistic conditions encountered in automotive electric drive units.

The gear set considered in this study has previously been analyzed in Ref. [101] using a simplified single-degree-of-freedom (1-DOF) torsional model, where the torsional flexibility of the shafts was neglected, and the system dynamics were primarily governed by the gear mesh stiffness and external excitation. Despite its simplicity, the 1-DOF model provided valuable baseline results for understanding the fundamental vibration characteristics of the gear pair. However, such a reduced-order representation is inherently limited in its ability to capture distributed torsional effects, modal interactions. Moreover, electromechanical coupling phenomena that arise in more realistic configurations can be captured in a model in which the torsional stiffness of the compliance shafts are included.

By contrast, the present model extends this earlier formulation by incorporating the torsional flexibility of the drive shafts, nonlinear gear mesh characteristics, and the dynamic interaction with the electric motor and its control system. This enhanced modeling framework allows for a more detailed representation of the transmission dynamics and enables the investigation of coupling effects between the mechanical and electromagnetic subsystems. The comparison with the results reported in Ref. [101] therefore serves a dual purpose: first, it provides a means to validate the proposed model by ensuring consistency with established results under simplified conditions; and second, it highlights the additional dynamic features that emerge when shaft flexibility and electromechanical interactions are taken into account.

The results presented in the following subsections demonstrate how the inclusion of these effects influences the system's modal properties, frequency response characteristics, and nonlinear vibration behavior.

Table 3: The gear pair's characteristics

Data	**Pinion**	**Gear**
Number of teeth	28	43
Module [mm]	3	3
Pressure angle [Deg]	20	20

Base radius [mm]	39.467	60.610
Theoretical pitch radius [mm]	42	64.5
Thickness on theoretical pitch circle [mm]	6.1151	6.7128
Addendum modification [mm]	1.927	2.748
Face width [mm]	27	22.5
Hob tip radius [mm]	0.9	0.9
Outer diameter [mm]	93.1	139.7
Root diameter [mm]	79.1	126.2
Inner diameter [mm]	40	40
Mass [kg]	0.71681	1.9823
Inertia [kg m2]	0.0008076	0.0047762
Young's modulus [MPa]	206000	206000
Poisson's coefficient	0.3	0.3
Center distance [mm]	111	
Backlash (2b) on the line of action [mm]	0.312	
Contact ratio	1.28565	
Profile modification	None	

The first stage is to model the gear pair's geometrical and material characteristics reported in Table 3, to reconstruct the TVMS of the gear pair through FE simulations conducted with Transmission 3D software [99]. The reconstruction procedure begins with the evaluation of the static transmission error (STE), which represents the relative angular displacement between the driving and driven gears under quasi-static loading conditions. The STE is computed at discrete angular positions over a complete mesh cycle, capturing the influence of tooth engagement and disengagement as well as the transition between single- and double-tooth contact. In this simulation, the mesh cycle is discretized into 15 evenly spaced angular positions, providing a sufficiently fine resolution to describe the periodic variation of the gear mesh stiffness while maintaining computational efficiency.

From the computed STE values, the mesh stiffness is derived as a function of the mesh position by relating the applied torque to the resulting elastic deflection. This procedure yields a discrete set of stiffness values that describe the temporal evolution of the TVMS over one mesh period. Since gear meshing is inherently periodic, the resulting TVMS exhibits periodicity with respect to the mesh frequency.

To obtain a continuous analytical representation suitable for dynamic simulations, the discrete stiffness data obtained from the FE-based STE analysis are transformed into the frequency domain using a discrete Fourier transform (DFT). The dominant harmonic components extracted from the DFT are then used to construct a Fourier series expansion of the TVMS, allowing the stiffness

variation to be expressed as a smooth, continuous, and periodic function of time. This formulation facilitates the incorporation of the TVMS into the nonlinear dynamic model of the transmission.

The simulation to extract and evaluate the static transmission error (STE) is performed in different driving torque level to investigate the effect of the applied torque on the dynamic response of the system.

(a) (b) (c)

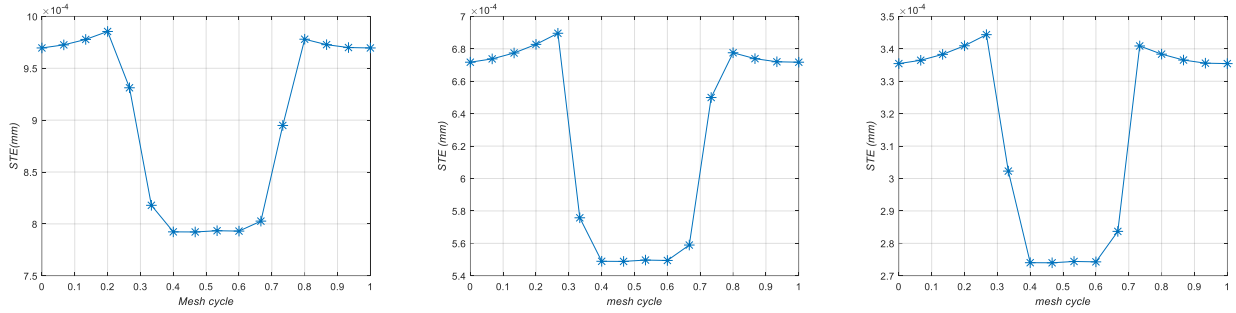

Figure 17 Static Transmission Error, (a): Applied torque=470 Nm, (b): Applied torque=325 Nm, (c): Applied torque=163 Nm

Figure 18 illustrates the variation of the mesh stiffness derived from the static FE analysis for the considered gear pair under three distinct driving torque levels. The results highlight the influence of the applied load on the magnitude and shape of the stiffness fluctuation, reflecting the nonlinear contact behavior of the gear teeth. As the driving torque increases, changes in contact conditions and load sharing between teeth lead to noticeable variations in both the mean stiffness value and the amplitude of its periodic modulation, which are expected to significantly affect the dynamic response of the electric drive system.

(a) (b) (c)

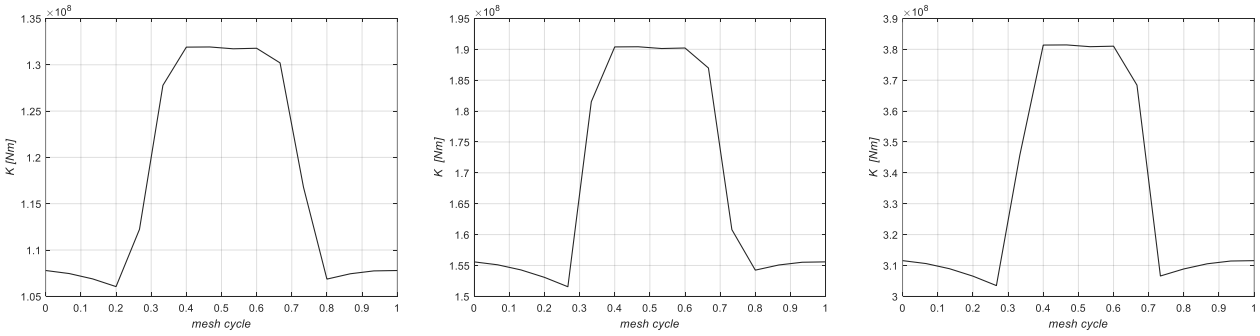

Figure 18 Mesh stiffness variation, (a): Applied torque=470 Nm, (b): Applied torque=325 Nm, (c): Applied torque=163 Nm

Table 4 lists the mean value of the mesh stiffness provided by the Fourier series, assuming seven harmonics, and details on the data are provided in Appendix A.

Table 4 Mean mesh stiffness under different static torques

Applied Torque (Nm)	Mean mesh stiffness (N/m)
470	3.3939 E+08
325	3.3665 E+08
163	3.3449 E+08

Figure 19 represents a comparison on the variation of the mesh stiffness with different torque levels.

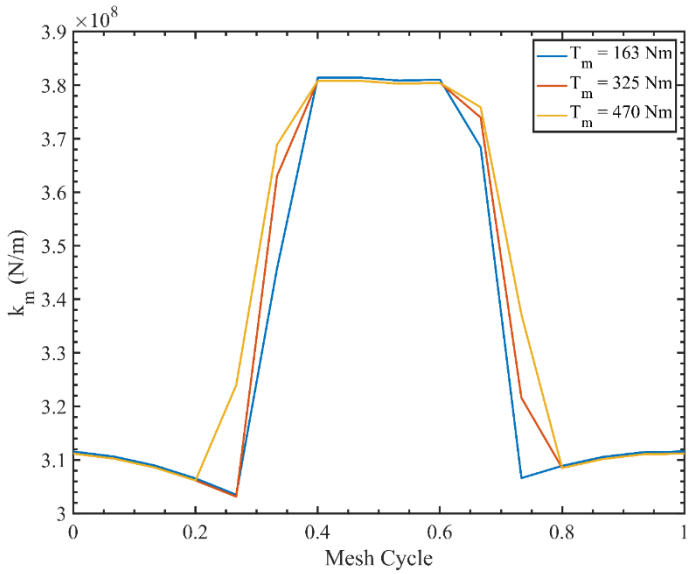

Figure 19 Time-varying mesh stiffness at three torque levels

The lumped-mass model of the transmission also accounts for shaft torsional deflection. The geometrical parameters and material properties of the shafts, provided in Table 5, are used to determine the torsional stiffness k_t^i of the i-th shaft using the pure torsional relation $k_t^i = \frac{GJ_i}{L_i}$, where G is the shear modulus, J_i is the polar moment of inertia, and L_i is the shaft length.

Following the approach presented in Refs. [106, 107], to retain the torsional damping c_t of both pinion and gear shafts, the following formula has been used,

$$c_t = 2\zeta_t \sqrt{\frac{k_t^p}{\left(\frac{1}{I_m} + \frac{1}{I_p}\right)}} \tag{35}$$

Where, ζ_t is the shaft's damping ratio.

The shaft inertias are also considered in the model. To incorporate them, each shaft's inertia is distributed equally among the three wheels of the system: the input shaft's inertia is divided between the motor and pinion wheels, while the output shaft's inertia is divided between the gear and the load wheel.

Table 5 Connecting shafts' characteristics

	Input shaft	Output shaft
Length [m]	0.2	0.515
Inner diameter [mm]	20	20
Outer diameter [mm]	40	40
Young's modulus [MPa]	206000	206000
Shear modulus [MPa]	70000	70000
Inertia [kg m2]	3.676E-04	9.4731E-04

The nonlinear electric motor is modeled based on the method described in Section 3.2.1. The motor considered for this study is a heavy-duty IPMSM for traction applications. The complementary details of the motor and PI controllers' characteristics are provided in Table 6. An example of the magnetic co-energy $W_c(i_d, i_q, \Theta_m)$, retrieved from Altair data multivariate interpolation, is shown in Figure 20 for $\Theta_m = 0$ rad.

Table 6 Electric motor and PI controllers' characteristics

Motor's parameters		Unit
Number of poles	12	-
Number of slots	72	-
Stator phase resistance R_s	0.02	Ω
Nominal DC-Link voltage V	650	V
Rated Current i_{max}	600	A
Rated Torque T_{max}	729	Nm
Rated Power	300	kW
D-axis inductance, unsaturated L_d	0.156	mH
Q-axis inductance, unsaturated L_q	0.308	mH
Magnet flux linkage, unsaturated λ_m	0.129	Wb
Speed controller cut-off frequency	100	Hz
Torque controller cut-off frequency	1000	Hz

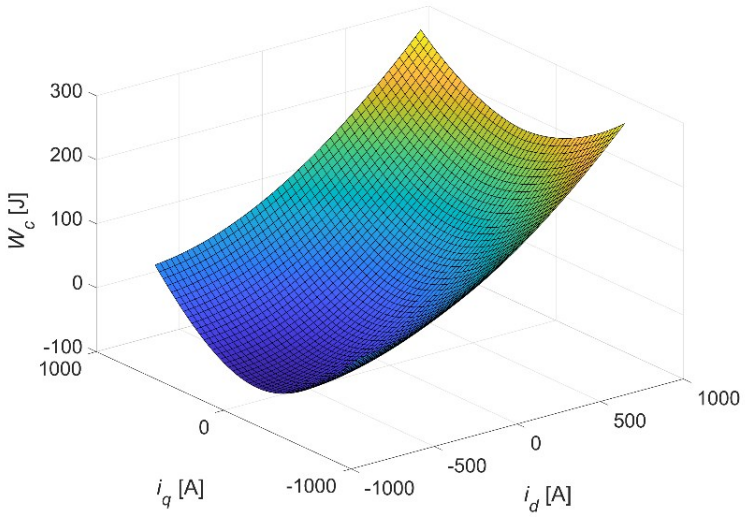

Figure 20. Interpolated IPMSM magnetic co-energy for $\Theta_m = 0$ rad

3.2 Validation of the Numerical Solver

The accuracy of the numerical solver is verified in two stages; First the tortional vibration model of the gear pair in the absence of the electromagnetic effects is considered in comparison with the experimental analysis of DTE response of a gear set [97], which serves as the basis validation source in many researches of the gear dynamics. In order to address this, the gear pair geometrical and material parameters are selected as is reported in the aforementioned study and the bifurcation simulation is applied to retain the DTE response in the speed range of interest. The validation typically involves comparing key dynamic metrics i.e., Dynamic Transmission Error, as the primary indicator of gear whine with the benchmark for mechanical vibration across a range of operating speeds. The close agreement with the experimental results as can be observed in Figure 21 highlights the model's effectiveness in predicting DTE response of the gear pair.

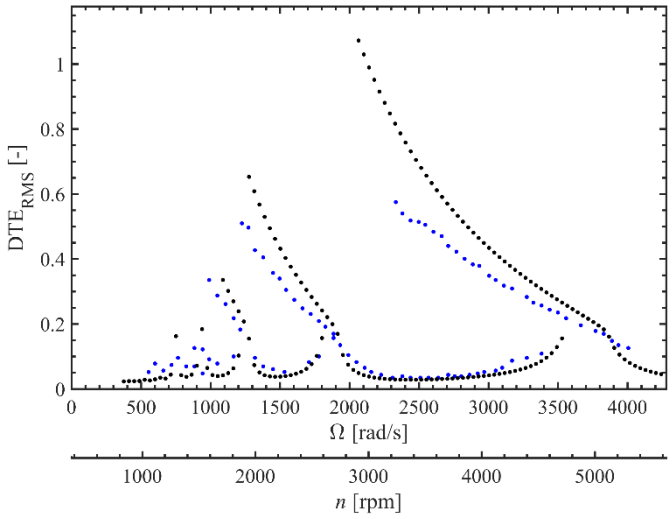

Figure 21 Nondimensional DTE amplitude-frequency diagram comparison: present model (black), and experimental data [43].

The comparison against the results published in reference [101] serves as the secondary check of the accuracy of the numerical solver**.** Reference [101] details a numerical study on the dynamic and stability analysis of spur gear pair that is validated base on the experimental data of [97]. In order to investigate the accuracy of the model, the amplitude-frequency diagram on the case study is compared with Ref. [101], which simulated the system utilizing a one-DOF torsional model. The geometrical and physical characteristics of the evaluation case are as reported in Table 3 and, in order to decouple the motion of motor and load from meshing gears, a shaft stiffness $k_t^p = k_t^g = 180\ Nm/\text{rad}$ is considered for the 3-DOF model.

Moreover, the system stability predicted by the model is compared against those observed in [101]. Figure 22 Nondimensional DTE, amplitude-frequency diagram comparison: 1-DOF model [38] (black), and 3-DOF model (blue).shows the comparison results indicating that the 3-DOF model

successfully converges to the 1-DOF model: the former exhibits the mesh mode at $\omega_n = 30272\ rad/s$, which approaches the natural frequency of the latter, $\omega_n = 31560\ rad/s$, with the 3-DOF model showing lower oscillation amplitude due to the presence of shaft compliances

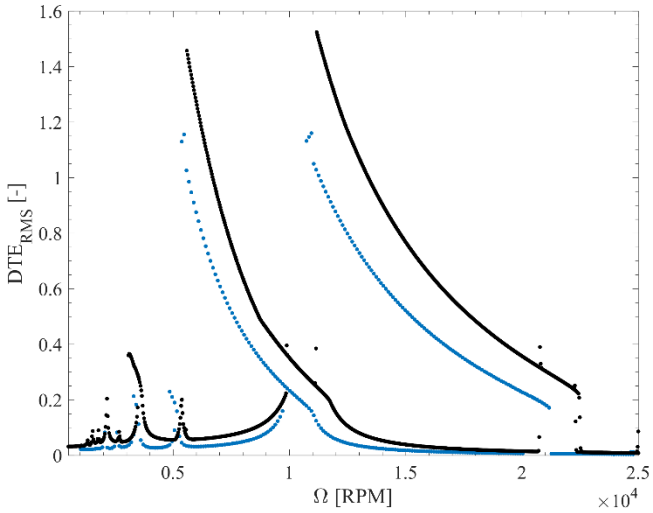

Figure 22 Nondimensional DTE, amplitude-frequency diagram comparison: 1-DOF model [38] (black), and 3-DOF model (blue).

A positive comparison confirms the model's ability to serve as a reliable predictive tool for subsequent analyses, such as exploring spectrogram plots and bifurcation diagrams which are the necessary groundwork for optimizing the NVH performance of future electric driveline designs.

3.3 Linear Normal Modes of the Electromechanical System

To rigorously evaluate the electromechanical interactions within the powertrain, a baseline is first established through modal analysis of the decoupled mechanical subsystem. By isolating the mechanical components from electromagnetic excitations and control feedback loops, the intrinsic dynamic characteristics of the driveline, governed solely by the structural parameters listed in Tables 3, 4, and 6 can be quantified. For this analysis, the gear mesh stiffness is assumed to be equal to its mean value in order to examine the system modes under linearized conditions.

The eigenvalue solution reveals three distinct stable modes within the frequency range of interest as can be observed in Figure 23. These modes represent the natural oscillatory behavior of the mechanical assembly and provide a reference for assessing the potential interaction between electromagnetic excitations and the structural dynamics in the coupled system.

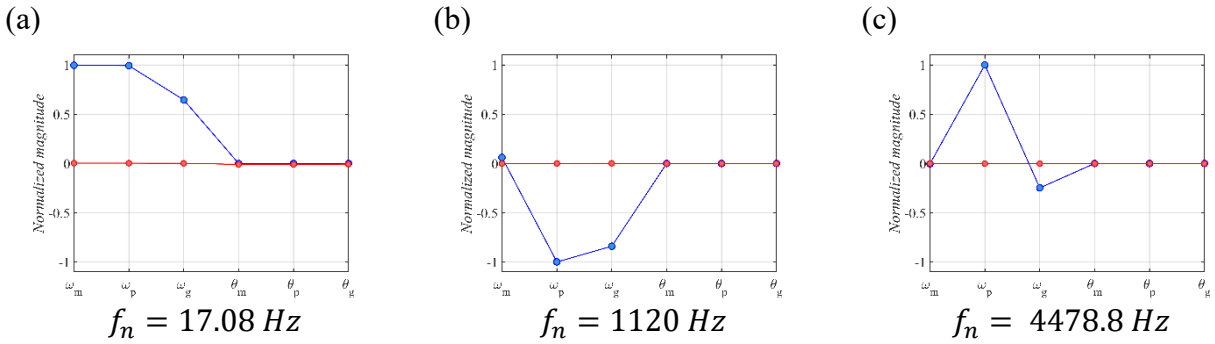

Figure 23. Linear normal modes of the purely mechanical 3-DOF model. Real value (blue), Imaginary value (red).

The modal analysis of the driveline reveals the presence of three stable natural modes, each corresponding to a distinct dynamic behavior of the system components.

The first mode occurs at 17.08 Hz and represents a quasi-rigid body in-phase rotational mode of the drivetrain. In this mode, all rotating inertias including the motor rotor, and gear disks oscillate in phase, as illustrated in Figure 23(a). This low-frequency behavior is primarily governed by the overall system inertia and the equivalent torsional stiffness of the shafts. Such a mode, is typically sensitive to load disturbances and low-frequency torque variations, and it plays a significant role in driveline low-frequency vibration phenomena

The second mode appears at 1120 Hz and is mainly characterized by the in-phase motion of the pinion and gear pair, while the motor exhibits a comparatively small out-of-phase contribution, as shown in Figure 23(b). The dominant participation of the gears indicates that this mode is influenced by the local stiffness distribution around the gear stage, while the limited motor participation suggests partial dynamic decoupling at this frequency range.

The third and highest-frequency mode is located at 4478.8 Hz and corresponds to the gear mesh mode. In this case, the dynamic motion is confined entirely to the pinion and gear wheels, which oscillate out of phase with respect to each other, as depicted in Figure 23(c). This behavior is characteristic of a local mesh deformation mode, where the relative motion across the gear contact is governed by the mesh stiffness. Due to its high frequency and localized nature, this mode is particularly relevant for high-frequency vibration and noise generation, and it is highly susceptible to excitation from mesh stiffness variation and electromagnetic torque harmonics near the mesh frequency.

Subsequently, by implementing a frozen-time modal analysis; a quasi-static linearization of the coupled electromechanical system as detailed in Section 3.2, enables us to rigorously quantify the modal interactions and the resultant deviations in the system's eigen properties. This methodology facilitates a high-fidelity characterization of how electromagnetic parameters influence the fundamental mechanical modes, providing a definitive analytical framework for evaluating the nonlinear coupling effects inherent in the integrated powertrain.

The inclusion of electromagnetic coupling and closed-loop control introduces non-conservative and control-induced interaction terms, which generally render the system matrices non-symmetric. As a result, the associated eigenvalue problem becomes non-self-adjoint. In such cases, a complete modal description requires the computation of both right and left eigenvectors.

The right eigenvectors represent the system state modes, describing the state evolution associated with each eigenvalue. The left eigenvectors, on the other hand, provide the corresponding adjoint modes and quantify the modal sensitivity or participation of the system states and inputs. Together, the right and left eigenvectors satisfy biorthogonality conditions, which are essential for modal projection and for achieving a decoupled representation of the system dynamics in the state-space framework.

Figure 24 presents the right eigenvectors of the electromechanical model, obtained under the frozen time assumption discussed in Section 1.3, with details about the coefficient matrices provided in Appendix B.

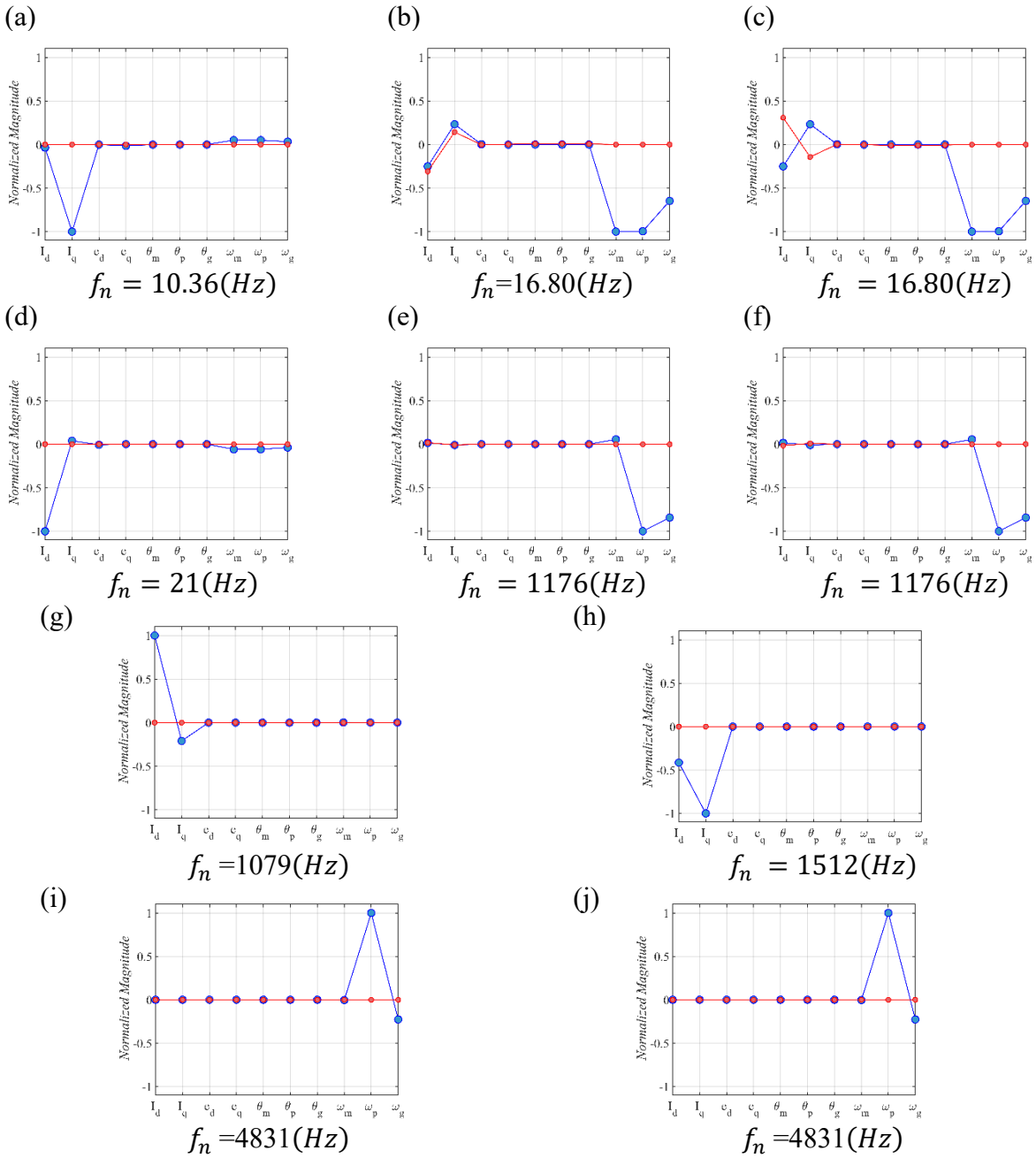

Figure 24. Linear normal modes of the coupled electro-mechanical model. Real value (blue), Imaginary value (red).

The comparative data presented in Table 5 illustrates the profound influence of electromagnetic coupling on the system's linear modes composition. By expanding the state-space vector to include electrical variables the system's dimensionality increases, giving rise to supplemental poles that characterize the electromechanical interaction.

Table 7. Comparison of the normal modes in the presence and absence of electromagnetic effects

Mode		Purely mechanical model			Electromechanical model	
n	characteristic	$f_n\ (Hz)$	ζ_n	characteristic	$f_n\ (Hz)$	ζ_n
1	-	-		electrical	10.36	-
2-3	torsional	17.08	0.020	coupled	16.80	0.03
4	-	-		coupled	21	-
5-6	torsional	1120	0.002	torsional	1176	0.002

7	-	-		electrical	1079	-
8	-	-		electrical	1512	-
9-10	torsional	4478.8	0.012	torsional	4831	0.01

The electromechanical formulation introduces four real eigenvalues (n=1, 4, 7, 8) that are absent in the decoupled mechanical model. These modes are predominantly governed by the electrical time constants of the motor. Specifically:

Mode 1 and 4 (10.36 Hz and 21 Hz): Represents the slow-acting electrical poles, with a negligible contribution of the mechanical subsystem

Mode 2 and 3 (16.80 Hz): the mode shapes show significant participation from both the mechanical speeds ($\omega_m, \omega_p, \omega_g$) and the electrical currents (I_d, I_q).

Modes 7 and 8: High-frequency electrical poles (1079 Hz and 1512 Hz) that represent the rapid electromagnetic transients. These real poles indicate non-oscillatory, over-damped decay characteristics inherent to the electrical subsystem.

The six complex conjugate pairs (n=2,3, 5,6, 9,10) correspond to the fundamental torsional oscillations of the driveline. While these modes are rooted in the mechanical physics of the system, their "coupled" nature in the new model suggests that the electromagnetic field acts as a frequency-dependent stiffness and damping element solely at n=2,3 (16.80 Hz).

A critical observation is the 7.8% increase in the gear-mesh natural frequency (Modes 9-10), rising from the purely mechanical baseline to 4831 Hz.

To investigate the stability characteristics of the system across operating conditions, the eigenvalue locus as a function of rotational speed is presented in Figure 25. The operational speed is selected based on the working speed range of IPM motor and at each speed step the frozen time approach is utilized to evaluate the eigenmodes of the coupled system. The horizontal axis represents the real part of the eigenvalues, which indicates the modal damping and stability, while the vertical axis shows the imaginary part, corresponding to the modal frequency (expressed in Hz). Each colored marker denotes an eigenvalue at a specific operating speed. The figure illustrates how the system modes evolve with speed and allows the identification of changes in damping and potential instability regions. As shown in the figure, all eigenvalues remain located in the left half of the complex plane, and none cross the line defined by Re(λ) = 0. This indicates that the system is stable over the investigated speed range, since eigenvalues with negative real parts correspond to decaying (stable) modes, whereas eigenvalues with positive real parts would indicate dynamic instability.

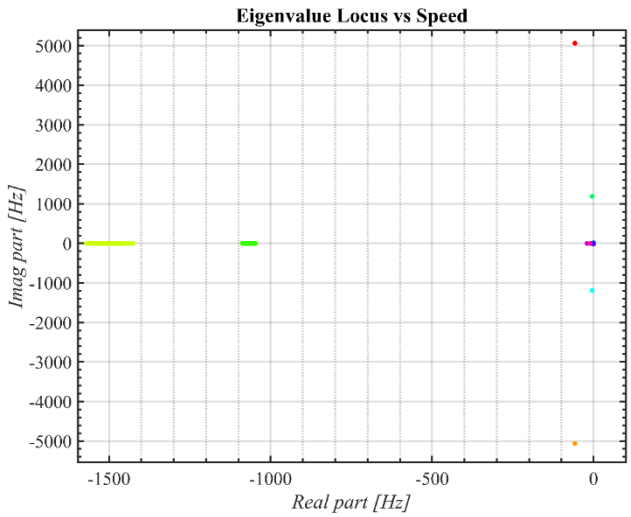

Figure 25. Eigenvalue's locus of the coupled system by varying the excitation frequency

Because the eigenvalues are distributed over a wide range, their variations are not clearly visible in the full-scale representation. Therefore, Figure 26 provides a zoomed view of Figure 25 where the locus of each mode is presented separately to better illustrate the evolution of the eigenvalues with operating speed. Although the modal frequencies and damping characteristics vary with speed, all eigenvalues remain confined to the left half plane.

(a)

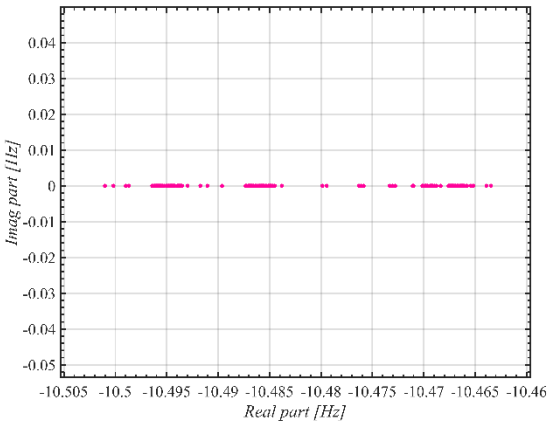

(b)

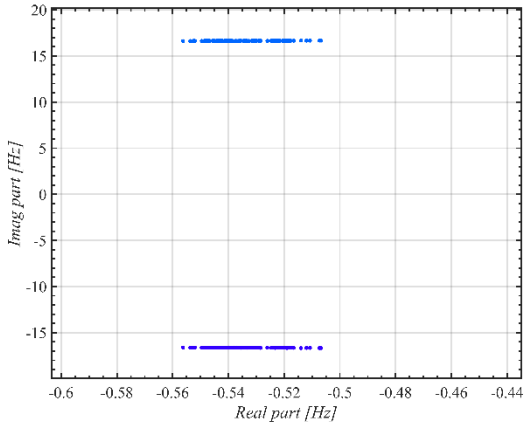

(c)

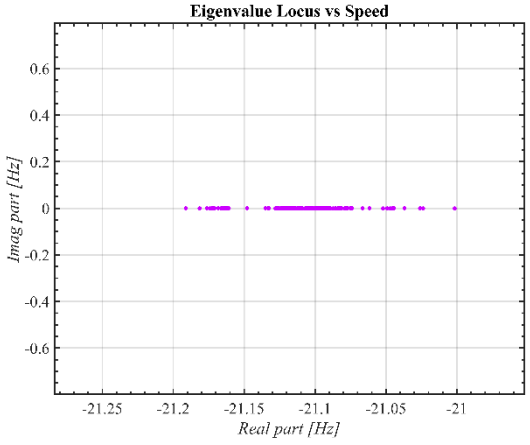

(d)

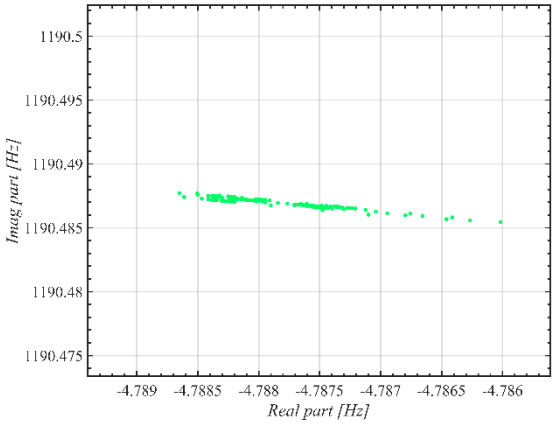

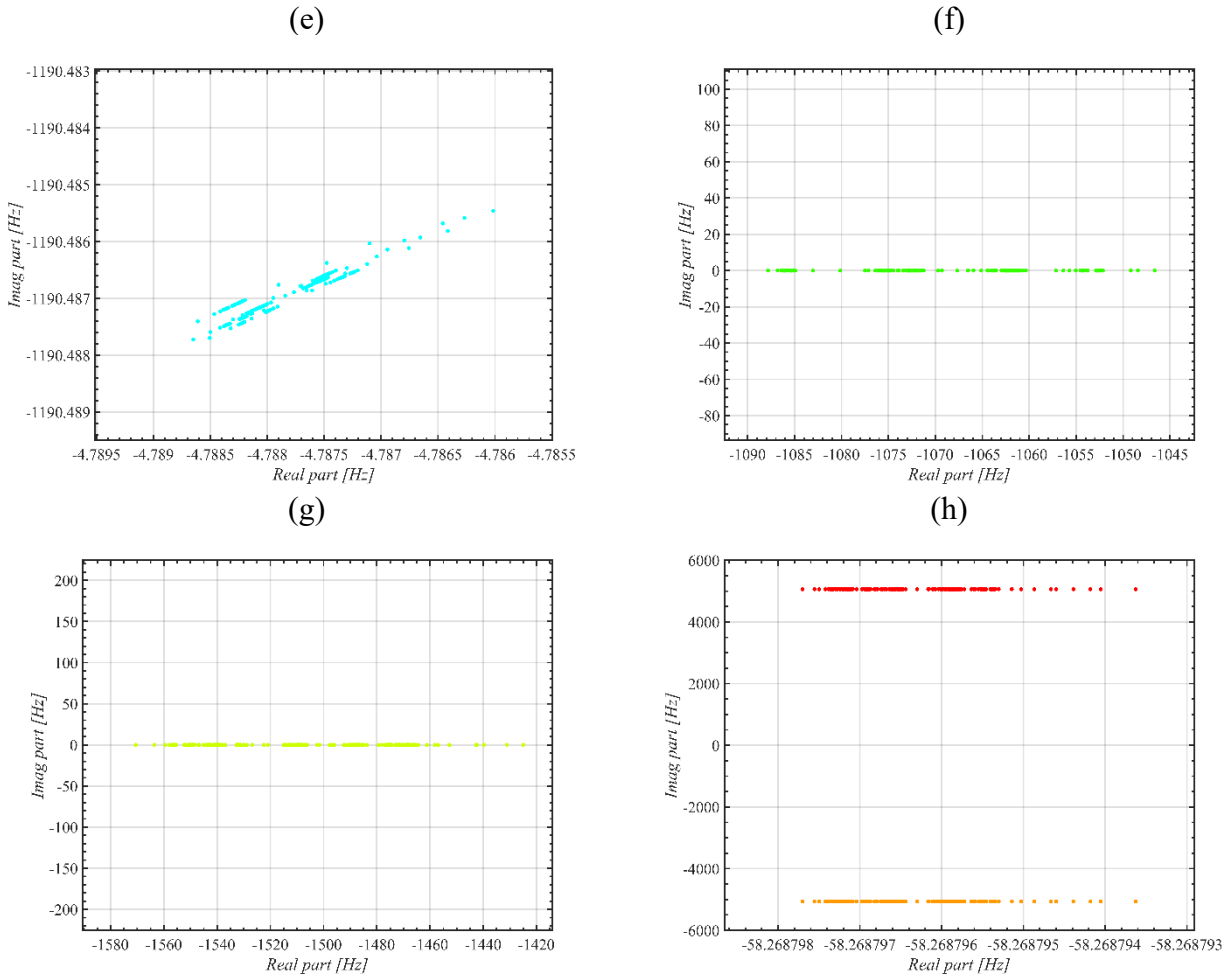

Figure 26. Eigenvalues locus by speed, the zoom view (a). Mode1, (b). Mode2 and 3, (c). Mode4, (d). Mode 5, (e). Mode 6, (f). Mode 7, (g). Mode 8, (h) Mode 9 and 10

This behavior confirms that the system preserves its stability throughout the operating range and supports the validity of the frozen-time (quasi-stationary) approach for analyzing the speed-dependent dynamics of the system. Moreover, it can be observed that the variation of each mode is relatively small within its respective scale. This limited shift in both modal frequency and damping indicates that the system dynamics change only slightly with operating speed, further supporting the validity and reliability of the frozen-time (quasi-stationary) approach for this system.

3.4 Dynamic Analysis

The dynamic behavior of the electromechanical system is investigated through the model that is developed in MATLAB/Simulink, representing the transmission system with the parameters listed in Table 3, Table 4 and Table 5. The drive shaft is powered by a 12-pole, 72-slot IPMSM, fully characterized using the FE-based software package, Altair [108], which is the dedicated simulation software package for designing and optimizing electric machines and as mentioned before, is utilized to drive the required data to build the numerical model of the objective motor.

The developed dynamic formulation results in a set of nonlinear ordinary differential equations (ODEs) describing the electromechanically coupled system. Due to the presence of strong nonlinearities, time-varying stiffness, backlash, and multi-scale dynamic interactions, the governing equations exhibit stiff behavior. These equations define the complete set of state variables associated with the mechanical and electromagnetic subsystems.

To ensure stable and efficient numerical integration of the stiff system, the MATLAB solver *ode23t*, which is based on a trapezoidal rule with free interpolant and is suitable for moderately stiff problems, is employed. The relative and absolute tolerances are specified as 10^-6 and 10^-8, respectively, in order to maintain a high level of numerical accuracy while preserving computational efficiency.

The reliability and accuracy of the numerical procedure are verified through a validation study. The obtained responses are compared with the reference results reported in Refs. [97] and [101], and a good agreement is observed. The details of this comparison and the validation process are presented in Section 3.2.

For dynamic analysis, the time-domain response of the system is computed under electromagnetic torque excitation. The primary response quantity considered is the dynamic transmission error (DTE) of the gear pair, which represents the relative torsional displacement between the meshing gears. To facilitate comparison and improve the generality of the results, the DTE is expressed in nondimensional form by normalizing it with respect to the backlash parameter, b.

The steady-state time histories are subsequently processed to extract characteristic dynamic features. In particular, the nondimensional DTE response is used to construct amplitude–frequency curves and bifurcation diagrams, which provide insight into the nonlinear dynamic behavior of the coupled system over a wide range of operating conditions.

Using the motor speed Ω_m as the bifurcation parameter, the simulations are conducted on the shaft speed range of [473.5, 3788.4] RPM, with a speed resolution of 16.57 RPM. This speed range is

selected based on the nominal operating characteristics of the considered electric motor. For each speed step, 7000 periods of simulation are evaluated, and the first 6000 periods are discarded to eliminate the transient effects.

Figure 27, illustrates a comparative analysis of the root mean square (RMS) values of the nondimensional dynamic transmission error (DTE) of the gear pair for three different mean torque levels. The responses are obtained over a range of rotational speeds considering both increasing and decreasing speed sweeps, allowing the identification of possible path-dependent phenomena and nonlinear dynamic effects.

The results clearly indicate that increasing the mean driving torque leads to a significant growth in the RMS amplitude of the DTE. This trend can be attributed to the higher dynamic load transmitted through the gear mesh, which enhances the nonlinear interaction between the time-varying mesh stiffness and the backlash nonlinearity. As the torque level increases, the system is driven deeper into the nonlinear operating regime, resulting in stronger vibration responses.

In addition, the response curves exhibit a pronounced nonlinear softening behavior. This phenomenon is mainly associated with partial tooth disengagement and intermittent loss of contact within the backlash zone. Such contact loss effectively reduces the average mesh stiffness, shifting the resonance region toward lower rotational speeds and modifying the overall dynamic characteristics of the system.

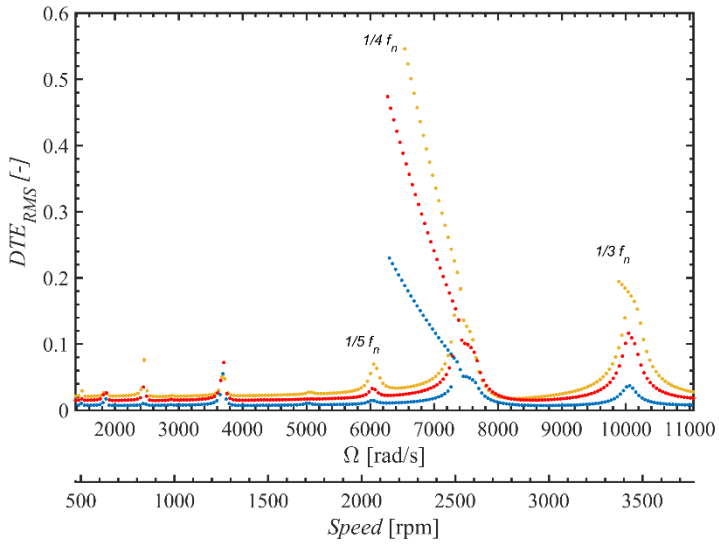

Figure 27. Amplitude frequency diagram in speed-up and speed-down analysis, T=163 Nm (blue), T=325 Nm (red), T=470 Nm (yellow).

A notable feature of the results is the presence of jump discontinuities in the amplitude–speed curves. These sudden transitions correspond to saddle-node bifurcations, where the system abruptly

shifts between low- and high-amplitude response states. The comparison between the acceleration and deceleration sweeps further reveals distinct differences in the response paths, indicating the existence of bistable regions and hysteresis. Within these regions, multiple stable solutions coexist, and the system response depends on the direction of the speed variation.

For the driving torque T_m is 470 Nm, with the mesh damping ratio $\zeta = 0.01$, the system exhibits its primary resonance at a rotational speed of 30.354E+3 rad/s. In addition to the fundamental resonance, several superharmonic resonances are observed due to the nonlinear characteristics of the gear mesh and backlash.

Specifically, the system response shows the occurrence of the 3rd, 4th, and 5th order superharmonic resonances at rotational speeds of 10,118.02 rad/s, 7,588.51 rad/s, and 6,070.81 rad/s, respectively. These superharmonic resonances arise from nonlinear excitation mechanisms associated with the periodic variation of the mesh stiffness and intermittent tooth contact, which enable energy transfer between the fundamental excitation frequency and its higher-order fractional components.

The presence of multiple superharmonic resonances indicates a strong nonlinear dynamic behavior, particularly under high torque conditions. Such resonant interactions contribute to localized amplification of the dynamic transmission error and may significantly affect the vibration and noise performance of the gear system within specific operating speed ranges.

Focusing on the 4th superharmonic resonance, which is associated with the highest vibration amplitudes, pronounced jump-up and jump-down phenomena are observed, highlighting the strongly nonlinear nature of the system. As can be observed in Figure 28, for a mean driving torque of 470 Nm, the jump-down event in the speed-decreasing simulation occurs at 2,229.7 RPM, whereas the jump-up transition in the speed-increasing simulation is observed at 2,494.4 RPM. When the mean torque is reduced to 325 Nm, the jump-down occurs at 2,138.2 RPM in the speed-down run, and the jump-up occurs at 2,484.7 RPM in the speed-up run. Finally, at a mean torque of 163 Nm, the jump-down in the speed-down simulation occurs at 2,147.8 RPM, while the jump-up in the speed-up run takes place at 2,493.2 RPM.

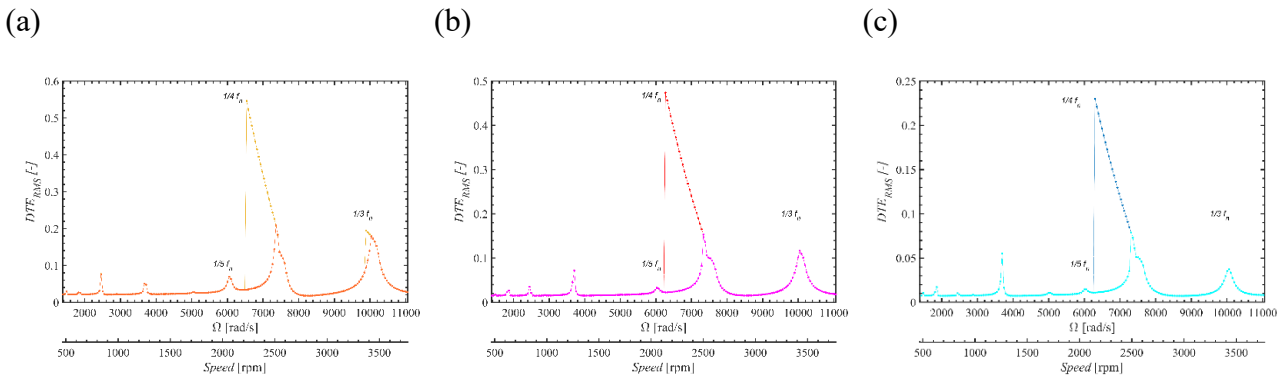

Figure 28 RMS diagram of speed-up and speed-down, (a) T=470 Nm, (b): T=325 Nm, (c): T=163 Nm.

These results clearly indicate that the nonlinear dynamic response of the gear system is strongly dependent on the applied torque level. Higher torque levels shift the operating points of the jump phenomena and amplify the associated vibration amplitudes, while lower torques tend to reduce the magnitude of the response but still exhibit bistable behavior. This torque-dependent behavior reflects the combined influence of nonlinear mesh stiffness, backlash, and superharmonic excitation on the dynamic characteristics of the system, emphasizing the critical role of operating conditions in determining gear system stability and performance.

The amplitude–frequency diagram provides important insights into the dynamic behavior of the gear system by quantifying the magnitude of the nondimensional dynamic transmission error (DTE). The DTE serves as a key indicator of gear mesh performance, reflecting both the presence of gear whine and the nonlinear effects associated with intermittent tooth contact and backlash. By examining the amplitude of the DTE across a range of rotational speeds, one can identify critical operating regions where the system exhibits resonant amplification or sudden transitions due to nonlinearities. However, while the amplitude–frequency diagram effectively captures the magnitude of the response, it does not provide information about the multiplicity of solutions or the potential coexistence of multiple stable and unstable states under the same operating conditions.

In contrast, a widely used technique for investigating qualitative changes in the response of nonlinear systems under parameter variations is the bifurcation diagram. In this representation, a characteristic measure of the system motion such as the peak value or RMS of the nondimensional dynamic transmission error (DTE) is plotted as a function of the control parameter, which in the present study is the rotor speed. This approach allows the identification of important nonlinear phenomena, including the coexistence of multiple steady-state solutions, subharmonic responses, and period-multiplication effects.

When the steady-state response is sampled once per gear-meshing period, the diagram provides a discrete representation analogous to a Poincaré map, facilitating the observation of periodicity

changes and subharmonic bifurcations. Moreover, the loss of continuity or the appearance of scattered points in the bifurcation diagram may indicate the transition from periodic motion to quasiperiodic or potentially chaotic behavior, although additional analyses are generally required to accurately classify the dynamic regime, as discussed in [105].

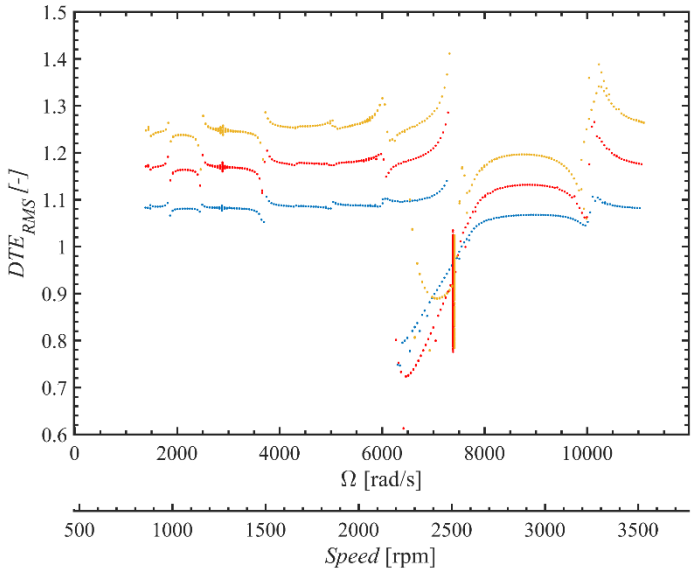

Figure 29. Bifurcation diagram of nondimensional DTE in speed down simulation for, T_m=163 Nm (blue), T_m=250 Nm (red), T_m=470 Nm (yellow).

Figure 29 presents the bifurcation diagrams obtained for three different mean torque levels under speed-decreasing (speed-down) simulations. The results show that the RMS values of the DTE increase with higher torque, reflecting the amplified nonlinear response of the gear system. In addition, the system exhibits a tendency toward non-periodic and potentially chaotic behavior at elevated torque levels. This is evident, for example, at a rotational speed of 2,528 RPM for a mean torque of 470 Nm, and at 2,518 RPM for a mean torque of 325 Nm, where the system transitions from periodic to aperiodic response regimes. Such observations highlight the strong dependence of the dynamic response on both the torque level and the operating speed, demonstrating the significance of torque-induced nonlinearities in the gear mesh and the potential for sudden changes in vibration and noise characteristics.

In order to provide a rigorous mathematical foundation for the observed dynamics, the Largest Lyapunov Exponent (LLE) across the rotor speed range, applying the Rosenstein method [114], is calculated. This quantitative analysis allows for a distinction between periodic, quasi-periodic, and chaotic regimes [115].

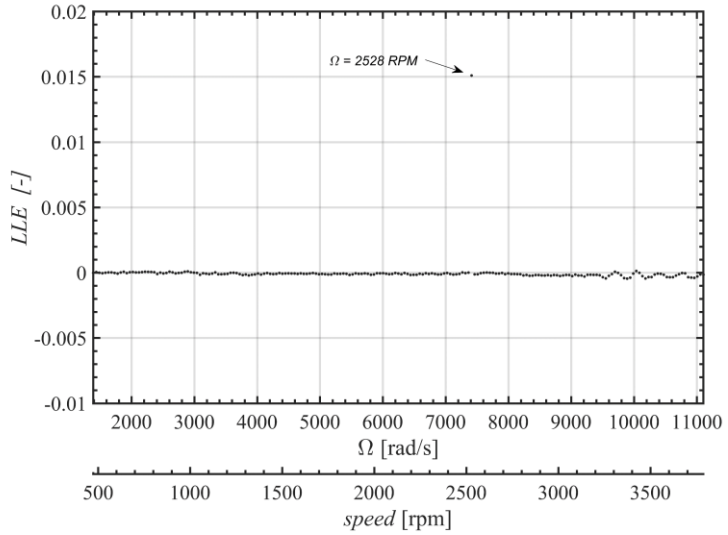

Figure 30 Largest Lyapunov Exponent of the state space derived from speed down simulation for T_m=470 Nm

Figure 30, represents the LLE of the state space vector across the speed range, applying 470 Nm torque, while the simulation is carried out in speed down direction. Taking into account that the system is non-autonomous, to maintain high fidelity across varying dynamics, an adaptive phase-space reconstruction was employed to the state space which includes time as the 11^{th} space, at each speed increment. The optimal time delay and embedding dimension were dynamically determined for each step via Average Mutual Information (AMI) and False Nearest Neighbors (FNN), respectively [114]. This approach ensures that the attractors are correctly unfolded regardless of the shifting complexity of the regimes.

As can be observed from Figure 30, LLE is almost zero all across the speed range, except for frequency of 2528 RPM. Which is 0.015; the positive LLE demonstrate the chaotic behavior at this frequency, as it represents divergence of adjacent trajectories in the state space.

3.5 Frequency Spectrum Analysis

In this section, a nonlinear dynamical framework is adopted to analyze the coupled electromechanical drivetrain system, with particular emphasis on identifying bifurcation phenomena and resonance-induced instabilities. The system under investigation is inherently nonlinear due to time-varying gear mesh stiffness, backlash nonlinearity, and electromagnetic torque ripple modulation. As a consequence, its response cannot be fully characterized using linear modal analysis alone. Time-domain simulations are therefore employed to capture the evolution of system trajectories in state space, enabling the detection of amplitude modulation, subharmonic generation, quasi-periodicity, and transitions to broadband and chaotic motion.

These features are interpreted within the context of bifurcation theory, where qualitative changes in system behavior arise as control parameters here, rotational speed are varied. In particular, Hopf bifurcations, period-doubling cascades, and secondary (superharmonic and subharmonic) resonance interactions are of primary interest, as they mark the onset of nonlinear instability and energy redistribution across frequency bands.

To complement the time-domain analysis, a speed-dependent spectral approach based on order-tracking methodology is employed. Since both mechanical and electromagnetic excitations scale proportionally with shaft speed, classical fixed-frequency Fourier analysis is insufficient to reveal their parametric evolution. Instead, RPM–frequency spectrograms are constructed to provide a time–frequency speed representation of the response.

This approach enables the tracking of harmonic orders defined as frequency components normalized by rotational speed across the operating range. Order tracking is particularly well suited to rotating machinery, as it distinguishes between excitation mechanisms tied to shaft rotation (e.g., gear meshing orders) and those associated with electromagnetic phenomena (e.g., pole-pair torque ripple orders). By expressing spectral components as functions of rotational order, resonance crossings and modal interactions become readily identifiable as intersections between excitation orders and structural eigenfrequency branches.

The combined use of nonlinear time-domain diagnostics and order-tracked spectral analysis provides a powerful framework for interpreting electromechanical coupling mechanisms. It allows the identification of internal resonance conditions in which integer combinations of excitation orders coincide with torsional eigenfrequencies, thereby triggering superharmonic or subharmonic responses. Moreover, the appearance of broadband spectral features or sudden amplitude growth can be interpreted as signatures of bifurcation-induced transitions, reflecting a qualitative change in

attractor topology in the underlying dynamical system. Such phenomena are characteristic of parametrically excited systems and cannot be predicted through purely linearized electric motor or gearbox models. Therefore, the adopted methodology enables not only the detection of instability thresholds but also a deeper understanding of the nonlinear mechanisms governing energy exchange between mechanical and electromagnetic subsystems.

The excitation mechanisms are characterized by the parametric forcing frequency $\Omega = 2\pi n z_p/60$, where n denotes the rotational speed (RPM) and z_p is the number of pinion teeth. From this expression, two primary families of harmonics emerge:

- Gear-meshing harmonics, which exhibit peaks at the fundamental meshing frequency $f_m = \Omega(2\pi)^{-1}$, and its multiples; These components arise from periodic stiffness variation and tooth engagement dynamics and are responsible for parametric excitation of the torsional system.

- Electromagnetic torque harmonics, which correspond to the ripple frequency $f_e = p\Omega\left(2\pi z_p\right)^{-1}$, and its multiples. These harmonics originate from spatial flux distribution, and slotting effects.

Since the system is driven by a 6-pole pair, 72-slot electric motor, the configuration considered herein is characterized by showing prominent electromagnetic torque harmonics at multiples of six. This structural periodicity directly influences the torque ripple signature and its interaction with the mechanical subsystem. In a 6-pole-pair, 72-slot machine, the spatial distribution of stator slots and rotor poles introduces a deterministic electromagnetic symmetry that governs the harmonic content of the air-gap flux density and, consequently, the developed electromagnetic torque. The discrete slotting effect modulates the permeance of the magnetic circuit, generating space harmonics that are mapped into time harmonics through rotor rotation. As a result, the electromagnetic torque contains characteristic harmonic components whose orders are directly linked to the pole–slot combination and the winding configuration. In particular, the periodicity imposed by the least common multiple of pole and slot numbers produces dominant torque ripple components at multiples of six electrical orders, which persist even under ideal sinusoidal current excitation.

These torque ripple harmonics act as speed-dependent parametric excitations applied to the mechanical drivetrain. Because their frequencies scale linearly with rotor speed, they sweep through the spectrum of torsional natural frequencies as operating conditions vary. When one of these electromagnetic orders approaches a structural eigenfrequency of the shaft–gear assembly, resonance amplification may occur. Importantly, this interaction is bidirectional: while electromagnetic torque

ripple excites mechanical vibration, the resulting torsional oscillations feed back into the electrical subsystem through speed-dependent back-EMF modulation and current control dynamics. This feedback loop alters the effective electromagnetic torque spectrum, potentially enhancing specific harmonic components and modifying their phase relationship with respect to the mechanical response.

From a nonlinear dynamics perspective, the structural periodicity of the machine therefore acts as a deterministic source of multi-harmonic forcing that can trigger superharmonic and subharmonic resonances in the coupled system. When combined with time-varying gear mesh stiffness and backlash nonlinearity, these harmonics contribute to complex internal resonance conditions, where integer combinations of electromagnetic and gear-mesh frequencies interact with torsional modes. The resulting dynamics may include amplitude modulation, frequency locking, or even bifurcation-induced transitions to quasi-periodic or broadband motion. Consequently, the electromagnetic structural symmetry is not merely a source of small torque ripple, but a fundamental driver of electromechanical coupling and dynamic stability in high-performance electric drivetrains.

3.5.1 Spectrogram Analysis

Figure 31 presents the RPM–frequency spectrogram of the nondimensional DTE response obtained from the speed-down simulation in the range 500–3800 RPM at a constant mean torque of 470 Nm. The representation clearly reveals two distinct families of excitation orders whose frequencies increase linearly with rotational speed. The first family corresponds to the gear-meshing harmonics f_m and its integer multiples which appear as straight lines with constant slope in the speed–frequency plane. These lines reflect the deterministic nature of the mesh excitation, whose frequency scales proportionally with shaft speed and tooth count. The second family corresponds to electromagnetic torque harmonics ($6f_e$,$12f_e$,$18f_e$,$24f_e$), which arise from the pole–slot configuration of the 6-pole-pair machine. The superposition of these harmonic families produces a structured lattice of excitation lines, whose intersections with structural resonance branches govern the dynamic amplification of the system. Three resonance tongues are clearly identified and labeled in the figure: the 5^{th}, 4^{th}, and 3^{rd} superharmonic resonances. The 5^{th} superharmonic resonance is observed at lower speeds, while the 4^{th} and 3^{rd} resonances emerge progressively as speed increases.

The most critical operating region is observed between approximately 2100 and 2600 RPM, as highlighted by the dashed vertical lines in Figure 31 Within this interval, the spectrogram exhibits a pronounced concentration of high-energy spectral components, indicating a localized amplification mechanism. Unlike other speed ranges where harmonic branches remain relatively distinct and well

separated, this region is characterized by the geometric convergence of multiple excitation families and resonance branches.

Specifically, the 4th superharmonic resonance branch clearly indicated in the upper frequency range of the spectrogram approaches and intersects several dominant excitation lines. Among these are the fundamental and higher-order gear-meshing harmonics $4f_m$, $5f_m$ and $6f_m$, which appear as inclined straight lines whose slope reflects their proportionality to shaft speed. Simultaneously, strong electromagnetic torque harmonics, particularly $6f_e$ and $12f_e$, also pass through this region. The visual overlap of these harmonic families produces a dense lattice of crossings concentrated within a relatively narrow speed window.

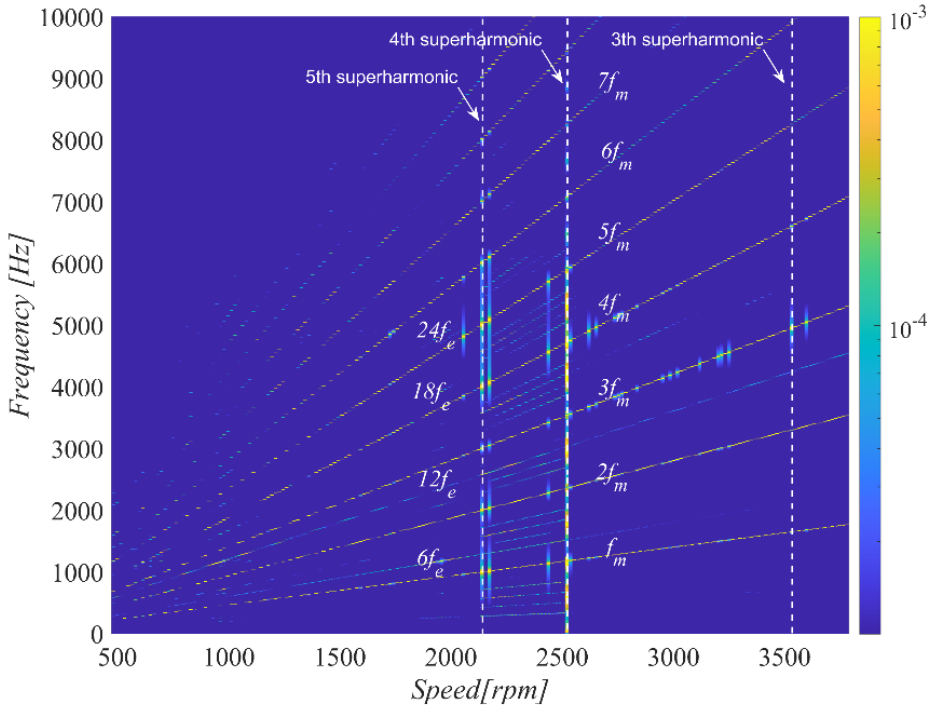

Figure 31. nondimensional DTE Spectrogram at 470 Nm.

This clustering is not merely geometric; it signifies the satisfaction of multiple near-commensurability conditions of the form

$$kf_m \approx f_n \qquad lf_e \approx f_n$$

where k and l are integers and f_n denotes a torsional natural frequency branch. When these conditions are simultaneously approached, the system experiences a multi-frequency internal resonance. In such a scenario, mechanical parametric excitation (via time-varying mesh stiffness) and electromagnetic torque ripple act coherently on the same structural mode, dramatically enhancing energy transfer into that mode.

The spectrogram confirms this behavior through visible spectral thickening and amplitude intensification along the intersecting branches. Instead of narrow, well-defined harmonic lines, the frequency content becomes broadened, indicating amplitude modulation and nonlinear frequency mixing. This broadening suggests that the response is no longer purely harmonic but includes sidebands and combination frequencies arising from nonlinear coupling terms. In other words, the system transitions from a linear superposition of independent excitations to a regime of nonlinear interaction where energy is redistributed across neighboring frequency bands.

The concentration of amplification in this speed window therefore reflects a resonance overlap phenomenon. From a nonlinear dynamics standpoint, this overlap reduces the effective stability margin of the system and facilitates transitions to subharmonic or quasi-periodic motion. Indeed, the subsequent appearance of broadband spectral features near 2528.7 RPM suggests that this internally resonant region acts as a precursor to bifurcation, marking the onset of qualitative changes in system behavior. Therefore, the 2100–2600 RPM interval represents a critical electromechanical interaction zone where gear-mesh superharmonic resonance and electromagnetic torque harmonics coincide. The resulting multi-frequency coupling leads to enhanced vibration amplitudes, spectral broadening, and the emergence of nonlinear dynamic phenomena that cannot be predicted by analyzing either subsystem independently.

A particularly striking feature appears at 2528.7 RPM, where a nearly vertical broadband structure emerges. Unlike the inclined harmonic lines, which follow deterministic speed-proportional scaling, this vertical feature indicates the activation of a wide frequency band over a narrow speed interval. Such a spectral signature is a classical indicator of bifurcation-induced dynamics. The broadband content suggests that the system undergoes a qualitative transition in attractor structure, consistent with the non-periodic behavior identified in the bifurcation diagram (Figure 29). From a nonlinear dynamic perspective, this behavior corresponds to a chaotic motion triggered by superharmonic resonance overlap.

Moreover, the amplification is not confined to a single harmonic order; rather, it spreads across adjacent mesh and electromagnetic components. This spreading is indicative of nonlinear energy exchange between subsystems, where torsional oscillations modulate rotor speed, altering back-EMF and current dynamics, which in turn feed back into the torque ripple spectrum as can be observed in Figure 32. Such bidirectional coupling reinforces certain harmonics while destabilizing others, creating the observed dense spectral texture. In Figure 32, this phenomenon is particularly evident in the region bounded by the dashed vertical lines, where not only the dominant branch (e.g., $12f_e$) exhibits high amplitude, but neighboring components such as $6f_e$, $18f_e$, f_m, $2f_m$, and $3f_m$ also experience

noticeable growth. Instead of isolated, sharply defined harmonic lines, the spectrum displays clustered and broadened ridges, indicating that energy is being redistributed across multiple frequency channels.

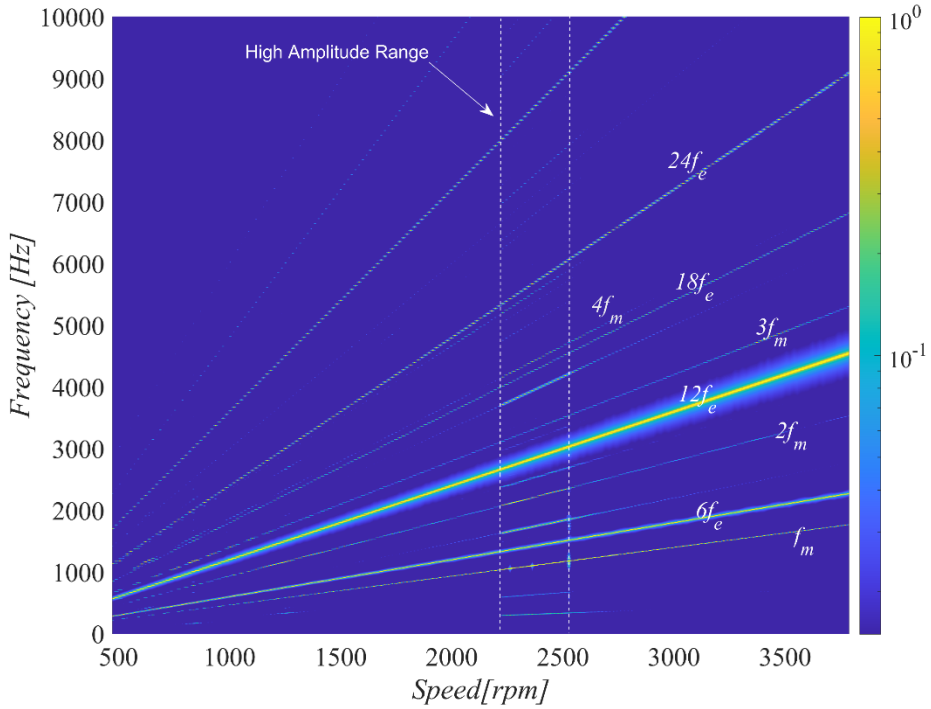

Figure 32. Electromagnetic torque Spectrogram.

This spreading is a clear signature of nonlinear energy exchange between the mechanical and electrical subsystems. The gear mesh excitation introduces periodic torsional oscillations at f_m and its multiples. These oscillations produce instantaneous speed fluctuations of the rotor, which directly perturb the electrical angle and modulate the back-EMF. Because the electromagnetic torque depends nonlinearly on current and electrical angle, these speed perturbations generate amplitude and phase modulation of the torque ripple components. As a result, new combination frequencies and sideband structures emerge around the principal electromagnetic harmonics.

In Figure 32, this interaction manifests as amplification not only along the primary electromagnetic orders (e.g., $12f_e$) but also along adjacent orders and mesh-related components. The coexistence and mutual amplification of kf_m and lf_e branches suggest that the system satisfies near-commensurability conditions over a finite speed interval. Under such conditions, internal resonance mechanisms become active, enabling bidirectional energy transfer: mechanical oscillations modulate the electromagnetic torque, and the resulting torque ripple feeds back into the torsional dynamics.

The spectral thickening and increased color intensity in the highlighted high-amplitude range further indicate that the response is no longer purely harmonic. Instead, nonlinear modulation produces

frequency spreading and local broadband characteristics, consistent with amplitude–phase coupling and possible secondary bifurcation behavior. This confirms that the observed amplification is not a linear superposition effect but rather the outcome of strong electromechanical coupling.

Therefore, Figure 32 provides direct spectral evidence of nonlinear interaction: torsional oscillations alter rotor speed, modifying back-EMF and current dynamics, which in turn reshape the torque ripple spectrum. The distributed amplification across adjacent harmonic families is a hallmark of coupled nonlinear systems operating near resonance overlap conditions.

Therefore, the presence of electromagnetic harmonics aligned with mechanical mesh orders highlights the bidirectional nature of the electromechanical coupling. When electromagnetic torque harmonics coincide with mesh harmonics or their superharmonic resonance branches, the torque ripple is amplified not merely as a passive excitation but as part of a feedback-mediated resonance loop. Mechanical oscillations modulate rotor speed, which in turn alters back-EMF and current control dynamics, reinforcing specific torque harmonics. This coupling mechanism explains why the highest amplification occurs in the interval bounded by the 4^{th} and 5^{th} superharmonic branches; a region where multiple excitation orders simultaneously approach structural eigenfrequencies.

Importantly, such amplification cannot be captured by a purely electrical motor model or by a purely mechanical gear model. The spectrogram demonstrates that instability emerges only when mechanical parametric excitation and electromagnetic harmonic content overlap in the speed–frequency domain. Therefore, the observed dynamics are a consequence of nonlinear electromechanical interaction rather than isolated subsystem behavior. Overall, Figure 31 reveals that the drivetrain dynamics are governed by a hierarchy of speed-dependent resonances, whose crossings generate localized instability pockets. The coexistence of deterministic harmonic orders, superharmonic resonance branches, and broadband bifurcation signatures confirms that the system operates within a nonlinear parametric regime, where small variations in speed can trigger significant qualitative changes in vibration behavior.

3.5.2 Single Response Time-domain and Spectral Analysis

In this section, the dynamic transmission error (DTE) response of the gear pair and its frequency content are analyzed under selected single-harmonic excitation scenarios. This approach enables a detailed investigation of the system's nonlinear dynamic characteristics within the critical speed ranges, with particular emphasis on resonance mechanisms, harmonic interactions, and the onset of instability phenomena. To address this, the DTE response and the electromagnetic torque, induced

by IPM motor affected by the interactions with transmission dynamics and control strategy is investigated and analyzed, in vicinity of the critical excitation frequencies:

- $\Omega_m = 2230$ RPM

In this context, at 2230 RPM corresponding to the jump-down frequency shown in Figure 29, the system resides near a nonlinear bifurcation point where the fundamental periodic response loses stability and a higher-period solution emerges. This critical regime is dominated by strong modal interaction and harmonic coupling. For clarity, the DTE response of the gear pair and the electromagnetic torque response are examined independently, so that the mechanisms responsible for the instability and the subsequent electromechanical feedback can be systematically identified. Regarding the DTE response, both the speed-down and speed-up simulation are presented, in order to address the nonlinear dynamic response of the system.

Figure 33(a) presents the time-domain response of the nondimensional DTE at 2230 RPM while the simulation has been done in speed down approach. The same speed is considered reporting the DTE of the transmission in Figure 33(d) when the simulation has been done in speed- up manner. The waveform exhibits a clearly periodic pattern in both cases; however, the harmonic signature and the amplitude are different in speed-up and speed-down. The signal shows modulation and distortion, indicating that the motion results from the interaction of multiple harmonic components rather than from a single dominant excitation.

The spectral content of the DTE, shown in Figure 33(b, e), reveals the emergence of 7T-subharmonic oscillations. Distinct spectral peaks appear at approximately k (1040.55)/7 Hz, with k an integer. where 1040.55 Hz corresponds to the fundamental gear-mesh frequency f_m. This confirms that the transmission response has undergone a period-seven multiplication relative to the primary meshing excitation which is confirmed by looking to the Poincaré section Figure 33(c, f).

Such subharmonic generation is a classical signature of nonlinear dynamics and indicates the occurrence of a secondary bifurcation from the fundamental periodic solution. Instead of oscillating synchronously with the mesh frequency, the system locks into a longer periodic orbit whose period is seven times the mesh period. The presence of these fractional harmonics demonstrates that nonlinear stiffness modulation and parametric excitation effects within the gear pair dominate the response in this operating condition.

For reference, the mesh harmonics f_m and its multiples are marked with red dashed lines, while the electromagnetic harmonic family $6f_e$ and its multiples are indicated by blue dashed lines. The DTE spectrum clearly shows that the mechanical excitation family governs the subharmonic structure.

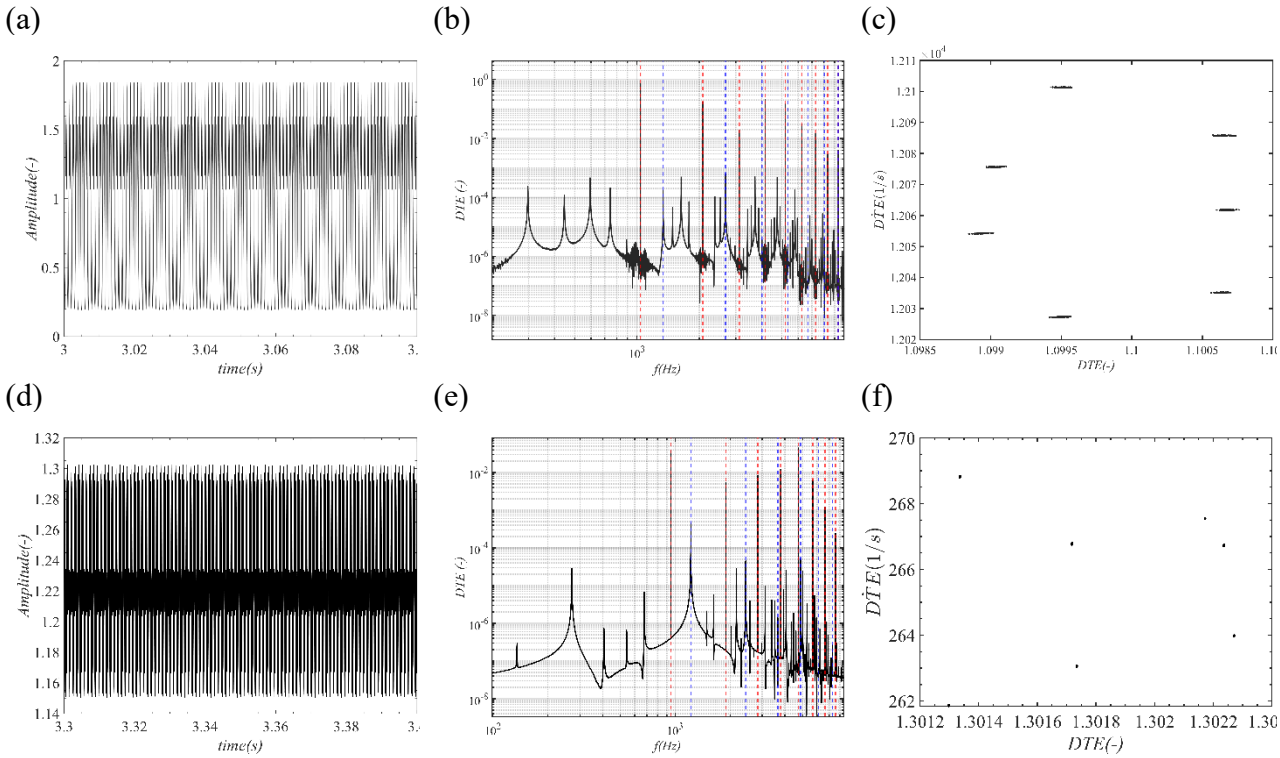

Figure 33. (a) DTE time history, (b) DTE spectra, (c) Poincare Section at 2230 RPM in speed-down simulation, (d) DTE time history, (e) DTE spectra, (f) Poincare Section at 2230 RPM in speed-up simulation.

To address the dynamic analysis of the electromagnetic torque, Figure 34(a) shows the time-domain record of the electromagnetic torque at the aforementioned operating speed. Although the torque signal remains periodic, its waveform reflects the influence of multiple interacting frequency components. The torque oscillations are not solely determined by intrinsic electromagnetic ripple but are visibly shaped by the mechanical dynamics of the transmission.

The torque spectrum, shown in Figure 34(b), provides direct evidence of this interaction. The dominant harmonic component is the gear-mesh frequency, $f_m = 1040.55$ Hz demonstrating that mechanical excitation strongly modulates the electromagnetic torque. This is a key result: the torque ripple is not governed exclusively by electrical slotting or pole-pair harmonics, but is substantially driven by the transmission dynamics.

Notably, in the presence of subharmonic vibrations originating from gear meshing, the torque spectrum exhibits non-negligible peaks at 297.6 Hz, and 594 Hz, corresponding to $2/7f_m$ and $4/7f_m$, respectively. These fractional components originate from the 7T-subharmonic oscillations observed in the DTE response. Their presence in the torque spectrum confirms that the mechanically generated subharmonic motion propagates back into the electrical subsystem. This behavior clearly indicates strong electromechanical coupling between the IPM and the mechanical transmission. The torsional vibrations generated within the gear pair are not effectively attenuated by shaft compliance; instead, they induce rotor speed fluctuations that perturb the electrical angle, back-EMF, and stator current

dynamics. These perturbations are then reflected in the torque ripple spectrum, closing a bidirectional feedback loop between mechanical and electrical domains.

(a) (b)

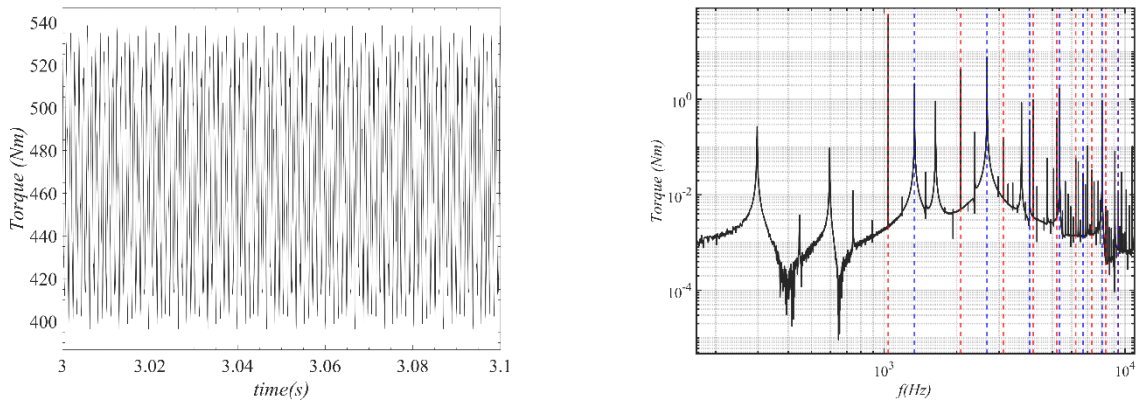

Figure 34 (a) Torque time history, and (b) Torque spectra, at 2230 RPM

Thus, while the DTE response demonstrates the nonlinear period-multiplying behavior of the gear pair, the torque response reveals how this nonlinear mechanical phenomenon actively reshapes the electromagnetic dynamics.

The system's dynamic response in proximity to the super harmonic resonance regimes is presented below, which show the time histories and spectra analysis of the DTE and the electromagnetic drive torque, respectively.

- $\Omega_m = 3450$ RPM

A detailed analysis of the system's dynamic behavior in proximity to the 3rd superharmonic resonance regimes is presented in this section. Figure 35 focuses on the operating condition at 3450 RPM, corresponding to the 3rd superharmonic resonance of the gear pair. At this speed, the mesh excitation frequency satisfies $f_m = \frac{1}{3} f_n$, placing the system in a one-third frequency commensurability condition. Under this regime, the nonlinear characteristics of the gear mesh, primarily the time-varying stiffness and backlash nonlinearity play a crucial role in shaping the response. Even though the excitation acts at f_m, the one-third relationship with the natural frequency changes the stability and amplitude of the oscillatory motion. This frequency commensurability changes the sensitivity of the system to harmonic interactions and promotes nonlinear distortion of the DTE waveform.

Figure 35 (a, b) presents the time histories and corresponding frequency spectra of the dynamic transmission error (DTE) at speed down simulation condition, allowing the nonlinear features

associated with the $\frac{f_n}{3}$ regime to be clearly identified. In particular, the results highlight how superharmonic resonance conditions alter the spectral distribution and amplify specific harmonic components, revealing the inherently nonlinear nature of the transmission dynamics.

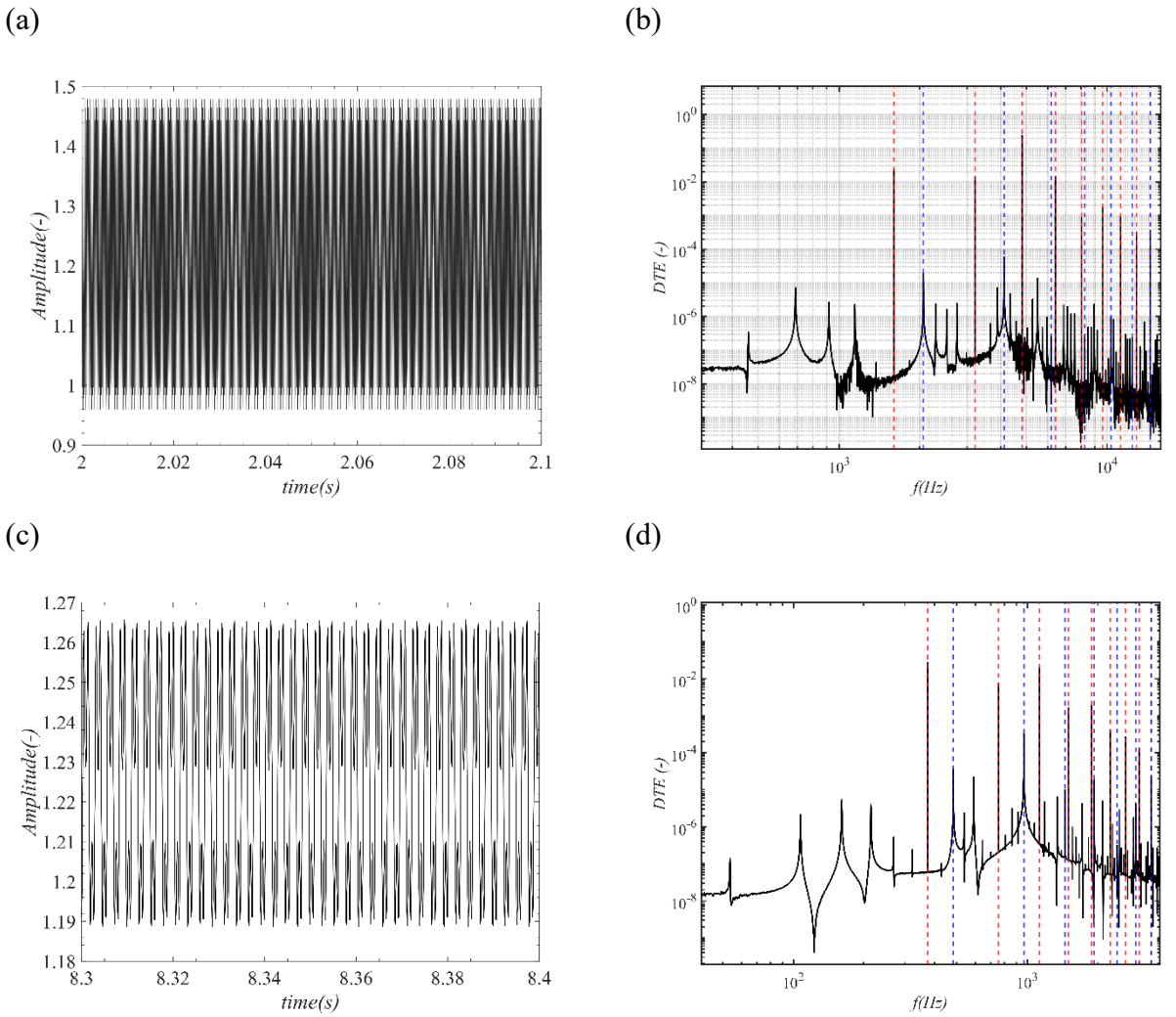

Figure 35 Nondimensional DTE time history and spectrum at 470 Nm torque at 3rd (3450 RPM), (a, b): Speed-down, (c, d): speed-up

From Figure 35(b), the response is predominantly governed by the gear-meshing harmonic family. The highest DTE magnitudes are associated with integer multiples of the mesh frequency f_m, which are indicated by the red dashed lines. This confirms that the principal vibration energy originates from the meshing orders, as expected for a transmission system where periodic stiffness variation constitutes the primary excitation mechanism.

At the operating condition corresponding to the 3rd superharmonic regime, the spectral distribution exhibits a distinct amplification pattern. As shown in Figure 35(b), when the excitation frequency decreases to touch the 3rd superharmonic resonance (in speed-down simulation), the maximum DTE amplitude occurs at the third meshing harmonic $3f_m$. In addition to the dominant $3f_m$ contribution, the spectrum reveals the presence of fractional components at $2/7f_m$, $3/7f_m$, $4/7f_m$, and $5/7f_m$. These

components appear as modulation sidebands and reflect nonlinear interaction mechanisms within the gear pair. Their presence indicates amplitude and phase modulation of the primary meshing oscillation, leading to a structured but non-uniform spectral distribution. By contrast, the components at $1/7f_m$ and $6/7f_m$ remain negligible, suggesting that the nonlinear energy transfer favors specific fractional orders rather than generating a fully symmetric subharmonic spectrum.

This is however different when the excitation frequency increase to reach the 3rd superharmonic resonance (in speed-up simulation), as can be seen in Figure 35(c, d). From Figure 35(a), the DTE peak to peak amplitude is lower compared to DTE in the speed- down condition, and the harmonic content presents different signature as well. While, the dominant contribution is from f_m and $3f_m$, the spectrum reveals the presence of fractional harmonic components at $k/7f_m$ (Figure 35(d)).

In order to investigate the influence of the electromechanical coupling on the electromagnetic torque, the time history steady state response and the spectra of T_m in presence of 3rd superharmonic resonance are presented in Figure 36(a, b). From the time history record, at 3450 RPM, the torque oscillates around the mean drive torque of approximately 470 Nm with a dense, highly periodic high-frequency ripple. The waveform remains stable and does not exhibit amplitude modulation or subharmonic beating, indicating that the system operates in a periodic steady-state regime despite being in the vicinity of a nonlinear superharmonic condition.

(a) (b)

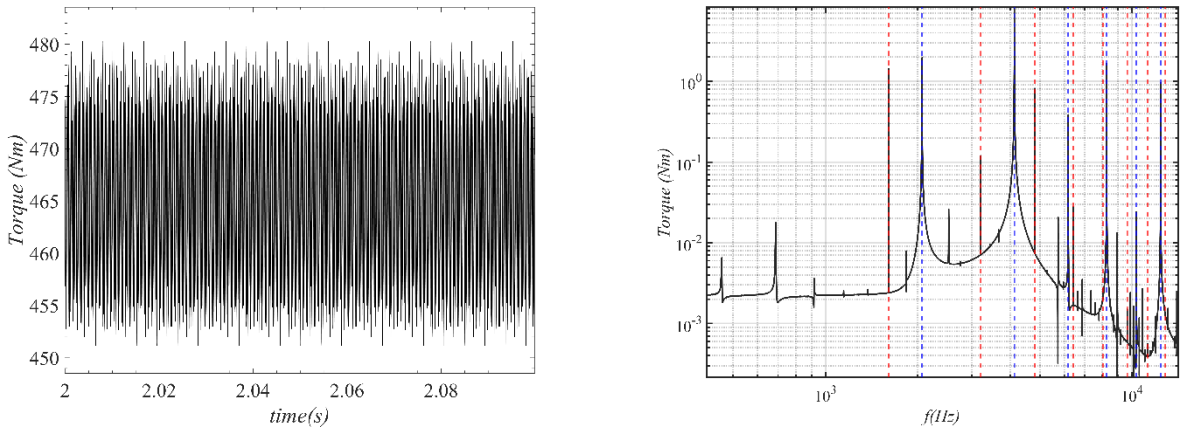

Figure 36. Torque time history and spectrum at 470 Nm (a, c): 3rd (3450 RPM) superharmonic resonance

However, the torque ripple is clearly non-sinusoidal. The fine structure of the oscillations suggests the superposition of multiple harmonic components rather than dominance by a single frequency. The resulting peak-to-peak variation corresponds to a torque ripple of approximately 3.2% at 3450 RPM. This confirms that the torque ripple amplitude is not constant across operating speeds but depends strongly on the prevailing harmonic interactions in each resonance regime.

The spectral analysis in Figure 36(b) provides deeper insight into the harmonic content of the torque. The dominant components align with the gear-meshing harmonic family (red dashed lines) and the electromagnetic harmonic family (blue dashed lines), demonstrating the coexistence of mechanical and electrical excitation orders in the torque response.

In particular, strong amplification is observed at higher mesh multiples, especially at f_m. The presence of pronounced peaks at this order confirms that the mechanical transmission dynamics significantly influence the electromagnetic torque. However, the dominant frequency orders at 3450 RPM are $6f_e$ and $12f_e$.

Unlike the previously discussed 7T-subharmonic regime, the present spectrum does not show significant fractional $k/7f_m$ components. Instead, the response is characterized by integer harmonic amplification, indicating that the system remains in a stable periodic orbit without period multiplication. The results clearly demonstrate that, under the 3rd superharmonic condition, the torque ripple is strongly shaped by the mechanical meshing dynamics. The periodic stiffness variation of the gear pair modulates rotor speed and electrical angle, thereby imprinting mechanical harmonic content onto the electromagnetic torque. Even though the response remains periodic, the redistribution of spectral energy toward higher mesh orders reflects nonlinear electromechanical coupling. The transmission does not merely act as a passive load; instead, it actively reshapes the torque ripple structure through harmonic interaction mechanisms.

- $\Omega_m = 2588$ RPM

The dynamic behavior of the gear pair at 2588 RPM, corresponding to the 4th superharmonic resonance, exhibits distinctive characteristics due to the interplay between mesh excitation and system nonlinearities. At this operating condition, the mesh frequency satisfies f_m = 1/4 f_n, placing the system in a one forth superharmonic commensurability regime. At 2588 RPM, corresponding to the 4th superharmonic resonance, the gear pair exhibits a distinct dynamic tooth engagement (DTE) response characterized by noticeable amplitude as can be seen in Figure 27. It is worth-noticing that the high amplitude DTE occurs at thus speed when the system experiences speed down condition.

Analysis of the DTE time history, (Figure 37(a)), indicates that the oscillations are consistent and periodic, while the high peak to peak amplitude suggests a strong resonance condition at this operating speed. The corresponding frequency spectrum, as shown in Figure 37(b), reveals that the dominant harmonic is driven by $4f_m$ harmonic, representing the maximum energy content. In addition to this primary meshing harmonic, all 7T modulations appear across the spectrum, reflecting the influence of the gear's tooth passage and transmission error patterns. A notable observation is the

presence of electromagnetic harmonics, f_e and its multiples, within the DTE spectrum, indicating that interactions between the gear mesh dynamics and the system's electromagnetic excitations also contribute to the overall vibration response. Comparison of the DTE responses under speed-down and speed-up conditions (Figure 37(a) and (b)) reveals significant nonlinear characteristics, emphasizing the need to consider the complete dynamic operating range for accurate system response prediction.

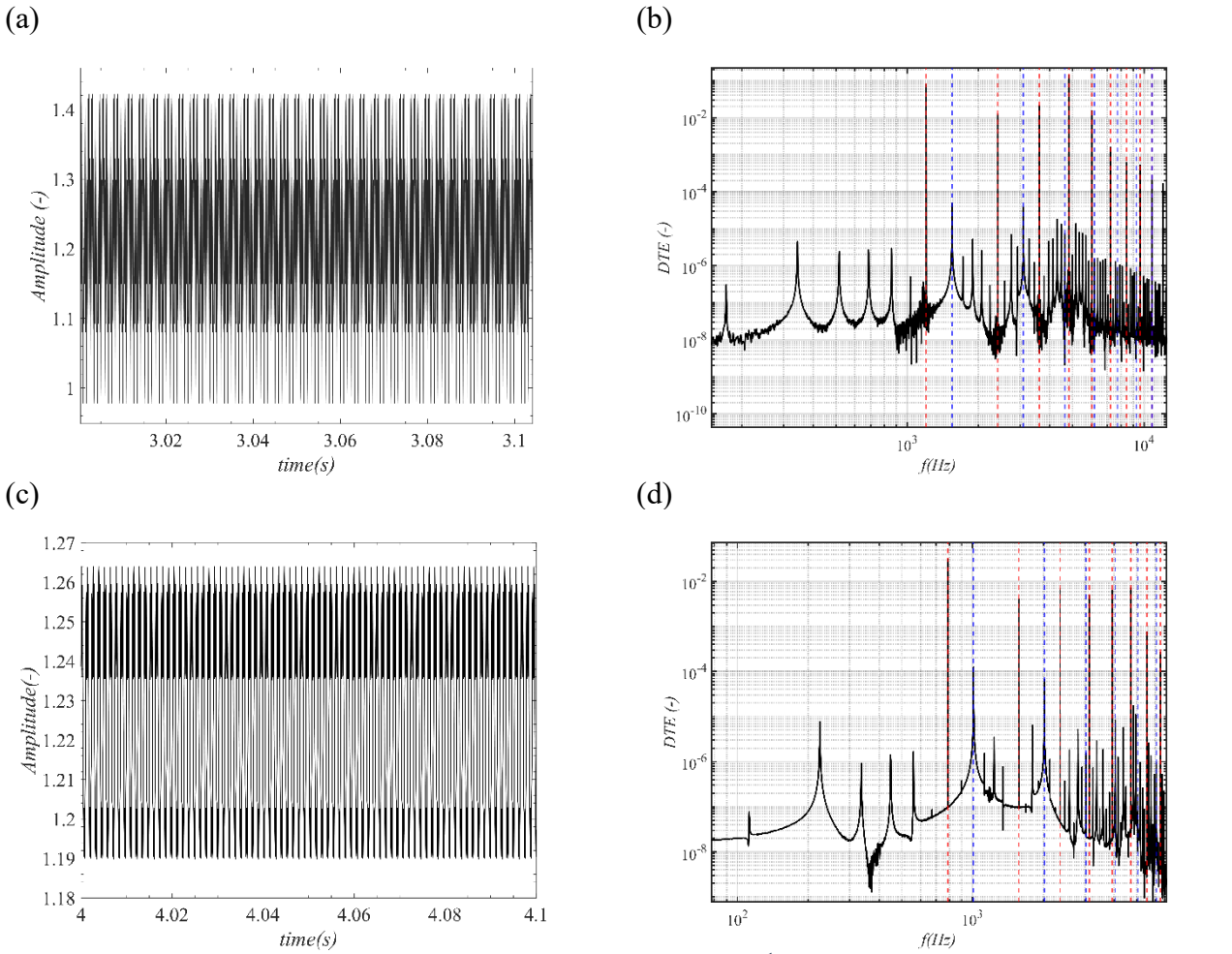

Figure 37. Nondimensional DTE time history and spectrum at 470 Nm torque at 4thsuperharmonic (2588 RPM), (a, b): Speed-down, (c, d) Speed-up simulation.

Similar to the previous step, to investigate the influence of the electromechanical coupling on the electromagnetic torque, the time history steady state response and the spectra of T_m in presence of 4th superharmonic resonances are presented in Figure 38(a-b). From the time history record, the first evidence is that the torque ripple is different compared to the torque ripple in the 3rd superharmonic resonance. As can be observed from Figure 38(a), the drive torque ripple is 7.3% at 2588 RPM. This indicates that, in different operational speeds due to the presence of different dominant harmonics the electromagnetic torque sees different harmonics and different ripple level. Moreover, from the frequency spectra of the torque, Figure 38(b), one can observe that the dominant frequency orders at

2588 RPM, the highest peak is due to the fundamental gear mesh harmonic f_m ,while as observed before the dominant harmonic in the 3rd superharmonic excitation was $12f_e$. However, yet as it is evident from Figure 38(b), the electromagnetic harmonics, $6f_e$ and $12f_e$ are pronounced significantly in the spectra. This behavior confirms the presence of electromechanical coupling phenomena, where the torque generated by the motor is not only affected by the characteristic of the electric system, but also from the fluctuation induced by the parametric forcing resulting from the gear mesh stiffness variation.

(a) (b)

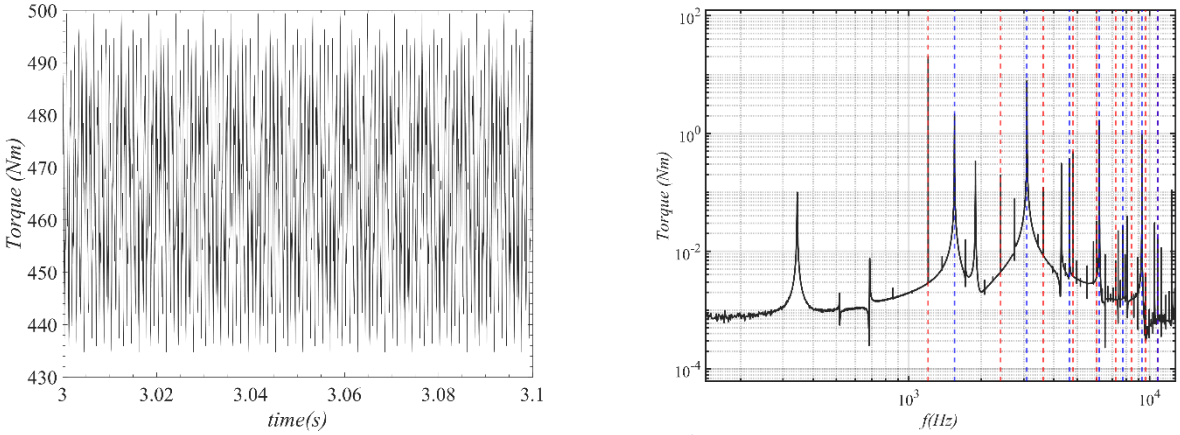

Figure 38. Torque time history and spectrum at 470 Nm 4th superharmonic resonance (2588 RPM).

- $\Omega_m = 2528$ RPM

According to the bifurcation diagram shown in Figure 29, where the dynamic transmission error (DTE) exhibits indications of chaotic behavior, a detailed investigation is conducted at 2528 RPM under a torque of T_m = 470 Nm. Examination of the time-domain response (Figure 39(a)) reveals behavior that is only slightly periodic, suggesting that the system is near a transition between periodic and more complex dynamic regimes. This observation is reinforced by the corresponding frequency spectrum (Figure 39(b)), which shows distinct harmonic peaks associated with the input mesh frequency and its multiples (highlighted by red dashed lines). These harmonics confirm that the meshing behavior still dominates the system response, while on the other hand, the electromagnetic harmonic orders vanished in this specific frequency.

However, the spectrum also exhibits a broadband energy distribution, indicative of the presence of complex, nonperiodic dynamics. The combination of sharp harmonics and continuous spectral components suggests that the system's response is influenced by mechanical nonlinearities, such as time-varying stiffness and tooth contact nonlinear backlash, rather than by electromechanical interactions. This interpretation is further supported by the Poincaré section of the DTE (Figure 39(c)), which displays distribution of points that exhibits the intricate, non-repeating geometric

structure of a strange attractor, a hallmark of chaotic oscillations [105]. This structural complexity, combined with the previously calculated positive LLE, confirms that the loss of strict periodicity stems from mechanical nonlinearities rather than electromechanical coupling.

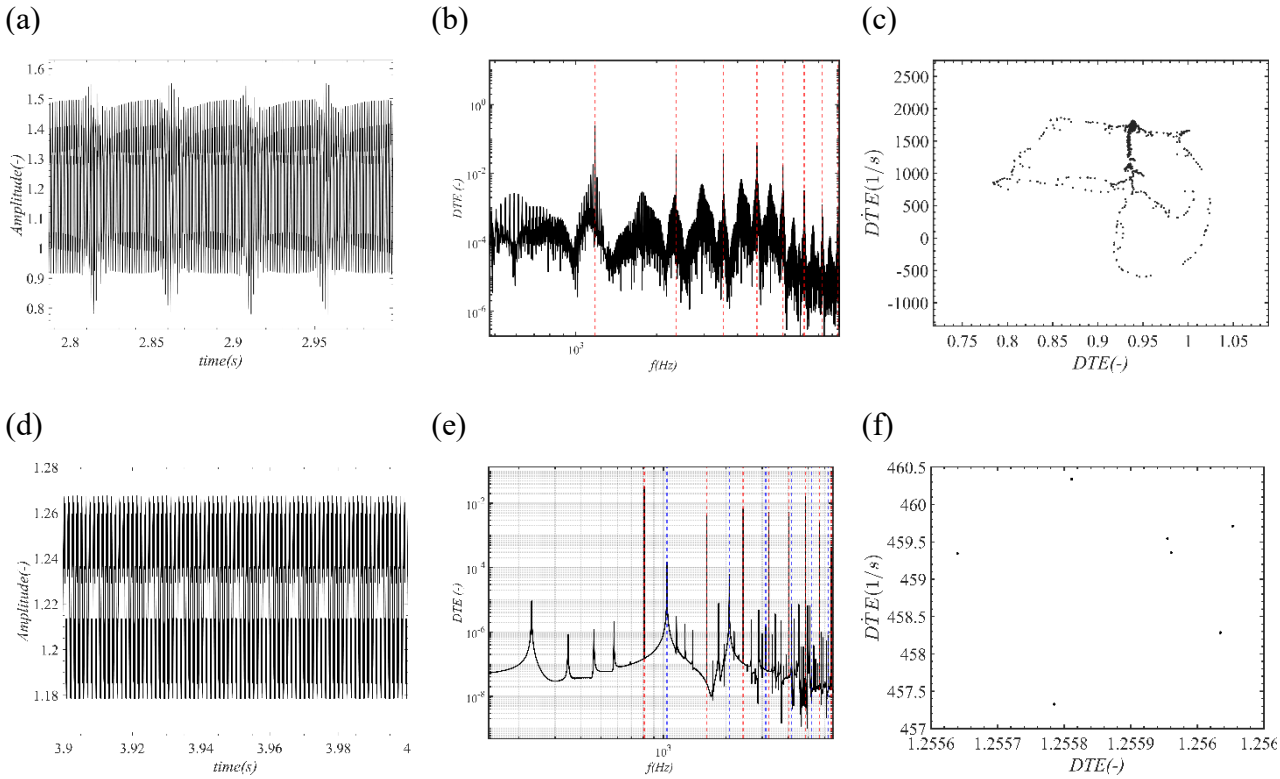

Figure 39. Nondimensional DTE response at 470 Nm and 2528 RPM: (a) time history, (b) spectrum, and (c) Poincaré section, at speed-down. (d) time history, (e) spectrum, and (f) Poincaré section at speed-up simulation.

The FFT of the DTE response reveals strong harmonic components at integer multiples of the excitation frequency, together with significant broadband spectral content. The presence of higher-order harmonics and the continuous frequency background indicate pronounced nonlinear distortion and energy transfer across a wide frequency range.

Although the system at 2528 RPM experiences a chaotic behavior when is under speed down simulation, the dynamic response is different in the same speed if the speed up simulation is utilized. As can be observed from Figure 39(d), the DTE response has both different amplitude and periodicity pattern compared to Figure 39(a). This is more supported by presenting the FFT spectrum of the response as can be seen in Figure 39(e), where the spectrum shows distinct harmonic peaks associated with the electromagnetic harmonics, f_e. Moreover, 7T modulations corresponding to f_m appear in low frequency range of the spectrum, reflecting the influence of the gear's tooth passage. From comparison of Figure 39(c) and Figure 39(f), one can observe the shift of a chaotic behavior to a period-7, by changing the simulation from speed-down direction to speed-up direction.

In summary, the results at 2528 RPM demonstrate a complex interplay between dominant meshing harmonics and nonlinear modulations, producing a chaotic DTE response in speed-down direction and a period-7 response that underscores the nonlinear nature of the gear transmission dynamics under high torque conditions.

3.6 Electromagnetic Parameters Analysis

The evaluation of the electromagnetic torque and the identification of gear mesh harmonics in its frequency spectrum indicate that mechanical excitations originating from the gearbox propagate back to the motor through the shaft. These state oscillations alongside the speed fluctuations, in turn affect the electromagnetic state variables such as I_d and I_q and stator flux linkages through the electromechanical coupling and the action of the control system. To investigate this interaction, the electromagnetic state variables are analyzed in both the time and frequency domains in this section. This analysis is particularly important because the time response of the d-q currents, as well as their deviation from the reference values, provides insight into the ability of the control strategy to reject mechanically induced disturbances and maintain torque tracking under gear–motor coupling conditions.

3.6.1 Spectral Analysis

Figure 40 illustrates the RPM–frequency spectrograms of the I_d and I_q currents obtained during the speed-down simulation over the range of 500–3800 RPM at a constant mean load torque of 470 Nm. The representations reveal that the current responses are not limited to their control-related low-frequency content but exhibit a rich harmonic structure that evolves with rotational speed.

Two principal families of frequency components can be distinguished. The first corresponds to the electromagnetic orders associated with the electrical frequency f_e and its integer multiples. These components appear as straight lines whose slopes are proportional to speed, reflecting the deterministic relationship between electrical frequency and rotor velocity. The second family originates from mechanical disturbances transmitted from the drivetrain, primarily the gear-mesh frequency f_m and its harmonics. The presence of these components in the current spectra indicates that torsional oscillations are fed back into the electrical subsystem through speed modulation and control action.

The interaction between these electrical and mechanical orders produces a structured pattern of intersecting frequency branches. As rotational speed varies, several of these branches approach the torsional resonance regions previously identified in the mechanical analysis. When such proximity occurs, the spectrograms display localized amplification zones, indicating increased sensitivity of the current response to electromechanical coupling.

(a)

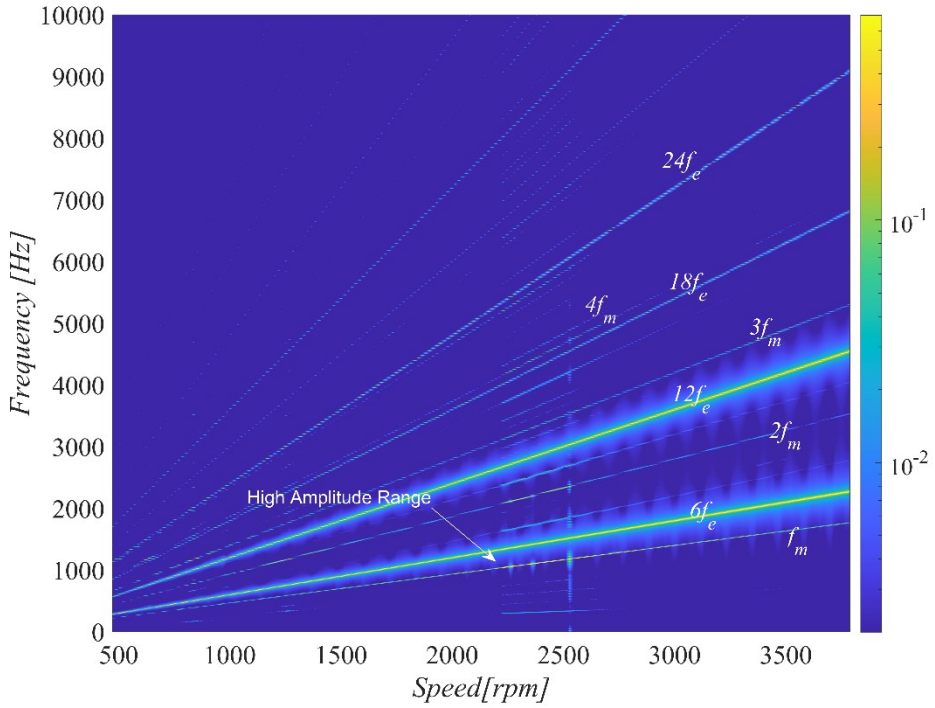

(b)

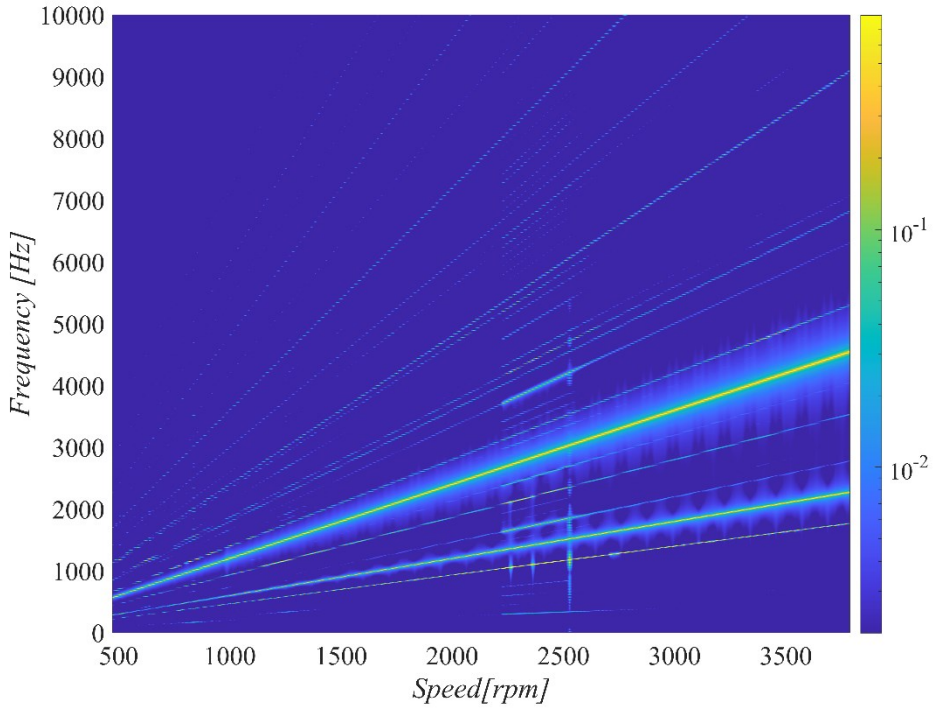

Figure 40 Current Spectrogram signature of (a): I_d and (b): I_q

A particularly pronounced interaction is observed in the speed interval between approximately 2100 and 2600 RPM. Within this region, the spectrograms of both I_d and I_q exhibit intensified spectral levels and noticeable thickening of several harmonic branches. Unlike lower-speed regions, where

individual orders remain narrow and well separated, the current spectra here show clustered and broadened ridges, suggesting amplitude modulation and frequency mixing.

This behavior can be interpreted as a consequence of rotor speed oscillations induced by gear-mesh excitation. Torsional vibrations modulate the instantaneous electrical angle and frequency, which directly affects the back-EMF. Since the current controllers attempt to regulate the I_d and I_q currents in the presence of these disturbances, the control system introduces additional dynamic components, causing mechanical harmonics to appear in the electrical variables. Consequently, frequency components at f_m as well as combination terms around the electromagnetic orders become visible in the spectra.

The spectral broadening observed in the highlighted speed range indicates that the current response departs from purely periodic behavior. Instead, amplitude–phase modulation generates sidebands around the dominant electrical harmonics, revealing nonlinear interaction between the mechanical oscillations and the control dynamics. Near approximately 2528.7 RPM, the spectrograms display a localized broadband feature extending over a relatively wide frequency band within a narrow speed interval.

Overall, the current spectrograms provide clear evidence of bidirectional electromechanical coupling. Mechanical vibrations generated by gear-mesh excitation induce speed fluctuations that perturb the electrical dynamics through back-EMF and control action. The resulting current variations modify the electromagnetic torque, which in turn feeds back into the torsional motion. The distributed amplification and frequency spreading observed in both I_d and I_q therefore reflect a closed electromechanical interaction loop.

Importantly, such behavior cannot be captured by a purely electrical motor model operating under ideal speed conditions. The presence of mechanical orders and their interaction with electromagnetic harmonics demonstrates that the observed dynamics arise from the coupled system. The spectrogram analysis thus confirms that the electrical variables carry clear signatures of the mechanical resonances and that significant current distortion occurs in the same speed interval where resonance overlap and instability pockets were identified.

3.6.2 Single-speed currents in time-domain

- $\Omega_m = 2230$ RPM

At 2230 RPM corresponding to the jump-down frequency shown, where the system resides near a nonlinear bifurcation point.

Figure 41(a) presents the time domain response of I_d and I_{dref} at 2230 RPM when the simulation is in speed down direction. The red curve corresponds to I_d and the blue one represents the reference direct current in this speed, in the steady state condition and in a narrow time frame. The same speed is considered reporting the time domain response of I_q and I_{qref} is represented in Figure 41(b). The waveform exhibits a clearly periodic pattern in both cases; however, signal shows modulation and distortion, indicating that the motion results from the interaction of multiple harmonic components rather than from a single dominant excitation.

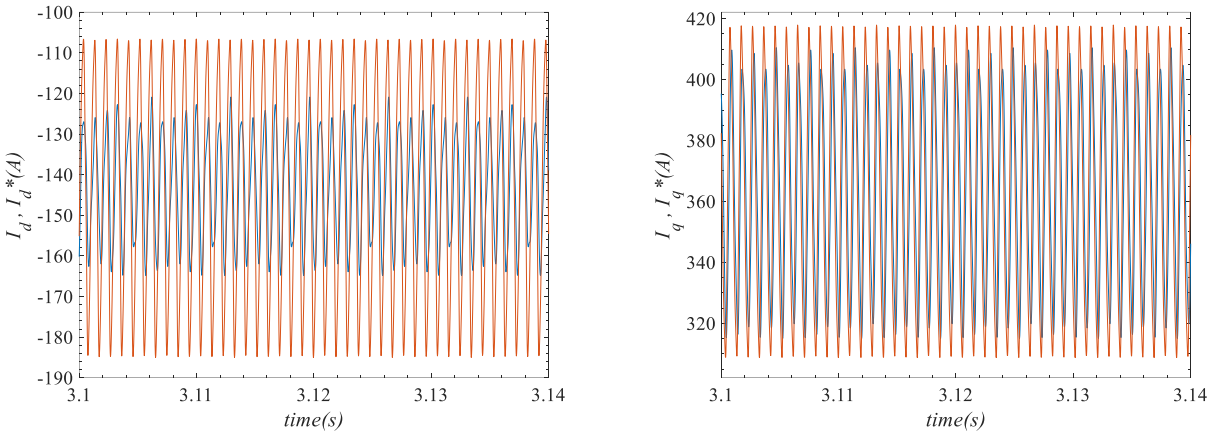

Figure 41.Time response of (a): I_d and I_{dref}, (b): I_q and I_{qref} at 2230 RPM, by applying 470 Nm

- $\Omega_m = 2588$ RPM

The other speed regime that is critical to observe the coupling effect of gear meshing harmonics on the current is at 2588 RPM, corresponding to the 4th superharmonic resonance, where the gear pair exhibits a distinct DTE response characterized by noticeable amplitude.

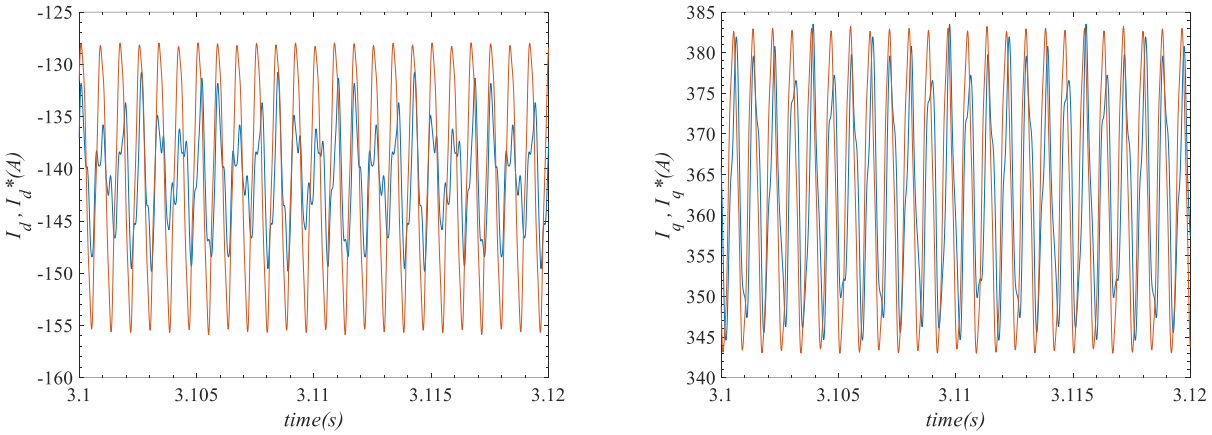

Figure 42. Time response of (a): I_d and I_{dref}, (b): I_q and I_{qref} at 2588 RPM, by applying 470 Nm

Figure 42(a) presents the time domain response of I_d and I_{dref} at 2588 RPM when the simulation is in speed down direction, and Figure 42(b) reports the time domain response of I_q and I_{qref} in the same speed. As observed, both current components track their reference values, although they exhibit

oscillations caused by meshing and electromagnetic harmonics. The magnitude and harmonic content of these oscillations depend on the excitation frequency and its interaction with the system's resonant modes.

Chapter 4: Conclusions

This work presented a comprehensive nonlinear dynamic investigation of a gear transmission system subjected to both mechanical and electromechanical excitations. A high-fidelity modeling framework was developed to capture the key physical mechanisms governing the torsional response of an electric powertrain. The proposed model integrates a finite-element-based IPM motor representation, drive-shaft torsional compliance, and a nonlinear gear contact formulation including time-varying mesh stiffness, transmission error excitation, and load-dependent torque conditions. The system was solved in the time domain, and the dynamic transmission error (DTE) was adopted as the primary NVH indicator. The dynamic behavior was analyzed over a wide operating speed range using time histories, frequency spectra, bifurcation diagrams, phase portraits, and order-tracked spectrograms.

The reconstruction of the time-varying mesh stiffness demonstrated a clear load dependence, with both the mean value and fluctuation amplitude increasing with torque. These variations significantly influence the dynamic response and confirm that realistic load-dependent stiffness modeling is essential for accurate prediction of drivetrain vibrations. Validation of the numerical framework was carried out in two stages. First, the mechanical subsystem reproduced experimental dynamic transmission error (DTE) trends reported in the literature. Second, the multi-degree-of-freedom model showed good agreement with simplified single-degree-of-freedom results while revealing additional dynamic features associated with shaft compliance and distributed inertia, confirming the reliability of the solver.

Linear modal analysis showed that the purely mechanical system exhibits three dominant modes: a low-frequency rigid-body torsional mode, an intermediate gear–shaft mode, and a high-frequency mesh mode. When electromagnetic dynamics and control were included, additional electrical poles appeared and the torsional modes became partially coupled with the electrical states. The electromechanical interaction produced measurable frequency shifts, including an increase of approximately 7.8% in the mesh-mode frequency, and introduced frequency-dependent damping effects. Eigenvalue locus analysis further confirmed that the system remains stable over the operating speed range, supporting the frozen-time linearization approach.

Nonlinear time-domain simulations revealed a strong dependence of the response on operating torque and speed. Increasing torque significantly amplified the DTE and shifted resonance regions toward lower speeds due to effective softening associated with backlash and intermittent contact. The amplitude–speed responses exhibited jump phenomena, hysteresis, and bi-stability, indicating saddle-node bifurcations. In addition to the primary resonance, multiple superharmonic resonances were identified, highlighting the strongly nonlinear nature of the drivetrain dynamics. Bifurcation analysis

further showed that higher torque levels promote transitions from periodic to chaotic behavior, with a critical operating region consistently observed between approximately 2100 and 2600 RPM.

Order-tracked spectrogram analysis revealed that this critical region is governed by the geometric convergence of two excitation families: gear-meshing harmonics and electromagnetic torque harmonics. This clustering reflects near-commensurability conditions between excitation orders and torsional eigenfrequencies, leading to multi-frequency internal resonance. The resulting interaction manifests as spectral thickening, amplitude intensification, and broadened harmonic ridges, indicating amplitude modulation, nonlinear frequency mixing, and energy redistribution. Around 2528 RPM, a broadband structure was observed, corresponding to a bifurcation-induced transition toward chaotic motion and reduced dynamic stability.

Detailed single-speed analyses provided further insight into the underlying mechanisms. At 2230 RPM, period-seven subharmonic oscillations were identified in the DTE and confirmed through spectral analysis and Poincaré sections. Importantly, these mechanically generated subharmonics were also present in the electromagnetic torque spectrum, demonstrating that torsional oscillations propagate back into the electrical subsystem through rotor speed modulation. At higher superharmonic conditions, such as 2588 RPM, large DTE amplitudes were accompanied by increased torque ripple, confirming the sensitivity of electromagnetic torque to mechanical resonance.

Frequency-domain results provided clear evidence of bidirectional electromechanical coupling. Electromagnetic harmonic components were observed in the DTE spectrum, indicating that motor torque ripple contributes directly to mechanical vibration. Conversely, gear-meshing harmonics and their combinations were detected in the electromagnetic torque and in the i_d and i_q current spectra, showing that mechanical oscillations modulate the electrical variables through speed fluctuations and control dynamics. This mutual spectral exchange confirms the existence of a feedback loop between the mechanical and electrical subsystems, in which each domain both excites and responds to the other.

Overall, the results demonstrate that the drivetrain operates within a nonlinear parametric regime, where resonance crossings between speed-dependent excitation orders and structural modes create localized instability zones. The most severe vibration and torque amplification occurs when gear-mesh superharmonic branches and electromagnetic harmonics simultaneously approach torsional natural frequencies. Such phenomena cannot be predicted using purely mechanical gearbox models or standalone motor models and require fully coupled nonlinear analysis.

The proposed framework therefore provides a powerful predictive tool for NVH-oriented design of electric drive units. It enables the identification of critical speed–torque regions, resonance overlap conditions, and electromechanical instability mechanisms, supporting design decisions related to gear geometry, shaft stiffness, motor electromagnetic configuration, and control bandwidth.

The main contributions of this study can be summarized as follows:

1. Development of a high-fidelity hybrid nonlinear electromechanical model of an electric powertrain implemented in Simulink, combining FE-based IPMSM torque generation with time-varying mesh stiffness obtained from detailed gear contact analysis.
2. Reconstruction of load-dependent mesh stiffness from static transmission error analysis, enabling realistic representation of nonlinear gear contact behavior.
3. Frozen-time modal characterization demonstrating the emergence of stable low-frequency electromechanical modes and quantifying the influence of electromagnetic coupling on torsional natural frequencies.
4. Comprehensive nonlinear analysis through amplitude–frequency responses, bifurcation diagrams and Largest Lyapunov Exponent analysis under multiple torque levels, revealing superharmonic resonances, hysteresis, bi-stability, and transitions to chaotic behavior.
5. Identification of a critical operating region (2100–2600 RPM) where near-commensurability between gear-mesh and electromagnetic harmonics produces multi-frequency internal resonance.
6. Spectral evidence of bidirectional coupling, including the presence of electromagnetic harmonics in the DTE spectrum and gear-meshing components in electromagnetic torque and current signals, confirming mutual energy transfer between the electrical and mechanical subsystems.
7. Demonstration that resonance overlap between electrical and mechanical excitation orders can lead to increased vibration levels and potential NVH issues, providing practical guidance for the design and operation of electric drivetrain systems.

Future work may extend the present study through longer-time simulations and the incorporation of bearing dynamics to further improve the predictive capability of the model. Additional developments may include experimental validation and parametric study on the effectiveness of the control bandwidth and mechanical properties of shafts on mitigation of the vibration due to the reverse modulations.

Appendix

Appendix A

Table A. 1 lists the mesh stiffness values obtained from the static analysis extracted from Transmission 3D.

Table A. 1 Mesh stiffness components (N/m)

Position NO.	At 470 Nm	At 325 Nm	At 165 Nm
1	310975030.14	311160582.67	311558060.38
2	310029852.68	310214815.45	310608952.20
3	308365250.33	308548902.65	308938776.27
4	305964932.98	306147369.30	306530336.36
5	323797458.27	303105277.34	303479884.75
6	368650827.95	363033490.03	345737769.89
7	380554321.39	380781139.71	381379336.58
8	380603302.21	380830340.45	381426639.07
9	380034844.06	380261526.71	380855335.09
10	380200668.23	380426998.84	381020609.87
11	375646010.49	373951259.16	368395936.44
12	336940275.10	321591115.13	306587701.14
13	308298728.19	308482395.82	308873969.29
14	309963853.92	310148985.14	310544389.96
15	310853835.88	311038804.58	311436473.57

Appendix B

The modal characterization of the system is proceeded as is explained in Section 3.3, resulting in the matrices A and B, which are reported in (B.1,2).

$$\mathbf{A} = \begin{pmatrix} 1.407\,E-4 & -1.591\,E-5 & -9.820\,E-1 & 0 & 0 & 0 & 0 & 0 & 0 & 0 \\ -1.591\,E-5 & 2.070\,E-4 & 0 & -1.934 & 0 & 0 & 0 & 0 & 0 & 0 \\ 0 & 0 & 1 & 0 & 0 & 0 & 0 & 0 & 0 & 0 \\ 0 & 0 & 0 & 1 & 0 & 0 & 0 & 0 & 0 & 0 \\ 0 & 0 & 0 & 0 & 1 & 0 & 0 & 0 & 0 & 0 \\ 0 & 0 & 0 & 0 & 0 & 1 & 0 & 0 & 0 & 0 \\ 0 & 0 & 0 & 0 & 0 & 0 & 1 & 0 & 0 & 0 \\ 0 & 0 & 0 & 0 & 0 & 0 & 0 & 7.018\,E-2 & 0 & 0 \\ 0 & 0 & 0 & 0 & 0 & 0 & 0 & 0 & 9.914\,E-4 & 0 \\ 0 & 0 & 0 & 0 & 0 & 0 & 0 & 0 & 0 & 5.250\,E-3 \end{pmatrix} \quad \text{(B.1)}$$

$$\mathbf{B} = \begin{pmatrix} 2.00E-2 & 0 & -1.26E+2 & 0 & 0 & 0 & 0 & -5.99E-1 & 0 & 0 \\ 0 & 2.00E-2 & 0 & -1.26E+2 & 0 & 0 & 0 & 6.42E-1 & 0 & 0 \\ 1 & 0 & 0 & 0 & 0 & 0 & 0 & 0 & 0 & 0 \\ 0 & 1 & 0 & 0 & 0 & 0 & 0 & 0 & 0 & 0 \\ 0 & 0 & 0 & 0 & 0 & 0 & 0 & -1 & 0 & 0 \\ 0 & 0 & 0 & 0 & 0 & 0 & 0 & 0 & -1 & 0 \\ 0 & 0 & 0 & 0 & 0 & 0 & 0 & 0 & 0 & -1 \\ 9.03\text{E}-1 & -9.32\text{E}-1 & 0 & 0 & 2.00E+5 & -2.00E+5 & 0 & 7.00\text{E}-2 & 7.00E-2 & 0 \\ 0 & 0 & 0 & 0 & -2.00E+5 & 7.29E+5 & -8.12E+5 & -7.00\text{E}-2 & 4.51E-1 & -5.85E-1 \\ 0 & 0 & 0 & 0 & 0 & -8.12E+5 & 1.25E+5 & 0 & -5.85E-1 & 9.68E-1 \end{pmatrix} \quad \text{(B.2)}$$

5. References

[1] Krause PC, Wasynczuk O, Sudhoff SD. *Analysis of electric machinery and drive systems*. 2nd ed. New York: Wiley-IEEE; 2002.

[2] Zeraoulia M, Benbouzid MEH, Diallo D. Electric motor drive selection issues for HEV propulsion systems: A comparative study. *IEEE Transactions on Vehicular Technology*. 2006;55(6):1756–1764. doi:10.1109/TVT.2006.878719.

[3] Lewthwaite E. Magnetic equivalent circuits for electrical machines. In: *Proceedings of the Institution of Electrical Engineers*. IET; 1967. p. 1805–1809.

[4] Ostović V. Magnetic equivalent circuit presentation of electric machines. *Electric Machines & Power Systems*. 1987;12(6):407–432. doi:10.1080/07313568708960120.

[5] Ostovic V. A novel method for evaluation of transient states in saturated electric machines. *IEEE Transactions on Industry Applications*. 1989;25(1):96–100. doi:10.1109/28.18874.

[6] Blondel A. *Synchronous motors and converters: Theory and methods of calculation and testing*. New York: McGraw-Hill; 1913.

[7] Park RH. Two-reaction theory of synchronous machines: Generalized method of analysis—Part I. *Transactions of the AIEE*. 1929;48(3):716–727. doi:10.1109/T-AIEE.1929.5055275.

[8] Kim YK. Analytical study considering both core loss resistance and magnetic cross saturation of interior permanent magnet synchronous motors. *Journal of Magnetics*. 2012;17(4):280–284.

[9] Kallio S, Karttunen J, Andriollo M, Peltoniemi P, Silventoinen P. Finite element-based phase-variable model in the analysis of double-star permanent magnet synchronous machines. In: *International Symposium on Power Electronics, Electrical Drives, Automation and Motion*. IEEE; 2012. p. 1462–1467.

[10] Harley RG, Limebeer DJN, Chirricozzi E. Comparative study of saturation methods in synchronous machine models. *IEE Proceedings B – Electric Power Applications*. 1980;127(1):1–7.

[11] Xie G, Ramshaw RS. Nonlinear model of synchronous machines with saliency. *IEEE Transactions on Energy Conversion*. 1986;1(3):198–204.

[12] Yan X et al. Dynamic circuit model considering core losses and phase interaction for switched reluctance machines. *IET Electric Power Applications*. 2018. doi:10.1049/iet-epa.2017.0693.

[13] Abbaszadeh A, Maroufian S. Axial flux permanent magnet motor modeling using magnetic equivalent circuit. In: *Iranian Conference on Electrical Engineering*. 2013. doi:10.1109/iraniancee2013.6599603.

[14] Iglesias I, García-Tabares L, Tamarit J. A d–q model for the self-commutated synchronous machine considering magnetic saturation. *IEEE Transactions on Energy Conversion*. 1992;7(4):768–776.

[15] Levi E, Vučković V. Field-oriented control of induction machines in the presence of magnetic saturation. *Electric Machines & Power Systems*. 1989;16(2):133–147.

[16] Levi E, Vukosavic S, Vuckovic V. Saturation compensation schemes for vector-controlled induction motor drives. In: *21st Annual IEEE Conference on Power Electronics Specialists*. 1990. p. 591–598.

[17] Levi E, Vučković V. Rotor flux computation in saturated field-oriented induction machines. *Electric Machines & Power Systems*. 1993;21(6):741–754.

[18] Levi E. Applications of the current state-space model in analyses of saturated induction machines. *Electric Power Systems Research*. 1994; 31:203–216.

[19] Levi E. A unified approach to main flux saturation modeling in d–q axis models of induction machines. *IEEE Transactions on Energy Conversion*. 1995;10(3):455–461.

[20] Levi E. Saturation modeling in d–q axis models of salient pole synchronous machines. *IEEE Transactions on Energy Conversion*. 1999;14(1):44–50.

[21] Belmans R, Vandenput A, Geysen W. Calculation of the flux density and the unbalanced pull in two-pole induction machines. *Archiv für Elektrotechnik*. 1987;70(3):151–161.

[22] Frosini L, Pennacchi P, Stoisser CM. Analysis of unbalanced magnetic pull calculation in generators with two pole pairs. In: *ASME Biennial Conference on Mechanical Vibration and Noise*. 2009. p. 1195–1203.

[23] Im H, Yoo HH, Chung J. Dynamic analysis of a BLDC motor with mechanical and electromagnetic interaction due to air-gap variation. *Journal of Sound and Vibration*. 2011;330(8):1680–1691.

[24] Huang C, Lei F, Han X, Zhang Z. Determination of modeling parameters for a brushless DC motor for electric vehicle applications. *Measurement and Control*. 2019; 52:002029401984260.

[25] Sudhoff SD, Kuhn BT, Corzine KA, Branecky BT. Magnetic equivalent circuit modeling of induction motors. *IEEE Transactions on Energy Conversion*. 2007;22(2):259–270.

[26] Jung JW, Lee JJ, Kwon SO, Hong JP, Kim KC. Equivalent circuit analysis of interior permanent magnet synchronous motor considering magnetic saturation. *World Electric Vehicle Journal*. 2009;3.

[27] Amrhein M. *Induction machine performance improvements: Design-oriented approaches*. PhD Thesis, University of Illinois at Urbana-Champaign; 2007.

[28] Tavana N, Dinavahi V. Real-time nonlinear magnetic equivalent circuit model of induction machine for hardware-in-the-loop simulation. *IEEE Transactions on Energy Conversion*. 2016.

[29] Asghari B, Dinavahi V. Experimental validation of a nonlinear permeance network-based real-time induction machine model. In: *IEEE Power and Energy Society General Meeting*. 2012.

[30] Townsend DP. *Gearing*. NASA; 1985.

[31] Jones A. *A portable cosmos: Revealing the Antikythera mechanism*. New York: Oxford University Press; 2017.

[32] Lewis MJT. Gearing in the ancient world. *Endeavour*. 1993;17(3):110–115.

[33] Willis R. *Principles of mechanism*. London; 1841.

[34] Moon FC. Robert Willis and Franz Reuleaux: Pioneers in the theory of machines. *Notes and Records of the Royal Society*. 2003;57(2):209–230.

[35] Lewis W. Investigation of the strength of gear teeth. *Proceedings of the Engineering Club of Philadelphia*. 1892.

[36] Buckingham E. Dynamic loads on gear teeth. ASME; 1931.

[37] Almen O, Straub JC. Durability of automotive transmission gears. SAE; 1937.

[38] ISO 6336-1, 1996. Calculation of load capacity of a spur and helical gears. Part 1: Basic principles, introduction and general influence factors.

[39] ISO 6336-2, 1996. Calculation of load capacity of a spur and helical gears. Part 2: Calculation of surface durability (pitting).

[40] ISO 6336-3, 1996. Calculation of load capacity of a spur and helical gears. Part 3: Calculation of tooth bending strength.

[41] ISO 6336-5, 1996. Calculation of load capacity of a spur and helical gears. Part 5: Strength and quality of materials.

[42] Harris SL. Dynamic loads on the teeth of spur gears. *Proceedings of the Institution of Mechanical Engineers*. 1958; 172:87–112.

[43] Tuplin WA. Gear tooth stresses at high speed. *Proceedings of the Institution of Mechanical Engineers*. 1950; 163:162–167.

[44] Tuplin WA. Dynamic loads on gear teeth. *Machine Design*. 1953; 25:203–211.

[45] Johnson DC, Bishop RED. Excitation of vibrating systems by gearing errors. *Journal of the Royal Aeronautical Society*. 1955; 59:434–435.

[46] Tuplin WA. Dynamic loads on gear teeth. In: *International Conference on Gearing*. London: IMechE; 1958.

[47] Bishop RED. Torsional failure caused by gear inaccuracy. *Journal of Mechanical Engineering Science*. 1962; 4:188–189.

[48] Johnson KL. *Contact mechanics*. Cambridge: Cambridge University Press; 1985.

[49] Litvin FL. *Theory of gearing*. NASA RP-1212; 1989.

[50] Litvin FL. *Gear geometry and applied theory*. Prentice Hall; 1994.

[51] Özgüven HN, Houser DR. Mathematical models used in gear dynamics—A review. *Journal of Sound and Vibration*. 1988;121(3):383–411.

[52] Kubur M, Yildirim V, Özgüven HN. A new model for simulating the dynamic characteristics of a helical system with multiple shafts. *Journal of Sound and Vibration*. 2004;271(1–2):481–508.

[53] Kahraman A, Singh R. Non-linear dynamic analysis of geared systems. *Nonlinear Dynamics*. 1990;1(2):175–191.

[54] Houser DR. The root of gear noise: Transmission error. *Power Transmission Design*. 1986; 28:27–30.

[55] Zhang X, Zhang T, Wu S. Research progress on gear transmission system dynamics. *Archive of Applied Mechanics*. 2023;93(7):2977–3006.

[56] Parker RG, Eritenel T. Three-dimensional nonlinear vibration of gear pairs. *Journal of Sound and Vibration*. 2012;331(15):3628–3648.

[57] Yang S. Analysis of gear noise and design for gear noise reduction. PhD Dissertation, Purdue University; 1993.

[58] Wang J, Zhang Y. Dynamic modeling and analysis of elastic isolation damping gears. *International Journal of Mechanical Sciences*. 2022; 222:107238.

[59] Shi C, Ding H. Dynamic modeling and stability analysis for a spur gear system considering gear backlash and bearing clearance. *Shock and Vibration*. 2019.

[60] Velex P, Maatar M. A general model for the analysis of vibration and noise of a planetary geared system. *Journal of Mechanical Design*. 1996;118(4):548–557.

[61] Mughal H, Sivayogan G, Dolatabadi N, Rahmani R. An efficient analytical approach to assess root cause of nonlinear electric vehicle gear whine. *Nonlinear Dynamics*. 2022;110(4):3167–3186.

[62] Ge S, Qiu L, Zhang Z, Wang H, Hu M. Electromechanical coupling dynamic characteristics of electric drive system for electric vehicle. *Nonlinear Dynamics*. 2024;112(8):6101–6136.

[63] Jiang S, Li W, Xin G, Sheng L, Fan M, Yang X. Analysis of torsional vibration characteristics and time delay feedback control of semi-direct drive cutting transmission system. *Chaos, Solitons & Fractals*. 2020; 132:109607.

[64] Wellmann T, Tousignant T, Govindswamy K, Tomazic D, Steffens C, Janssen P. NVH aspects of electric drive unit development and vehicle integration. SAE Technical Paper; 2019.

[65] Jiang S, Li W, Wang Y, Yang X, Xu S. Electromechanical coupling torsional resonance characteristics of gear system driven by PMSM. *Nonlinear Dynamics*. 2021;104(2):1205–1225.

[66] Fan X, Li X, Shang D, Wang H. Multi-excitation interaction-based mechatronics modeling and vibration characteristics analysis of electric powertrain. *Nonlinear Dynamics*. 2025.

[67] Feki N, Clerc G, Velex P. An integrated electro-mechanical model of motor–gear units. *Mechanical Systems and Signal Processing*. 2012; 29:377–390.

[68] Bai W, Qin D, Wang Y, Lim TC. Dynamic characteristics of electromechanical coupling effects in motor–gear systems. *Journal of Sound and Vibration*. 2018; 423:50–64.

[69] Bai W, Qin D, Wang Y, Lim TC. Dynamic characteristics of motor–gear systems under load variations and voltage transients. *Mechanical Systems and Signal Processing*. 2018; 100:1–16.

[70] Chen X, Hu J, Chen K, Peng Z. Modeling of electromagnetic torque considering saturation and magnetic field harmonics in PMSM. *Simulation Modelling Practice and Theory*. 2016; 66:212–225.

[71] Kwak SY, Kim JK, Jung HK. Characteristic analysis of multilayer buried magnet synchronous motors using fixed permeability method. *IEEE Transactions on Energy Conversion*. 2005; 20:549–555.

[72] Ge S, Qiu L, Zhang Z, Wang H, Hu M. Electromechanical coupling dynamic characteristics of electric drive systems. *Nonlinear Dynamics*. 2024; 112:6101–6136.

[73] Donmez A, Kahraman A. Dynamic behavior of electric vehicle gear trains. *Journal of Computational and Nonlinear Dynamics*. 2025;20(2):021003.

[74] Mughal H, Dolatabadi N, Rahmani R, King P, Gnanakumar M, Varnier O. Tribodynamic analysis of lubricated gear contacts for gear whine identification. *Mechanical Systems and Signal Processing*. 2025; 236:113054.

[75] Wang J, Li R, Peng X. Survey of nonlinear vibration of gear transmission systems. *Applied Mechanics Reviews*. 2003; 56:309–329.

[76] Velex P. On the modelling of spur and helical gear dynamic behavior; 2012.

[77] Yang J, Dai L. Survey of dynamics of planetary gear trains. *International Journal of Materials and Structural Integrity*. 2008; 1:302–322.

[78] Chen S, Tang J, Li Y, Hu Z. Rotor dynamics analysis of double-helical gear transmission systems. *Meccanica*. 2016; 51:251–268.

[79] Chen S, Tang J, Zhou C, Hu Z. Modal and whirling analysis of coupled lateral and torsional vibration of herringbone gears. *International Journal of Dynamics and Control*. 2014.

[80] Wang C, Wang SR, Yang B, Wang GQ. Dynamic modeling of double helical gears. *Journal of Vibration and Control*. 2018; 24:3989–3999.

[81] Vijayakar SM, Busby HR, Houser DR. Linearization of multibody frictional contact problems. *Computers & Structures*. 1988; 29:569–576.

[82] Özgüven HN, Houser DR. Dynamic analysis of high-speed gears using loaded static transmission error. *Journal of Sound and Vibration*. 1988; 125:71–83.

[83] Kang MR, Kahraman A. Dynamic behavior of double-helical gear sets. *Journal of Sound and Vibration*. 2015; 350:11–29.

[84] Kahraman A, Singh R. Non-linear dynamics of a spur gear pair. *Journal of Sound and Vibration*. 1990; 142:49–75.

[85] Kahraman A, Singh R. Interaction between time-varying mesh stiffness and clearance nonlinearities. *Journal of Sound and Vibration*. 1991; 146:135–156.

[86] Theodossiades S, Natsiavas S. Non-linear dynamics of gear-pair systems with periodic stiffness and backlash. *Journal of Sound and Vibration*. 2000; 229:287–310.

[87] Litak G, Friswell MI. Vibration in gear systems. *Chaos, Solitons & Fractals*. 2003; 16:795–800.

[88] Li S, Kahraman A. Spur gear mesh interface damping model based on elastohydrodynamic contact. *International Journal of Powertrains*. 2011;1(4).

[89] Wei S, Han QK, Dong XJ, Peng ZK, Chu FL. Dynamic response of a single-mesh gear system under uncertainty. *Nonlinear Dynamics*. 2017; 89:49–60.

[90] Yang Y, Cao L, Li H, Dai Y. Nonlinear dynamic response of a spur gear pairs with time-varying stiffness. *Applied Mathematical Modelling*. 2019; 72:444–469.

[91] Yang Y, Xu M, Du Y, Zhao P, Dai Y. Dynamic analysis of nonlinear spur gear systems under multi-frequency excitation. *Journal of Vibration and Control*. 2019; 25:1210–1226.

[92] Shi J, Gou X, Zhu L. Modeling and analysis of spur gear pairs considering multi-state mesh. *Mechanism and Machine Theory*. 2019; 134:582–603.

[93] Cirelli M, Valentini PP, Pennestrì E. Nonlinear dynamic response of spur gears using multibody contact-based models. *Journal of Sound and Vibration*. 2019; 445:148–167.

[94] Xiao Z, Zhou C, Chen S, Li Z. Effects of oil film stiffness and damping on spur gear dynamics. *Nonlinear Dynamics*. 2019; 96:145–159.

[95] Park CI. Dynamic behavior of spur gear systems with time-varying stiffness and backlash. *Journal of Mechanical Science and Technology*. 2020; 34:565–572.

[96] Liu F, Jiang H, Liu S, Yu X. Dynamic behavior analysis of spur gears considering sliding friction. *Journal of Mechanical Science and Technology*. 2016; 30:5363–5370.

[97] Kahraman A, Blankenship GW. Experiments on nonlinear dynamic behavior of oscillators with clearance. *Journal of Applied Mechanics*. 1997; 64:217–226.

[98] Velex P, Cahouet V. Influence of tooth friction in spur and helical gear dynamics. *Journal of Mechanical Design*. 2000; 122:515.

[99] Vijayakar S, Marambedu K, Baker B. *Transmission3D user's manual*. 2023.

[100] Vijayakar SM. Linearization of multibody frictional contact problems. *Computers & Structures*. 1988;29(4):569–576.

[101] Bonori G. *Static and dynamic modelling of gear transmissions*. PhD Dissertation, University of Modena and Reggio Emilia; 2005.

[102] Rosenbrock HH. The stability of linear time-dependent control systems. *Journal of Electronics and Control*. 1963;15(1):73–80.

[103] Ray S, Zhu J. Frozen-time eigenvalues for stability analysis of periodic linear systems. In: *Proceedings of the Southeastern Symposium on System Theory*. 1991. p. 450–453.

[104] Meirovitch L. *Fundamentals of vibration*. New York: McGraw-Hill; 2001.

[105] Moon FC. *Chaotic vibrations: An introduction for applied scientists and engineers*. New York: Wiley; 2004.

[106] Lin HH, Liou CH. Spur gear dynamics study. NASA/CR-98-206598; 1998.

[107] Hahn WF. Instantaneous gear tooth loading study. PhD Dissertation, University of Illinois; 1969.

[108] Altair Engineering Inc. *Altair Flux documentation*, Version 2024.1; 2024.

[109] Ba X, Gong Z, Guo Y, et al. Equivalent circuit models of PMSM considering core loss. *Energies*. 2022;15(6):1995.

[110] Krause P, Wasynczuk O, Sudhoff S, Pekarek S. *Analysis of electric machinery and drive systems*. 2nd ed. New York: Wiley; 2002.

[111] The MathWorks Inc. *MATLAB*, Version R2024b. Natick; 2023.

[112] Busarello TDC, Bubshait A, Varaprasad OVSR, et al. Field-oriented control design with parameter variation analysis for IPMSM drives. *IEEE Access*. 2025; 13:89524–89541.

[113] Rosenbrock HH. The stability of linear time-dependent control systems. *Journal of Electronics and Control*. 1963;15(1):73–80.

[114] Rosenstein MT, Collins JJ, De Luca CJ. A practical method for calculating largest Lyapunov exponents from small data sets. *Physica D: Nonlinear Phenomena*. 1993;65(1-2):117-134. doi:10.1016/0167-2789(93)90009-P.

[115] Parker TS, Chua LO. Chaos: A tutorial for engineers. *Proceedings of the IEEE*. 1987;75(8):982-1008. doi:10.1109/PROC.1987.13845.